

JPL Publication 11-6



Estimates of SEU Rates from Heavy Ions in Devices Exhibiting Dual-Node Susceptibility

Larry D. Edmonds

**National Aeronautics and
Space Administration**

**Jet Propulsion Laboratory
California Institute of Technology
Pasadena, California**

June 2011

This research was carried out at the Jet Propulsion Laboratory, California Institute of Technology, under a contract with Xilinx Corporation.

Reference herein to any specific commercial product, process, or service by trade name, trademark, manufacturer, or otherwise, does not constitute or imply its endorsement by the United States Government or the Jet Propulsion Laboratory, California Institute of Technology.

©2011 California Institute of Technology. Government sponsorship acknowledged.

TABLE OF CONTENTS

Abstract.....	iii
I. Introduction	1
II. Review of the Single Node Problem.....	2
III. The Starting Equation	4
IV. Preview of Three Methods	6
A. The Brute-Force Method.....	6
B. Fitting Data to a Beam Alignment Measure	6
C. Fitting Data to a Physical Model.....	7
V. The Brute-Force Calculation	8
VI. Fitting Data to a Beam Alignment Measure.....	13
A. A Measure of Beam Alignment	13
B. Calculating σ_{AVG} From Alignment Measure Plots.....	19
VII. Fitting Data to a Physical Model.....	21
A. Statement of the Model for Single Nodes	21
B. The Dual-Node Problem	24
C. Summary of the Final Equations.....	30
VIII. Codes and an Example.....	32
IX. A Second Example.....	49
A. The All-1's Pattern.....	49
B. The All-0's Pattern.....	65
C. Comparison with SRAM7	77
Appendix A. Derivation of (13).....	81
Appendix B. Derivation of (14).....	84
Appendix C. Evaluation of I	88
Appendix D. Regression Wizard Programming.....	89
Appendix E. The Transform	91
Appendix F. The Fortran Code	93
References.....	95

ABSTRACT

A single-event effect (SEE) occurs when a single ionizing particle passing through an electronic device produces a detectable event in the device (e.g., a bit flip in a memory element). The type of SEE most frequently discussed in the literature is a “single-node upset” problem. A device contains a set of nodes and an error is observed if any one or more of these nodes collects enough charge to upset that node. The terminology “single node” reflects the fact that, in this problem, whether or not a given node upsets depends only on conditions seen by that node, and is independent of responses from other nodes. In contrast, Xilinx has developed SEE tolerant devices with circuitry designed so that a device error becomes a “dual-node” problem. In this problem, a given cell contains a pair of nodes with the property that a device error requires that each node *simultaneously* (i.e., from the same particle hit) collect some sufficient amount of charge. When measuring upset cross sections for heavy ions at a particle accelerator, while varying the direction of the ion beam relative to the device, the dual-node device exhibits a complex directional dependence not seen in single-node devices. This directional dependence reflects not only the directional dependence associated with the upset susceptibility of individual nodes (which would also be seen in single-node devices), but also a directional dependence associated with the degree of beam alignment relative to a line connecting the nodes (which is not seen in single-node devices). In particular, inspection of an actual data set has shown the directional dependence of the dual-node cross section violates the “invariant integral property” that is defined and discussed in Section II. This implies that methods traditionally used to calculate SEE rates for single-node devices in given heavy-ion environments (e.g., the familiar RPP model) cannot be used for dual-node devices. The objective of this report is to develop an algorithm for calculating SEE rates in known heavy-ion environments for dual-node devices.

Three approaches for heavy-ion-induced rate calculations are discussed. All three require heavy-ion cross section measurements as input information, and also assume that incident particles are adequately described by linear energy transfer (LET) and direction of travel, but the approaches differ in terms of the amount of test data that is needed. The first approach is entirely empirical. The advantage of this approach is that the reliability of the predicted rate is not dependent on the validity of any assumed charge-collection device-physics model. The disadvantage of this approach is the enormous amount of test data that is required. Even the example included for illustration did not have enough data for a rate estimate (there is a complete set of test data for one ion LET, but not for other LETs). The discussion is still included in this report (in Section V) because this approach is still an option if the needed data set ever becomes available for a particular device. The second approach, discussed in Section VI, is essentially a more sophisticated version of the first approach. It is more sophisticated in terms of data processing algorithms, so numerical computations are less laborious. It also allows greater flexibility in the structure of the test data, in the sense that more randomness is allowed in the tilt angles and rotation angles selected for tests. Like the first approach, the second approach requires an enormous amount of test data.

The third approach, in Section VII, uses a physical model. It is still a data-fitting tool in the sense that the input information consists of experimentally measured cross sections from heavy ions. This method does not require as much test data as a purely empirical method, because interpolations/extrapolations of the data set are guided by physical considerations. A data-fitting tool has the advantage that the physical assumptions can be simpler than would be needed to derive predictions when the given information consists of device construction specifications (a task that is best performed by a device simulator). To be successful as a data-fitting tool, a physical model merely has to have the versatility needed to fit data (via adjustable fitting parameters), together with the correct qualitative behavior as needed to interpolate/extrapolate test data. A more familiar example of a data-fitting tool is the RPP model traditionally used for single-node upset rate estimates. As a physical charge-collection model, the RPP model is oversimplified, but this model can still estimate upset rates for single-node devices in a given heavy-ion environment when suitable values are assigned to model parameters. However, the dual-node problem requires more than a simple RPP. Even a pair of RPPs, one for each node, is inadequate when charge sharing (each node collects a different portion of the same increment of liberated charge) has a role. One possible approach is to allow for nested and weighted RPPs, with each RPP assigned a different weight factor describing the fraction of liberated charge that is collected by the node it is associated with. The approach that was actually followed is similar, except that the RPP corners are rounded to produce ellipsoids. This was done for analytical convenience, and produces relatively simple mathematical expressions for dual-node cross section calculations, making Monte Carlo trajectory tracing unnecessary. The mathematical analysis applied to the physical model is exact, so model predictions exactly describe a dual-node device, but the device itself is a simplified idealization intended to approximate a real device in terms of susceptibility to heavy ions from direct ionization. This simplified idealization was constructed with the intention of giving it the correct qualitative properties as needed to interpolate/extrapolate test data.

Each of the three methods above is accompanied by an illustrative example. The third method (Section VII) carries the example to completion, and gives a rate estimate for a selected environment. This method requires some software. Hard copies of the programming (which can be typed in at the keyboard) are provided, together with step-by-step instructions on usage.

The parts selected for the illustrative examples were fabricated by Xilinx, and heavy-ion tests were conducted by Xilinx in collaboration with JPL. Heavy-ion test data were provided by Gary Swift (formally with JPL, now with Xilinx), Carl Carmichael (Xilinx), and Gregory Allen (JPL), and are reproduced here with permission from Xilinx. It should be noted that these example devices represent the early stages of an on-going part-development research effort by Xilinx, and may not represent the final product that Xilinx will be offering to the public.

I. INTRODUCTION

A single-event-effect (SEE) occurs when a single ionizing particle passing through an electronic device produces a detectable event in the device (e.g., a bit flip in a memory element). The type of SEE most frequently discussed in the literature is a “single-node” problem. A device contains a set of nodes and an SEE occurs in the device if any one or more of these nodes collects an amount of charge exceeding the “critical charge” for that node (depending on device circuitry, the concept of a well-defined critical charge may be a good approximation even when it is not strictly correct due to time-dependent effects). The terminology “single node” reflects the fact that, in this problem, whether or not a given node contributes to a device response (e.g., a bit flip) depends only on conditions seen by that node, and is independent of responses from other nodes. In contrast, Xilinx has developed SEE tolerant devices with circuitry designed so that an SEE becomes a “dual-node” problem. Each bit in the device contains a set of nodes but an SEE involves a particular pair of nodes; call them Node 1 and Node 2. Circuit simulations performed by Xilinx have found that an SEE requires that charge collected by Node 1 exceed a critical value for Node 1, *and* charge collected by Node 2 exceed a critical value for Node 2, *simultaneously* (i.e., from the same particle hit). The objective of this report is to develop an algorithm for calculating SEE rates in known heavy-ion environments for such devices.

Such calculations can be performed by integrating an environmental flux, expressed as a function of ion linear energy transfer (LET), multiplied by a device SEE cross section expressed as a function of both LET and particle direction relative to the device. The LET integration is performed numerically, and the flux is regarded as known, so the theoretical work reduces to the problem of estimating the cross section from available experimental data, and integrating the cross section with respect to particle trajectory angles. Heavy-ion rate calculations traditionally assume an isotropic environment, and the same assumption will be used here, so the only directional effects are in the device response, and are reflected by the device cross section.

II. REVIEW OF THE SINGLE NODE PROBLEM

Although the problem considered is the dual-node problem, it is reasonable to ask whether earlier work with the more familiar single-node problem will help with this investigation, so we give a brief review of the single-node problem. The “single-node” qualification, and the numerical value assigned to the critical charge are statements regarding device circuitry, but the problem has not yet been sufficiently described until a model is given for calculating charge collected by the node from a hit by an ionizing particle. Device simulators can solve the most complex charge-transport equations, but simplified models are typically used for analytical work. The most versatile simplified model, used for analytical studies in [1]-[8], is based on a “charge-collection-efficiency” function, which quantifies the importance of an increment of charge liberated at one location compared to the same amount of charge liberated at another location within the device. For example, if an increment of charge liberated at a point (x_1, y_1, z_1) produces the same collected charge as twice this increment liberated at another point (x_2, y_2, z_2) , then the charge-collection efficiency for the first point is twice as large as the charge-collection efficiency for the second point. The collected charge is the volume integral of the charge-collection efficiency multiplied by the density of charge liberated by the ion.

A special case of the above model is the sensitive volume model, in which the charge-collection efficiency is unity inside some pre-defined volume and zero outside, so collected charge equals the charge liberated within the volume. A special case of the sensitive volume model is the rectangular parallelepiped (RPP) model, in which the sensitive volumes are RPPs. Normal-incident cross section versus LET curves experimentally measured for devices are typically smooth curves (as opposed to an abrupt step function), and such curves can be obtained from the RPP model by imagining a collection of RPPs, having a distribution of critical charges, and adding cross sections. This leads to the integrated RPP (IRPP) method of rate calculations [9], which is used by the CREME96 code.¹ This code is the industry standard for environmental models and is also commonly used to calculate SEE rates.

The RPP model is not a realistic description of charge-collection physics in typical low- to moderate-voltage microelectronic devices [8], so the RPP dimensions needed to correctly describe the directional dependence of the device cross section need not correspond to physically recognizable quantities. In particular, it is generally recognized that a “funnel length” should not be included in the RPP thickness (if the model were correct, the thickness would be the charge collection depth, which includes a funnel length when funnel length is defined in terms of charge-collection depth). The lack of realism is particularly obvious when considering cases involving “charge sharing,” in which one portion of the charge liberated at a given location is collected by one node, and another portion is collected by another node (although the more general case of a charge-collection-efficiency function is compatible with charge sharing [8]). However, the RPP model can approximate the directional dependence of the device cross section if RPP

¹ CREME96 has been replaced by CRÈME-MC at the new website <https://creme.isde.vanderbilt.edu/>. However, the new code includes (among other things) all of the data sets and algorithms used by the original CREME96, so calculations performed by the original code can be duplicated by the new code.

dimensions are selected to do that, so the model is traditionally used as a data-fitting tool in spite of its lack of reality.

The RPP model illustrates the fact that a model need not be physically correct in order to fit data, so it is reasonable to ask if there is an existing model intended for the single-node problem that might also serve as a fitting tool for the dual-node problem. This question can be answered, at least in the context of the models discussed in this section, because all of these models have an “invariant integral property.” This property states that [5]

$$\int_0^{\infty} \frac{\sigma(L, \theta, \varphi)}{L^2} dL = \int_0^{\infty} \frac{\sigma_N(L)}{L^2} dL \quad (\text{single node}) \quad (1)$$

where L is particle LET (not the effective LET that is often reported at accelerator facilities), θ is the tilt angle of the beam relative to the device, φ is the rotation angle of the beam relative to the device, $\sigma_N(L)$ is the normal-incident ($\theta = 0$) cross section as a function of LET, and $\sigma(L, \theta, \varphi)$ is the directional cross section for the direction defined by θ and φ . The directional cross section is experimentally defined to be the number of SEE counts divided by beam fluence, when beam fluence is measured in a plane perpendicular to the beam (not the device plane, even though accelerator facilities often report fluence measured in the device plane). The integral on the left side of (1) is invariant in the sense that it has the same value for all beam directions. This can be visualized for the RPP model by noting that the direction that sees the longest path length (smallest threshold LET) also sees the smallest projected area (or saturation cross section), so a decrease in threshold LET is accompanied by a decrease in saturation cross section. More generally, for any model discussed in this section, any change in direction that increases the cross section at small LET must also decrease the cross section at larger LET as needed to produce the same integral.

However, experimental measurements of the directional cross section, performed by Xilinx, have shown that the dual-node devices of interest to this report badly violate the invariant integral property (1). The conclusion is that no single-node model derivable from a charge-collection efficiency function (which includes the RPP model as a special case) will be able to fit the data presented in later sections.

III. THE STARTING EQUATION

The previous section concluded that the conventional single-node models will not be able to fit the data presented in later sections, even if the models are used merely as data-fitting tools and we do not insist on physical validity. It is therefore necessary to start from first principles. The most versatile equation for calculating rates in an isotropic flux is

$$\text{SEE rate} = \int_0^\infty \int_0^\pi \int_0^{2\pi} h(L) \sigma(L, \theta, \varphi) \sin \theta \, d\varphi \, d\theta \, dL \quad (2)$$

where $h(L)$ is the differential (in LET) directional flux, and the other symbols were explained in the previous section. Although the flux is assumed to be isotropic, it is still called directional to distinguish it from the omnidirectional flux, which is 4π times the directional flux. The two types of fluxes can be recognized by the units, with a persteradian appearing in the directional flux but not in the omnidirectional flux. Note that (2) is an immediate result of the definition of directional cross section, and applies to any kind of SEE having the property that a cross section is defined (i.e., counts are proportional to fluence) together with the property that ions are adequately described by LET and direction. For those cases in which the directional dependence of device susceptibility is known (or assumed) there are a variety of ways to change the appearance of (2). One of the more common forms is an LET integration of the normal-incident (instead of directional) cross section multiplied by an “effective flux”². In this form, there are no integrations in angles because these integrations were already performed when constructing the effective flux. However, the effective flux approach is only useful when the directional dependence of device susceptibility is known (or assumed) in advance. The problem considered here is that in which the directional dependence of device susceptibility is *not* known in advance, but must be extracted from the measured data. The form of (2) that is most useful for this case is obtained by factoring the flux out of the angular integrals to get

$$\text{SEE rate} = \int_0^\infty h_{OMNI}(L) \sigma_{AVG}(L) \, dL \quad (3)$$

where the omnidirectional flux h_{OMNI} is defined by

$$h_{OMNI}(L) \equiv 4\pi h(L) \quad (4)$$

and the directional-average cross section σ_{AVG} is defined by

² An effective flux was first defined by Binder [10] for devices that satisfy the cosine law, but the definition was later generalized to include a broad category of device models, including the RPP model (see Section VIII-D in [5]). In fact, it was pointed out in [8] that the traditional IRPP rate calculation method is an effective flux calculation, although it is rarely called that.

$$\sigma_{AVG}(L) \equiv \frac{1}{4\pi} \int_0^\pi \int_0^{2\pi} \sigma(L, \theta, \varphi) \sin \theta \, d\varphi \, d\theta. \quad (5)$$

Note that the directional-average cross section can be calculated directly from (5), or it can be calculated in two steps by first calculating the phi-average cross section from

$$\sigma_{phi-avg}(L, \theta) \equiv \frac{1}{2\pi} \int_0^{2\pi} \sigma(L, \theta, \varphi) \, d\varphi \quad (6a)$$

and then calculate σ_{AVG} from

$$\sigma_{AVG}(L) \equiv \frac{1}{2} \int_0^\pi \sigma_{phi-avg}(L, \theta) \sin \theta \, d\theta = \frac{1}{2} \int_{-1}^1 \sigma_{phi-avg}(L, \theta) \, d(\cos \theta). \quad (6b)$$

There are two important points to remember when using the above equations:

- (a) The directional cross section $\sigma(L, \theta, \varphi)$ in (5) and (6a) is experimentally defined to be counts divided by fluence, when fluence is measured in a plane perpendicular to the beam. This is not the same as fluence measured in the device plane, which is reported at some experimental facilities.
- (b) The LET L in all equations is actual ion LET, which is not the same as the “effective LET” reported at some experimental facilities.

The SEE rate is calculated from a numerical integration of (3), with h_{OMNI} regarded as given, so the main focus of this work is to derive an algorithm for estimating σ_{AVG} . This is the objective of the remainder of this report.

IV. PREVIEW OF THREE METHODS

This paper will present three methods for rate calculations, with each one having advantages and disadvantages compared to the other two, so one method might be preferred for some examples while another method might be preferred for other examples. When comparing the advantages and disadvantages in the discussions below, the phrase “complete data set” will be used and is defined here. A data set consists of a set of measured directional cross sections as a function of LET, tilt angle, and rotation angle. Whether or not a data set is called “complete” is somewhat subjective because it depends on the users perception of the reliability of graphical interpolations and extrapolations, but a loose definition can be given. A data set is called complete if it is sufficiently dense and broad so that graphical methods can be used to reliably (as judged by the user) interpolate/extrapolate the data between and beyond the measured points. The advantages and disadvantages of the three methods are compared below. Details for each method are given in later sections.

A. *The Brute-Force Method*

The brute-force method numerically integrates measured data without any benefits from physical models. The primary advantage of this method is that its validity does not depend on the validity of any assumed physical model, so there are no errors associated with deficiencies in assumed models. The only requirement is that a cross section is defined, i.e., counts are proportional to fluence. The only error in the calculation method is from errors in the measured data and in the graphical interpolation/extrapolation of the data. The primary disadvantage is that the method requires a complete data set. If a data set is incomplete, there will always be the question of whether a peak in the cross section was missed, so rate calculations cannot be done. Stated another way, an incomplete data set has no value if the brute-force method is to be used. Adding new measurement points to a data set does not give the data set any value until enough points are included to make the data set complete. Because the definition of complete depends on the ability to interpolate/extrapolate, the most likely candidates for the brute-force method are devices in which the data show the simplest trends. For example, when plotting directional cross section against rotation angle (at a fixed LET and tilt angle), a simple trend is one in which the cross section exhibits two peaks and two valleys uniformly spaced in rotation angle. Devices exhibiting more complexity (many peaks and valleys and/or symmetry violations) are less likely candidates for the brute-force method because a complete data set for such cases is a very extensive data set that is difficult to obtain. A second disadvantage of the brute-force method is that the numerical computations are laborious. A third disadvantage is that the method has no ability to predict the impact of changes in device design. Numerical results are unique to the device that was tested. Each device design requires a separate test that produces another complete data set.

B. *Fitting Data to a Beam Alignment Measure*

This method is a data fitting method. However, the curve fit is not derived from a proposed physical model. Instead, it is derived from a fairly lenient assumption that is

expected to apply (roughly) to a variety of physical models, at least for devices exhibiting simple trends as discussed under the brute-force method. The assumption is that the cross section can be expressed as a function of a “beam alignment measure.” This assumption would be exactly correct if the beam alignment measure was defined in a suitable way for each device, but becomes an approximation when a simple expression (containing one or more adjustable fitting parameters) is assumed for the beam alignment measure. One advantage of this fitting method is that the numerical computations are less laborious than for any of the other rate calculation methods. Another advantage is that incomplete data sets have some value, and adding new measurement points to a data set increases the value of the data set. A disadvantage is that the expression assumed for the beam alignment measure may be more accurate for some devices than others, so a good fit is not always guaranteed. It is possible to envelope the data points between fitting curves (i.e., an upper-bound fit and a lower-bound fit) and the spread between the curves is an indication of how good the fit is. If the fit is poor, a large spread between curves produces error bars in the rate calculations. These error bars are an artifact of the data fitting method and are in addition to any errors associated with data measurements and data interpolation/extrapolation. Another disadvantage is that (like the brute-force method) this method does not benefit from physical models so it has no ability to predict the impact of changes in device design.

C. Fitting Data to a Physical Model

This method is another data fitting method, but in this case the curve fit is derived from a proposed device-physics model. One advantage of this method (like any other fitting method) is that incomplete data sets have some value, and adding new measurement points to a data set increases the value of the data set. A second, and perhaps the most important, advantage is that it may have some ability to predict the impact of changes in device design. By fitting the cross section data obtained for one device design, and noting the values assigned to the fitting parameters and then using some knowledge of device physics to estimate changes in the fitting parameters associated with changes in device design (e.g., node-to-node separation), estimates are obtained for the fitting parameters appropriate for a new device design. Putting these new fitting parameters into the model produces a prediction of the cross section for the new device design. A disadvantage of this method is that the proposed device-physics model may be more accurate for some devices than others, so a good fit is not always guaranteed.

V. THE BRUTE-FORCE CALCULATION

The objective is to obtain an estimate of the directional-average cross section σ_{AVG} . The brute-force method is merely a numerical evaluation of the integrals in (6), and is simple enough to be explained via an example. Although conceptually simple, this is not the recommended approach because it is computationally laborious (as will be seen below). However, it is still useful to work through one example because this example also serves as a test case for testing the validity of a more efficient method discussed in the next section.

Each LET value is a separate and independent calculation, so we can consider one LET value at a time. To be useful as a test case, the selected example should have a dense sampling of measured data points, so the selected example is the device that Xilinx has called “SRAM11” with the $3.5\mu\text{m}$ epi thickness and 90nm feature size, and tested with an ion LET of $58.5\text{MeV}\cdot\text{cm}^2/\text{mg}$. Measured cross section data provided by Xilinx for this example are reproduced in Table 1.

The first step in the calculation is to plot the directional cross section as a function of rotation angle, using a separate plot for each tilt angle. In this example, the cross section can be neglected for tilt angles less than 60° . Data for the larger tilt angles are shown as the circled points in Figs. 1 through 5. The next step is to extrapolate data to fill in gaps in the data, because a numerical integration that follows will require that the gaps be filled in. This device appears to have enough symmetry so that the first extrapolation of the data is a periodic extension using a 180° degree period. If any gaps still remain, additional extrapolations are needed. For example, Fig. 5 does not show a cutoff angle, so a graphical (visual) extrapolation was used to produce the points at the rotation angles of 150° and 245° . A periodic extension is then applied to these points. These extrapolations produced the boxed points in Figs. 1 through 5.

The next step is to represent each data set by a curve with vertices selected to be used in a numerical integration, such as the curves shown in Figs. 1 through 5. The points in the figures define the vertices of the curve, except where there are multiple points at the same rotation angle φ , in which case a single point must be selected. In the examples shown, the largest cross section was selected where there are multiple points. The points that were selected to define the vertices of a given curve are then listed in a separate column, and ordered by increasing φ , so that a numerical integration can be performed. The trapezoidal rule was used to integrate each curve with respect to φ in these examples. The integration produces the integral in (6a), except that the angle was expressed in degrees instead of radians so the coefficient $1/2\pi$ in (6a) is replaced by $1/360$. These numerical evaluations of the right side of (6a) produced the phi-average cross sections listed in the upper right corners in Figs. 1 through 5.

Table 1. Directional cross section (cm²/bit) as a function of direction for the SRAM11 (3.5μm epi thickness, 90nm feature size) tested with an ion LET of 58.5MeV-cm²/mg.

		Rotation Angle (degrees)						
		0	90	140	160	180	200	220
Tilt Angle (degrees)	0		0					
	50	2.14E-12	1.64E-12	3.05E-12		2.85E-12	3.05E-12	1.83E-12
	55	1.22E-11	1.64E-12	3.66E-12	4.26E-12	8.24E-12	7.32E-12	1.83E-12
	60	4.16E-11	1.51E-12	2.71E-12	2.18E-12	6.07E-11	7.32E-10	5.59E-12
	65	1.98E-9	1.22E-12	7.93E-12	6.35E-11	4.60E-10	6.10E-9	7.90E-10
	70		1.22E-12	2.56E-11	5.78E-10	4.76E-9	2.56E-8	8.73E-9
	75	2.48E-8		1.56E-11	3.00E-9		6.10E-8	2.14E-8
	80				5.09E-8	1.80E-7	1.40E-7	7.31E-8

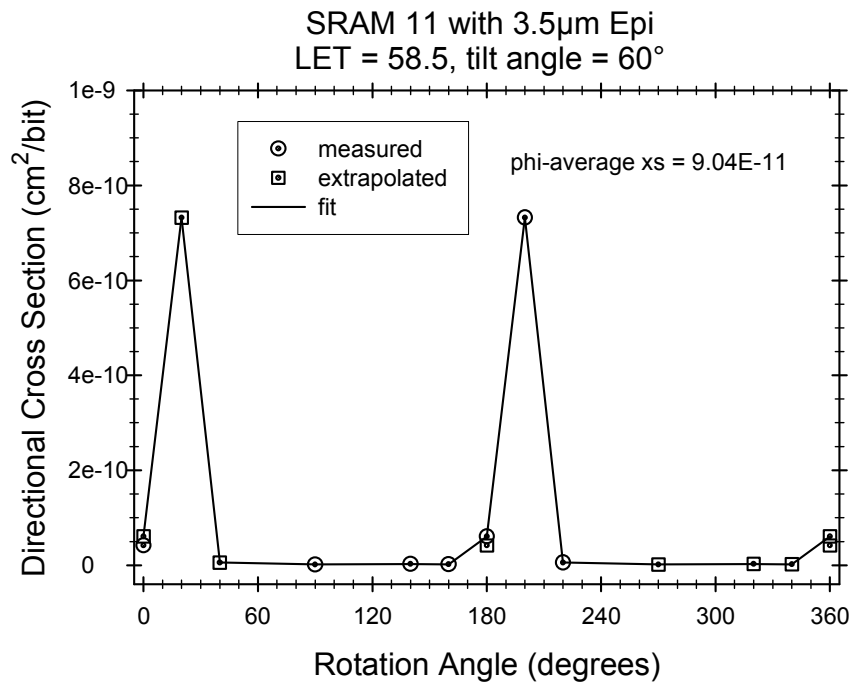


Fig. 1. Table I data and extrapolations for the 60° tilt angle.

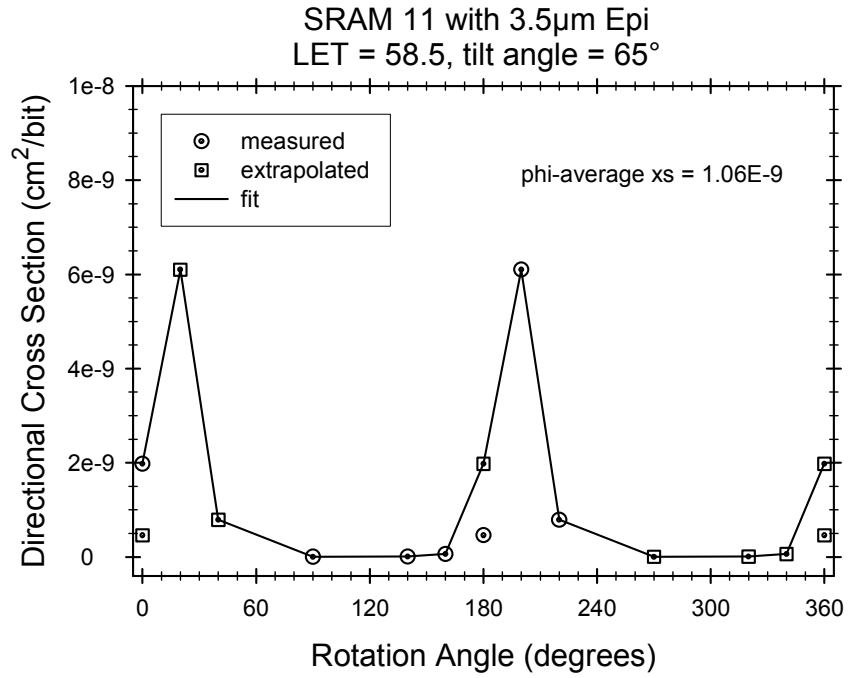


Fig. 2. Table I data and extrapolations for the 65 $^\circ$ tilt angle.

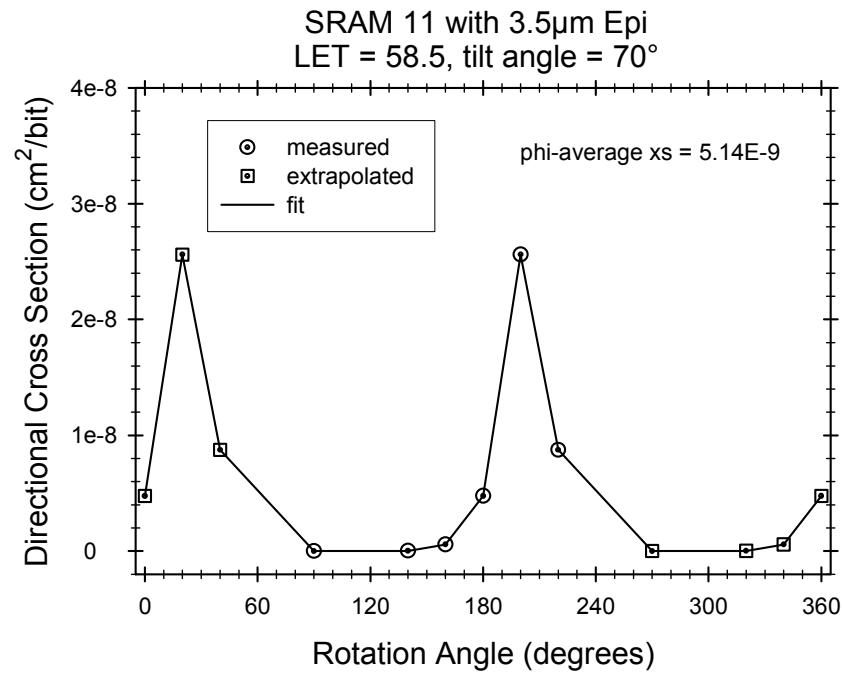


Fig. 3. Table I data and extrapolations for the 70 $^\circ$ tilt angle.

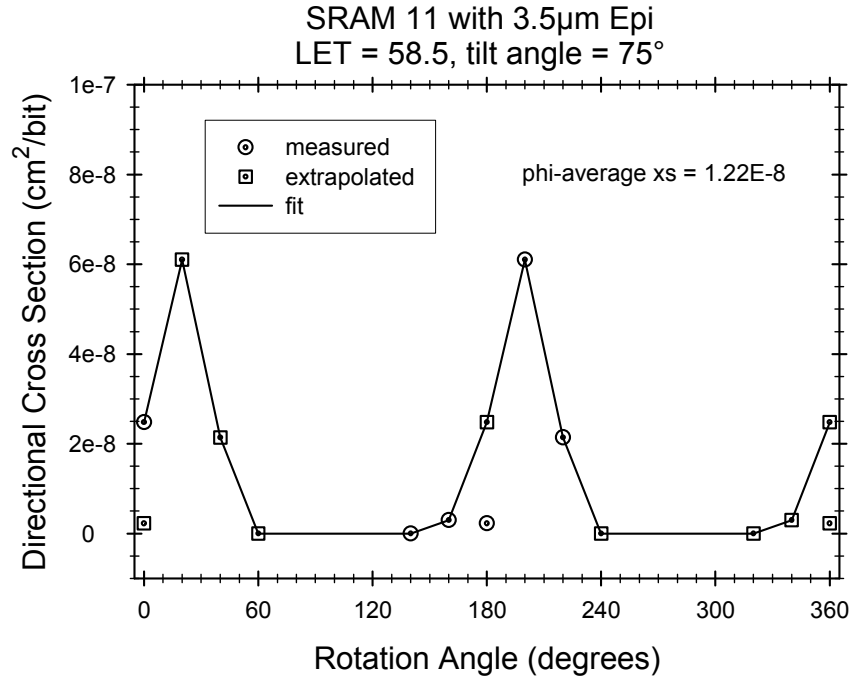


Fig. 4. Table I data and extrapolations for the 75 $^\circ$ tilt angle.

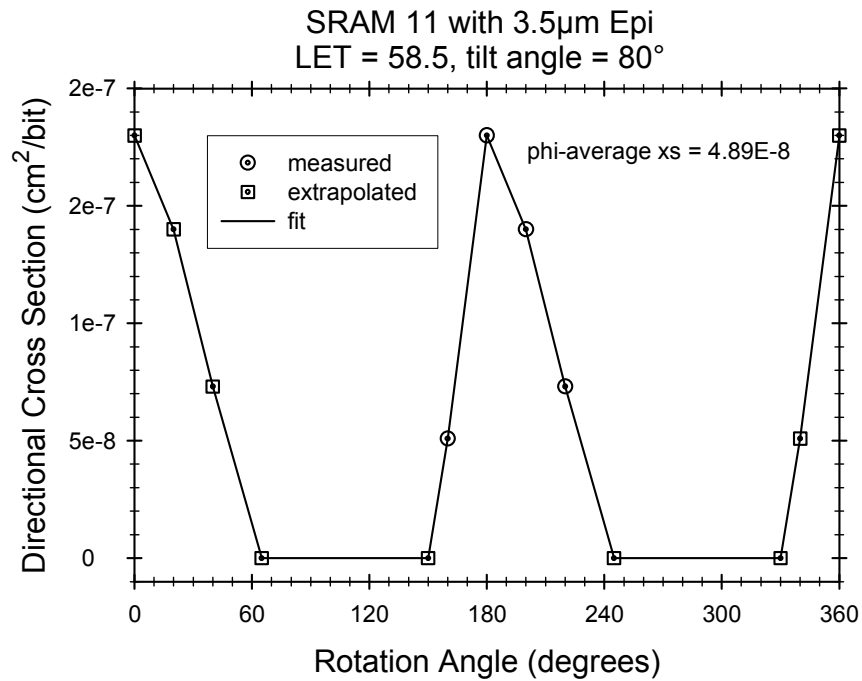


Fig. 5. Table I data and extrapolations for the 80 $^\circ$ tilt angle.

The next step is to plot the phi-average cross section as a function of tilt angle so that the final integration in (6b) can be performed. Anticipating that a simple curve fit can be found that will allow the integral to be evaluated analytically instead of numerically, it is convenient to use the cosine of the tilt angle for the horizontal axis. The phi-average cross sections listed in the upper right corners in Figs. 1 through 5 are plotted against the cosine of the tilt angle in Fig. 6. A simple fit was found (which is the curve in the figure) and it has the equation

$$\sigma_{\text{phi-avg}}(\theta) = a \exp(-b |\cos \theta|), \quad a = 1 \times 10^{-6} \text{ cm}^2/\text{bit}, \quad b = 15.95.$$

Substituting this fit into the far right side of (6b) gives the final result

$$\sigma_{\text{AVG}} = 6.27 \times 10^{-8} \text{ cm}^2/\text{bit} \text{ at LET} = 58.5 \text{ for this example.}$$

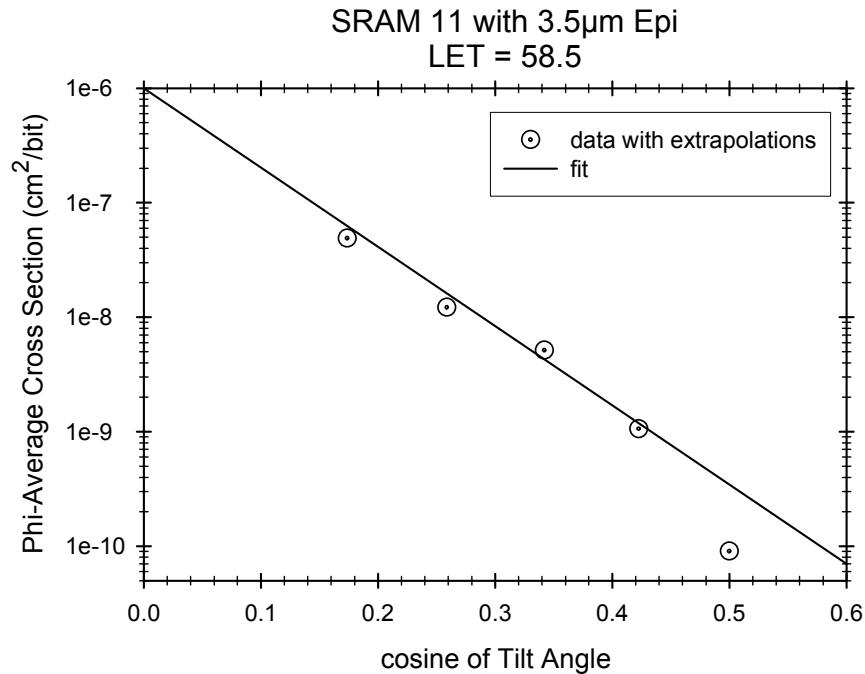


Fig. 6. Phi-averages listed in Figs. 1 through 5 are plotted against the cosine of the tilt angle.

VI. FITTING DATA TO A BEAM ALIGNMENT MEASURE

The method used in the previous section is very laborious because it requires a great deal of graphical work that is not easy to automate. The calculations would become much more efficient if we could find a way to plot data, at a fixed LET, so that all points belong to a single curve. In other words, instead of plotting the directional cross section against two angles (rotation and tilt), we look for a single parameter that the data can be plotted against. This is explained below and is followed by explanations of how this parameter is used in rate calculations.

A. *A Measure of Beam Alignment*

To construct such a parameter as discussed above, let us first consider a hypothetical case that may not be realistic but still serves as a visual aid. The coordinate system is oriented so that the x-axis connects both nodes and, for this hypothetical case, the susceptibility of each node has rotational symmetry about the x-axis. The directional cross section is then determined by the angle between the beam and the x-axis, and this one angle can be used as the single parameter that the directional cross section can be plotted against. This angle is also a measure of the degree of alignment between the beam and the x-axis, so the data can be plotted against this alignment measure. A more realistic case will not have such symmetry. For example, if the beam makes a 5° angle with the x-axis, it could make a difference whether this angular displacement is horizontal or vertical, i.e., a 5° change in tilt angle could have a different effect on the directional cross section than a 5° change in the rotation angle. It is necessary to construct a measure of beam alignment with the x-axis that distinguishes horizontal rotations from vertical rotations. This leads to what will be called an “elliptical measure of beam alignment” and is defined below.

As with the brute-force method, each LET is a separate and independent calculation, so we consider an arbitrary but fixed LET and do not display LET in the notation. The coordinate system is oriented so that a beam direction that is parallel to the x-axis produces the largest directional cross section, so the cross section depends on how close the beam direction is to the direction of the x-axis, but some quantitative definition of “close” is needed. For example, if a 5° angular displacement (of the beam relative to the x-axis) has a large effect on the cross section when the displacement is vertical, but a small effect when the displacement is horizontal, then a useful definition of “close” is one in which the latter beam direction is closer to the direction of the x-axis than the former beam direction. Such a measure of “close,” i.e., a measure of beam alignment with the x-axis, can be defined in terms of a family of ellipses.

The family of ellipses is constructed by selecting an arbitrary positive distance D to define the $x = D$ plane, and the family of ellipses lies in this plane. Each ellipse has one axis parallel to the y-axis, the other axis parallel to the z-axis, and the ellipse is centered on the x-axis. All ellipses in the family have the same eccentricity (which is regarded as given for now, but will be used as a fitting parameter later), so different ellipses in the family differ only in size. Such a family is illustrated in Fig. 7a. Different beam directions

are compared by selecting, for any given direction, the beam that connects the origin to the $x = D$ plane. Different beams that intersect the same ellipse are considered to have directions that are equally close to the direction of the x-axis, while a beam that intersects a smaller ellipse has a direction that is closer to the direction of the x-axis. This is illustrated in Fig. 7b.

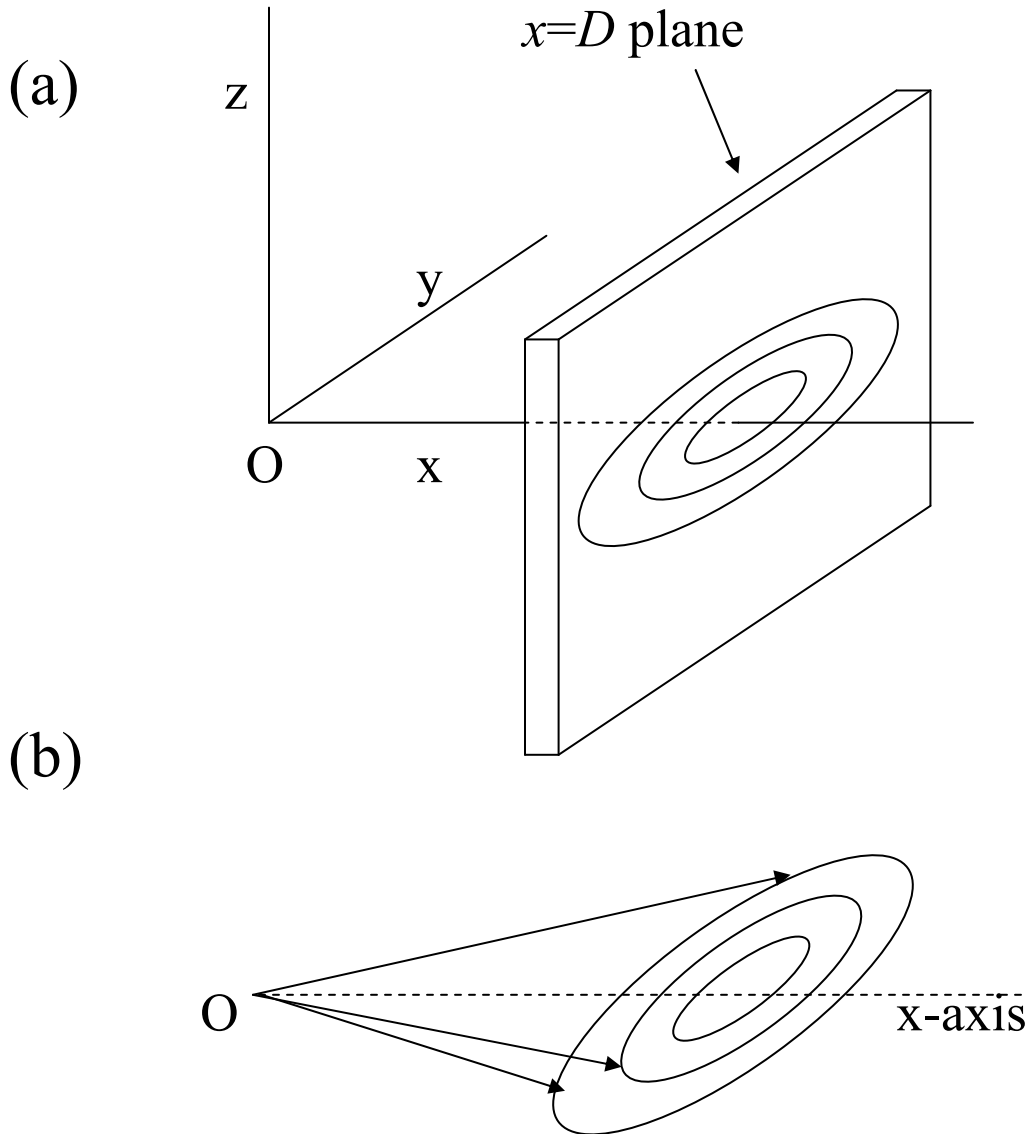


Fig. 7. The family of ellipses is shown in (a), while (b) compares three beam directions represented by arrows. The two beams that intersect the same ellipse have directions that are equally close to the direction of the x-axis, while the beam that intersects the smaller ellipse has a direction that is closer to the direction of the x-axis

Having used geometric properties to give a qualitative definition of “closeness” between a given direction and the x-axis, we now derive a quantitative measure of closeness, which will be called the measure of alignment between the given direction and the x-axis. Each ellipse in the family has the equation

$$A^2 z^2 + y^2 = \text{constant}$$

where A is a constant that is related to the eccentricity and is the same for each ellipse, so different ellipses differ in the numerical value assigned to the constant on the right. A particular ellipse is selected from the family by selecting a numerical value for the constant λ appearing in

$$A^2 z^2 + y^2 = D^2 \frac{1-\lambda^2}{\lambda^2} \quad (0 < \lambda \leq 1). \quad (7)$$

A given beam direction intersects a particular ellipse, as illustrated in Fig. 7b, and the λ -value of that ellipse is the quantitative measure of beam alignment. Note that a smaller ellipse has a larger λ , so a larger λ defines better alignment. To calculate λ in terms of the tilt angle and rotation angle of the beam, let the beam direction be represented by the unit vector \hat{a} , which is given by

$$\hat{a} = \sin \theta \cos \varphi \hat{e}_1 + \sin \theta \sin \varphi \hat{e}_2 + \cos \theta \hat{e}_3 \quad (8)$$

where \hat{e}_1 , \hat{e}_2 , and \hat{e}_3 are the unit vectors in the directions of the x-axis, y-axis, and z-axis, respectively. A displacement vector \vec{R} that has the direction of \hat{a} and connects the origin to the $x = D$ plane has the equation

$$\vec{R} = \frac{D}{\hat{a} \circ \hat{e}_1} \hat{a}$$

so the y and z coordinates of the intersected point in the $x = D$ plane are given by

$$y = \vec{R} \circ \hat{e}_2 = D \frac{\hat{a} \circ \hat{e}_2}{\hat{a} \circ \hat{e}_1}, \quad z = \vec{R} \circ \hat{e}_3 = D \frac{\hat{a} \circ \hat{e}_3}{\hat{a} \circ \hat{e}_1}.$$

Using (8), the above equations become

$$y = D \tan \varphi, \quad z = D \cot \theta \sec \varphi.$$

The ellipse that this point lies on has a λ given by

$$D^2 \frac{1-\lambda^2}{\lambda^2} = A^2 z^2 + y^2 = A^2 D^2 \cot^2 \theta \sec^2 \varphi + D^2 \tan^2 \varphi \quad (0 < \lambda \leq 1)$$

and solving for λ , which is now denoted $\lambda(\theta, \varphi)$ to display the directional dependence, gives

$$\lambda(\theta, \varphi) = \frac{|\sin \theta \cos \varphi|}{\sqrt{A^2 \cos^2 \theta + \sin^2 \theta}}. \quad (9)$$

The quantitative measure of alignment between the beam and the x-axis is $\lambda(\theta, \varphi)$ given by (9), with a larger $\lambda(\theta, \varphi)$ implying better alignment. Perfect alignment occurs when θ is 90° and φ is either zero or 180° , in which case $\lambda=1$. For the symmetric case ($A=1$), λ can be related to the angle γ that the beam makes with the x-axis. To derive this relation, note that γ satisfies $\cos \gamma = \hat{a} \cdot \hat{e}_1$, and using (8) gives

$$\cos \gamma = \sin \theta \cos \varphi. \quad (10)$$

Evaluating (9) at $A=1$ while using (10) gives

$$\lambda(\theta, \varphi) = |\cos \gamma| \quad \text{when } A = 1. \quad (11)$$

The absolute value is appropriate because parallel and anti-parallel are regarded as equivalent directions from the point of view of the directional cross section.

The value selected for A controls the relative importance of horizontal angular displacements compared to vertical angular displacements when assessing the degree of alignment between the beam and the x-axis. This can be visualized by looking at Fig. 7. If $A = 1$, the ellipses become circles and the alignment measure depends only on the angle γ between the beam and the x-axis. If $A \gg 1$, the ellipses become long and thin, with the long axis in the y-direction, so the alignment measure becomes much more sensitive to the tilt angle than to the rotation angle. If it were possible to select A in such a way so that the alignment measure has exactly the same relative sensitivity between horizontal rotations compared to vertical rotations as the directional cross section has, then different beam directions that have the same alignment measure will also produce the same directional cross section. In other words, the directional cross section would become a function of the alignment measure, so a plot of directional cross section versus the alignment measure would result in all points belonging to a single curve. If it is not possible to construct the alignment measure (i.e., find a suitable A) to make this relation exact, it may still be possible to construct an alignment measure (i.e., select an A) in such a way so that the above plot has an acceptable amount of scatter.

The discussion in the above paragraph will be illustrated by an example. The data to be plotted are shown in Table 1, and are also shown in Figs. 1 through 5. The mathematical analysis was derived for a coordinate system that is oriented so that the direction of the x-axis sees the largest directional cross section, so the first step is to adjust the rotation angles, by adding or subtracting a constant to them, to obtain an adjusted rotation angle in

which the largest cross sections are at $\varphi = 0$ and at $\varphi = 180^\circ$. The amount of offset can be different for different data sets when devices are replaced by fresh devices (to reduce radiation damage during the accelerator tests), so each data set is considered separately. For example, the 80° tilt-angle data in Table 1 (also seen in Fig. 5) show maximum cross sections at $\varphi = 0$ and at $\varphi = 180^\circ$, so no offset is used here. All other data sets show a maximum at $\varphi = 200^\circ$, so 20° is subtracted from each rotation angle to obtain the adjusted rotation angle. Then we select a trial value for A and use (9) to calculate the alignment measure λ for each data point, and plot the cross section against λ . The trial value $A = 1$ produced Fig. 8a, which shows a lot of scatter. The trial value $A = 5$ does much better, as seen in Fig. 8b, because the points can now be enveloped by bounding curves that are fairly close together. The bounding curves are empirical fits and the equations for them will be listed in the next subsection.

Note that whether we use the method in this section or the brute-force method in the previous section, it is necessary to extrapolate data because measurements cannot be made at a 90° tilt angle. In Fig. 6 it was necessary to extrapolate data for $\cos\theta < 0.17$. In Fig. 8b, it was necessary to extrapolate data for $\lambda > 0.74$. The two methods will be compared in the next subsection, so the two extrapolations should at least be compatible with each other. Note that the phi-average of the directional cross section cannot exceed the maximum directional cross section, so compatibility requires that the extrapolated (to $\lambda = 1$) directional cross section in Fig. 8b be at least as large as the extrapolated (to $\cos\theta = 0$) phi-average in Fig. 6. The upper curve in Fig. 8b satisfies this requirement while the lower curve does not, so we can anticipate that the upper curve will give better agreement with the brute-force method than the lower curve.

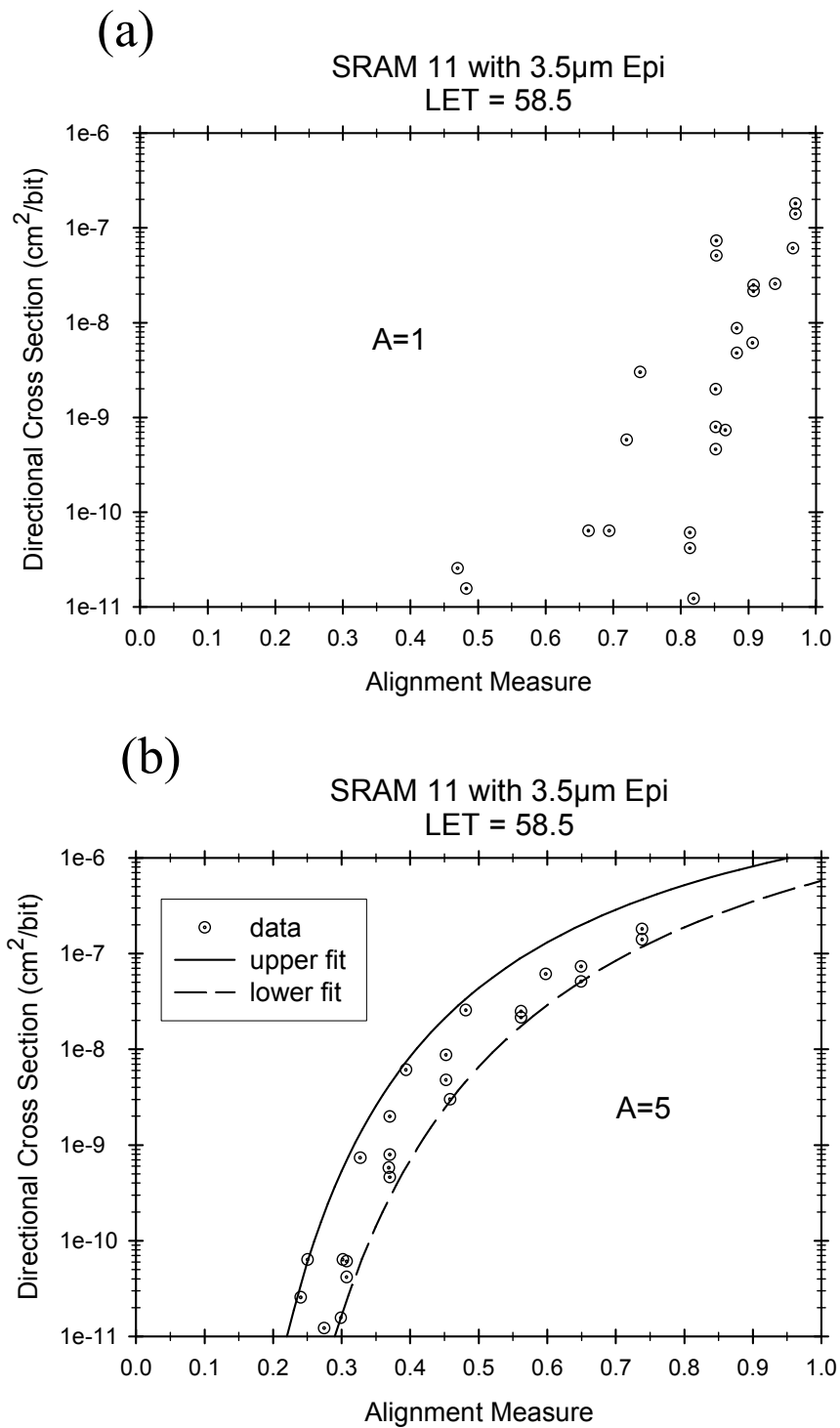


Fig. 8. The symmetric ($A = 1$) alignment measure does not conform well to the data because the points in (a) are badly scattered. Trial and error finds that the alignment measure defined by $A = 5$ is much better, because the points in (b) can be enveloped by bounding curves that are fairly close together.

B. Calculating σ_{AVG} From Alignment Measure Plots

Having obtained a plot such as shown in Fig. 8b, it is still necessary to perform the angular integrals in (5) in order to calculate σ_{AVG} . Again, each LET is a separate and independent calculation, so we consider an arbitrary but fixed LET and do not display LET in the notation. The directional cross section is either fit by some function of λ , i.e.,

$$\sigma(\theta, \varphi) \approx \sigma_{fit}(\lambda(\theta, \varphi))$$

for some fitting function σ_{fit} , or the directional cross section is bracketed between two such functions. In either case, an estimate of, or a bound for, the directional-average cross section is σ_{AVG}^* calculated from

$$\sigma_{AVG}^* \equiv \frac{1}{4\pi} \int_0^\pi \int_0^{2\pi} \sigma_{fit}(\lambda(\theta, \varphi)) \sin \theta \, d\varphi \, d\theta. \quad (12)$$

In order for this method to be computationally convenient, it is necessary to write the integral in (12) in such a way so that only a single numerical integration is needed. It is shown in Appendix A that (12) can be written as

$$\sigma_{AVG}^* = \frac{1}{A} \int_0^1 T(\lambda) \sigma_{fit}(\lambda) \, d\lambda \quad (13)$$

where λ is now an integration dummy symbol, T is a suitably defined function (see below), and A is the parameter that appears in (9) and was already selected when constructing plots of the type shown in Fig. 8b. Appendix B shows that an approximation for T is given by

$$T(\lambda) \approx \frac{1}{2} \frac{\eta+1}{\eta^2} \left[1 + \frac{1}{8} \left(\frac{\eta-1}{\eta+1} \right)^2 \right]^2 \quad (14a)$$

where

$$\eta \equiv \frac{1}{A} \sqrt{(A^2 - 1) \lambda^2 + 1}. \quad (14b)$$

The error in the approximation (14a) is less than 0.6% for any $A > 0$ and any λ between 0 and 1.

For example, the upper and lower curves in Fig. 8b have the equations

$$\sigma_{fit} = a e^{-b/\lambda}, \quad a = 3.2 \times 10^{-5} \text{ cm}^2/\text{bit}, \quad b = 3.30 \quad (\text{upper})$$

$$\sigma_{fit} = a e^{-b/\lambda}, \quad a = 5.07 \times 10^{-5} \text{ cm}^2/\text{bit}, \quad b = 4.48 \quad (\text{lower}).$$

Using these equations together with (14) and numerically evaluating the integral in (13) produces the bounds

$$\sigma_{AVG}^* = \begin{cases} 6.33 \times 10^{-8} \text{ cm}^2/\text{bit} & (\text{upper}) \\ 2.33 \times 10^{-8} \text{ cm}^2/\text{bit} & (\text{lower}). \end{cases}$$

Recall that the brute-force method in Section IV produced the estimate $\sigma_{AVG} \approx 6.27 \times 10^{-8}$, which is closer to the above upper bound than the lower bound. As pointed out in the last paragraph in Section VI-A, this is merely an artifact of compatibility between extrapolations, so it is not clear whether the above upper bound or lower bound is the more accurate estimate. However, if we take the geometric mean of the two estimates, to get 3.84×10^{-8} as the final estimate, this estimate is within a factor of 2 of either bound.

VII. FITTING DATA TO A PHYSICAL MODEL

The previous sections were essentially data processing, the processing needed to convert empirical cross section data into rate estimates, without any benefits from physical models. This section derives another data fitting method, but in this case the curve fit is derived from a proposed device-physics model. Physical models may have some ability to predict the effect that changes in device design (such as node-to-node separation, epi thickness, or critical charge of one or both nodes) have on the dual-node SEE susceptibility. The physical model is first stated for a single node and then applied to the dual-node problem.

A. Statement of the Model for Single Nodes

We start with a fairly generic physical model, which assumes that there is a charge-collection-efficiency function associated with each node. To be more specific, let us select a single node and call it the “node of interest” (dual nodes will be considered later). Consider an increment of charge liberated at a point (x,y,z) in the device interior. Some fraction of this charge will be collected by the node of interest, but this fraction depends on the location of the charge liberation. This fraction is denoted $\Omega(x,y,z)$ and will be called the charge-collection-efficiency function for the node of interest. Note that charge collection often involves nonlinear transport processes, but it has been argued (see discussions of the “JBA property” and “Q-flexibility property” in [5]) that the assumed existence of a charge-collection-efficiency function can still be a useful approximation even when nonlinear effects are involved. Therefore, a reasonably well-defined charge collection efficiency function is assumed here. The analysis will not require that an explicit expression for this function be known.

The charge-collection-efficiency function for the node of interest depends not only on the physical construction of the node of interest, but also on other structures (e.g., other nodes, or ohmic contacts that serve as sink-like boundaries for charge carriers) because charge removed by other structures influences the amount of charge that is available for collection by the node of interest. For example, if the node of interest is surrounded by a dense array of other charge-collecting nodes, the charge-collection-efficiency function for the node of interest tends to be localized to within a small distance from the node of interest, because charge liberated at larger distances is primarily collected by the surrounding nodes. The influence, that neighboring structures have on the charge-collection-efficiency function, was illustrated in [1] for several hypothetical examples in which charge collection is by diffusion (so the charge-collection-efficiency function can be calculated analytically). For some examples, in which the node of interest is relatively isolated from other structures, the family of constant- Ω surfaces roughly resembles a family of concentric hemispheres below the upper device plane (see Fig. 3 in [1]). For some other examples, in which the node of interest is surrounded by nearby sink-like boundaries, a constant- Ω surface roughly resembles a closed ellipsoid centered on a horizontal plane that is some suitable depth below the upper device plane (see Fig. 6c in [1]).

Of the two cases mentioned above, the one that is most easily treated analytically is that in which constant- Ω surfaces are closed ellipsoids. This assumption, combined with an additional simplifying approximation used in [8], produced a model for single-node SEU cross sections that can be made to agree with measured data ([8], [15]) when adjustable fitting parameters are suitably selected. Motivated by past success, the same simplifying assumption used in [8] will also be used here. This assumption is that the actual Ω -function can be approximated well enough, for the purpose of fitting the directional dependence of cross section data, by taking the family of constant- Ω surfaces to be a family of concentric ellipsoids, having a common center point and a common pair of eccentricities. Using these approximations, and with the coordinate system selected so that the origin is centered below the node of interest, and at some suitably selected depth, the family of constant- Ω surfaces for the node of interest is the family of ellipsoids given by

$$A^2 x^2 + B^2 y^2 + z^2 = \text{constant} \quad (\text{defines a constant-}\Omega \text{ surface}) \quad (15)$$

where A and B are adjustable parameters to be selected to conform to the device construction (the parameters used here are distinct from, and should not be confused with, the A parameter in Section VI). Smaller values of A and B produce flatter ellipsoids and would be expected for devices having thinner epi layers, while larger values would be appropriate for thicker epi layers.

Using the above approximations, the function $\Omega(x,y,z)$ is some suitably selected function of the left side of (15). An alternate statement of the assumptions is that there exists parameters A and B , an origin location, and a function F , having the property that the approximation

$$\Omega(x, y, z) \approx F\left(A^2 x^2 + B^2 y^2 + z^2\right) \quad (\text{alternate statement of the assumptions}) \quad (16)$$

is acceptable for the purpose of estimating the directional dependence of the cross section. It is not required that the function F or origin location be known; it is only required that such entities satisfying (16) exist. The analysis given here applies to those device designs in which (16) has acceptable accuracy when evaluated at the best-fitting F , A , B , and origin location.

For a given beam LET L , tilt angle θ , and rotation angle φ , the occurrence of a single-node SEU in the node of interest depends on the ion hit location. The hit location can be described by the x and y coordinates where the trajectory intersects the $z = 0$ plane (recall that the $z = 0$ plane may be some depth below the top of the device, as needed to maximize the accuracy of (16)). It was shown in [8] that, when (16) applies, an SEU occurs in the node of interest if and only if the hit location (x,y) satisfies

$$A^2 x^2 + B^2 y^2 - \frac{\sin^2 \theta}{\alpha^2(\theta, \varphi)} (A^2 x \cos \varphi + B^2 y \sin \varphi)^2 < \frac{AB}{\pi} \sigma_N \left(\frac{L}{\alpha(\theta, \varphi)} \right) \quad (17)$$

where $\sigma_N(L)$ is the normal-incident ($\theta = 0$) cross section as a function of LET L , so the right side contains the normal-incident cross section evaluated at an adjusted LET. The adjustment is through the factor α defined by

$$\alpha(\theta, \varphi) \equiv \sqrt{(A^2 \cos^2 \varphi + B^2 \sin^2 \varphi) \sin^2 \theta + \cos^2 \theta} . \quad (18)$$

For the special case of a symmetric Ω (i.e., $A=B$), it is not difficult to show that (17) defines the interior of an ellipse with the long axis making an angle φ (the beam rotation angle) with the x-axis. The geometry of this ellipse for the symmetric case is illustrated in Fig. 9, where L' in the figure is L/α . If $A \neq B$, the angle that the long axis of the ellipse makes with the x-axis becomes more complex and depends on the tilt angle θ . However, it is still possible to calculate the area enclosed by the ellipse. This area projected in the beam direction (i.e., multiplied by the absolute value of $\cos\theta$) is the directional cross section, and it was shown in [8] that this cross section satisfies the ‘‘alpha-law,’’ which is

$$\sigma(L, \theta, \varphi) = \alpha(\theta, \varphi) \sigma_N(L/\alpha(\theta, \varphi)). \quad (19)$$

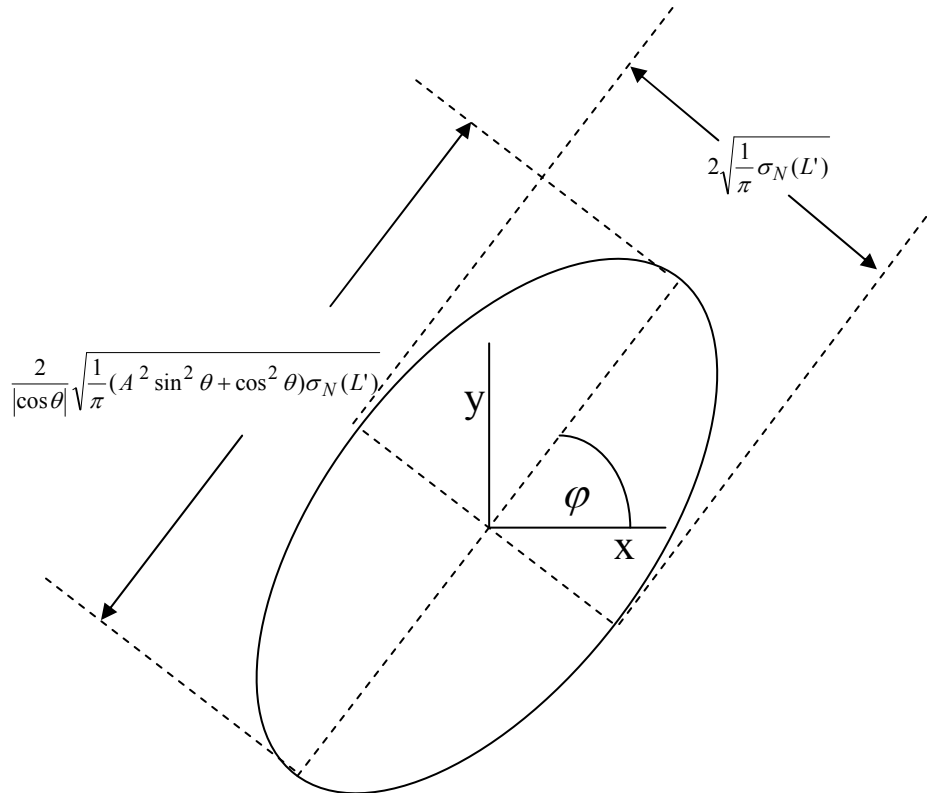


Fig.9. The ion hit location is described by the (x,y) coordinates of the point where the trajectory intersects the $z=0$ plane (which may be below the upper device plane). The hit locations that produce a single-node upset in a node laterally centered on the origin is the set of (x,y) points enclosed by the ellipse. The symmetric ($A = B$) single-node case is illustrated. This ellipse should not be confused with a constant- Ω surface, which is a three-dimensional ellipsoid that does not depend on the trajectory angles θ or φ . The ellipse shown is an upset region which does depend on θ and φ .

For later use, it is convenient to use (19) to express (17) in terms of the directional cross section to get

$$A^2 x^2 + B^2 y^2 - \frac{\sin^2 \theta}{\alpha^2(\theta, \varphi)} (A^2 x \cos \varphi + B^2 y \sin \varphi)^2 < \frac{AB}{\pi} \frac{\sigma(L, \theta, \varphi)}{\alpha(\theta, \varphi)}. \quad (20)$$

Although incidental, it is interesting that the alpha-law (19) does not explicitly show the function F appearing in (16). The normal-incident cross section as a function of LET implicitly contains all required information about F for the purpose of calculating the single-node directional cross section via (19). In other words, specifying the normal-incident cross section as a function of LET is an alternative to specifying the function F . This is the reason that the theory never required an explicit expression for F .

B. The Dual-Node Problem

We now consider dual-node upsets in two nodes called Node 1 and Node 2. Each has its own Ω -function, and each has its own region (points in the x-y plane) of susceptibility such as the elliptical region illustrated in Fig. 9, but one region is translated relative to the other by an amount that reflects the node-to-node separation. This separation is denoted T . To simplify the analysis, we assume that one of these two nodes has the property that the A and B parameters for this node has a much stronger influence on the directional dependence of the dual-node cross section than the A and B parameters for other node. This means that both nodes can be assigned the same A and B parameters providing that these parameters agree with the node having the greatest influence. Stated another way, it is assumed that a single pair of A and B parameters will adequately describe the dual-node cross section if the parameters are selected to produce the best fit with measured dual-node cross section data. The two regions of susceptibility then become geometrically similar ellipses. However, we do allow for the possibility that the two nodes are treated differently by the device circuitry (i.e., they do not necessarily have the same critical charges for upset), so the single-node cross sections may differ, i.e., the ellipses may be of different sizes. The intersection of these regions is the region of dual-node susceptibility.

To calculate the dual-node cross section, we first apply (20) to each node. As previously stated, the A , B , and α are taken to be the same for each, but we do allow for different single-node cross sections on the right side of (20) so we use subscripts to distinguish between the two. We start with Node 1 and select the origin to be centered on this node so the single-node upset region is given by

$$A^2 x^2 + B^2 y^2 - \frac{\sin^2 \theta}{\alpha^2(\theta, \varphi)} (A^2 x \cos \varphi + B^2 y \sin \varphi)^2 < \frac{AB}{\pi} \frac{\sigma_1(L, \theta, \varphi)}{\alpha(\theta, \varphi)}. \quad (21)$$

Suppose (for now) that Node 2 is in the same plane as Node 1, but displaced a positive distance T along the x-axis (the coordinate system is oriented so that the x-axis connects

the two nodes) relative to Node 1. Using the same coordinate system that was used for Node 1, the single-node upset region for Node 2 is given by

$$A^2(x-T)^2 + B^2y^2 - \frac{\sin^2 \theta}{\alpha^2(\theta, \varphi)} (A^2(x-T) \cos \varphi + B^2y \sin \varphi)^2 < \frac{AB \sigma_2(L, \theta, \varphi)}{\pi \alpha(\theta, \varphi)}.$$

Recall that the depth of the horizontal plane was selected to make (16) the best fit. This depth need not be the same for the two nodes, so we now allow Node 2 to be displaced vertically by an amount h (which is a fitting parameter) relative to Node 1. Using more precise terminology, the centroid of the Ω -function for Node 2 is displaced relative to the centroid of the Ω -function for Node 1. Note that h can be positive or negative depending on which node is above the other. The condition for upsetting Node 2 is as given above, except that the coordinates now describe hit locations in the vertically displaced plane. The condition becomes

$$A^2(\bar{x}-T)^2 + B^2\bar{y}^2 - \frac{\sin^2 \theta}{\alpha^2(\theta, \varphi)} (A^2(\bar{x}-T) \cos \varphi + B^2\bar{y} \sin \varphi)^2 < \frac{AB \sigma_2(L, \theta, \varphi)}{\pi \alpha(\theta, \varphi)} \quad (22)$$

where (\bar{x}, \bar{y}) is the point where the ion trajectory intersects the vertically displaced plane. But a trajectory described by θ and φ that intersects the displaced plane at the point (\bar{x}, \bar{y}) also intersects the original plane at the point (x, y) satisfying

$$\bar{x} = x - h \tan \theta \cos \varphi, \quad \bar{y} = y - h \tan \theta \sin \varphi. \quad (23)$$

Using the same coordinate system as for Node 1, the hit locations in the original plane that upset Node 2 are the points (x, y) satisfying (22) and (23), i.e.,

$$A^2(x-b_1)^2 + B^2(y-b_2)^2 - \frac{\sin^2 \theta}{\alpha^2(\theta, \varphi)} [A^2(x-b_1) \cos \varphi + B^2(y-b_2) \sin \varphi]^2 < \frac{AB \sigma_2(L, \theta, \varphi)}{\pi \alpha(\theta, \varphi)} \quad (24)$$

where

$$b_1 \equiv h \tan \theta \cos \varphi + T, \quad b_2 \equiv h \tan \theta \sin \varphi. \quad (25)$$

The set of points satisfying (21) is the region of susceptibility for Node 1, and the set of points satisfying (24) is the region of susceptibility for Node 2. The area of the intersection region, projected in the beam direction (i.e., multiplied by the absolute value of $\cos \theta$), is the directional cross section for dual-node upsets, i.e.,

$$\sigma(L, \theta, \varphi) = |\cos \theta| \iint_{\mathcal{R}} dx dy \quad (26)$$

where

$$\mathcal{R} \equiv \text{intersection of the two point sets defined by (21) and (24)}. \quad (27)$$

A change in variables makes the integral in (26) easier to evaluate. A new pair of coordinates X and Y is defined by the linear (but not a rotation) transformation

$$x = \left(\frac{A B}{A^2 \cos^2 \varphi + B^2 \sin^2 \varphi} \right)^{1/2} \left(\sqrt{\alpha(\theta, \varphi)} \frac{\cos \varphi}{\cos \theta} X - \frac{B \sin \varphi}{A \sqrt{\alpha(\theta, \varphi)}} Y \right) \quad (28a)$$

$$y = \left(\frac{A B}{A^2 \cos^2 \varphi + B^2 \sin^2 \varphi} \right)^{1/2} \left(\sqrt{\alpha(\theta, \varphi)} \frac{\sin \varphi}{\cos \theta} X + \frac{A \cos \varphi}{B \sqrt{\alpha(\theta, \varphi)}} Y \right). \quad (28b)$$

The condition (21) can be expressed in terms of X and Y via the substitution (28), but the algebra will be less cumbersome if we first use (28) to derive two preliminary results, which are

$$A^2 x^2 + B^2 y^2 = A B \left(\frac{\alpha(\theta, \varphi)}{\cos^2 \theta} X^2 + \frac{Y^2}{\alpha(\theta, \varphi)} \right) \quad (29a)$$

$$A^2 x \cos \varphi + B^2 y \sin \varphi = [(A^2 \cos^2 \varphi + B^2 \sin^2 \varphi) A B \alpha(\theta, \varphi)]^{1/2} \frac{X}{\cos \theta}. \quad (29b)$$

Substituting (29) into (21) while using (18) gives

$$X^2 + Y^2 < \frac{\sigma_1(L, \theta, \varphi)}{\pi} \quad (\text{condition for Node 1 upset}). \quad (30)$$

The condition (24) can be expressed in terms of X and Y via the substitution (28), but the algebra will be less cumbersome if we first define the transformed b_1 and b_2 , denoted B_1 and B_2 , and defined by

$$b_1 = \left(\frac{A B}{A^2 \cos^2 \varphi + B^2 \sin^2 \varphi} \right)^{1/2} \left(\sqrt{\alpha(\theta, \varphi)} \frac{\cos \varphi}{\cos \theta} B_1 - \frac{B \sin \varphi}{A \sqrt{\alpha(\theta, \varphi)}} B_2 \right) \quad (31a)$$

$$b_2 = \left(\frac{A B}{A^2 \cos^2 \varphi + B^2 \sin^2 \varphi} \right)^{1/2} \left(\sqrt{\alpha(\theta, \varphi)} \frac{\sin \varphi}{\cos \theta} B_1 + \frac{A \cos \varphi}{B \sqrt{\alpha(\theta, \varphi)}} B_2 \right). \quad (31b)$$

Note that (29) is implied by the transformation (28), which is the same transformation as (31), so the same linear transformation also relates the pair of numbers $x - b_1$ and $y - b_2$ to the pair $X - B_1$ and $Y - B_2$. Therefore, another version of (29) is

$$A^2 (x - b_1)^2 + B^2 (y - b_2)^2 = A B \left(\frac{\alpha(\theta, \varphi)}{\cos^2 \theta} (X - B_1)^2 + \frac{(Y - B_2)^2}{\alpha(\theta, \varphi)} \right)$$

$$A^2 (x - b_1) \cos \varphi + B^2 (y - b_2) \sin \varphi = [(A^2 \cos^2 \varphi + B^2 \sin^2 \varphi) A B \alpha(\theta, \varphi)]^{1/2} \frac{X - B_1}{\cos \theta}.$$

Substituting these results into (24) while using (18) gives

$$(X - B_1)^2 + (Y - B_2)^2 < \frac{\sigma_2(L, \theta, \varphi)}{\pi} \quad (\text{condition for Node 2 upset}). \quad (32)$$

The condition for a dual-node upset consists of the simultaneous conditions (30) and (32), i.e.,

$$X^2 + Y^2 < R_1^2, \quad (X - B_1)^2 + (Y - B_2)^2 < R_2^2 \quad (33)$$

where

$$R_1 \equiv \left[\frac{\sigma_1(L, \theta, \varphi)}{\pi} \right]^{1/2}, \quad R_2 \equiv \left[\frac{\sigma_2(L, \theta, \varphi)}{\pi} \right]^{1/2}. \quad (34)$$

Recall that the purpose of the coordinate transformation from (x, y) to (X, Y) was to assist in the evaluation of the integral in (26). A change in variables is made using

$$\iint_{\mathcal{R}} dx dy = \iint_{\bar{\mathcal{R}}} J dX dY \quad (35a)$$

where J is the Jacobian of the transformation and $\bar{\mathcal{R}}$ with the bar is the region in the XY plane satisfying (33). The Jacobian is given by

$$J = \left| \frac{\partial x}{\partial X} \frac{\partial y}{\partial Y} - \frac{\partial x}{\partial Y} \frac{\partial y}{\partial X} \right|$$

and using the transformation (28) to calculate the derivatives gives

$$J = \frac{1}{|\cos \theta|}. \quad (35b)$$

Also, the integral on the right side of (35a) with the Jacobian omitted is the area of the intersection of the two circular regions indicated in (33). This gives

$$\iint_{\overline{\mathcal{R}}} dX dY = I(R_1, R_2, D) \quad (35c)$$

where I is the intersection area defined by

$$I(R_1, R_2, D) \equiv \begin{cases} \text{Area of intersection of two circular regions} \\ \text{with one having radius } R_1 \text{ and the other having} \\ \text{radius } R_2 \text{ and with a distance } D \text{ between centers.} \end{cases} \quad (36)$$

Appendix C gives a formula for calculating I . The distance D between centers is calculated from

$$D = \sqrt{B_1^2 + B_2^2}. \quad (37)$$

Combining the three equations in (35) with (26) gives

$$\sigma(L, \theta, \varphi) = I(R_1, R_2, D). \quad (38)$$

Explicit equations for calculating the R_1 and R_2 appearing in (38) are given in (34), but D is still obscure because explicit equations are still needed for the B_1 and B_2 appearing in (37). Inverting the transformation (31) gives

$$B_1 = \frac{\cos \theta}{\sqrt{A B \alpha(\theta, \varphi)}} \frac{A^2 b_1 \cos \varphi + B^2 b_2 \sin \varphi}{\sqrt{A^2 \cos^2 \varphi + B^2 \sin^2 \varphi}}$$

$$B_2 = \sqrt{A B \alpha(\theta, \varphi)} \frac{b_2 \cos \varphi - b_1 \sin \varphi}{\sqrt{A^2 \cos^2 \varphi + B^2 \sin^2 \varphi}}$$

so (37) becomes

$$D^2 = \frac{\cos^2 \theta [A^2 b_1 \cos \varphi + B^2 b_2 \sin \varphi]^2 + A^2 B^2 \alpha^2(\theta, \varphi) [b_2 \cos \varphi - b_1 \sin \varphi]^2}{A B \alpha(\theta, \varphi) (A^2 \cos^2 \varphi + B^2 \sin^2 \varphi)}$$

and combining this with (18) and (25) gives

$$D^2 = \frac{\alpha^2(\theta, \varphi) - \cos^2 \theta}{A B \alpha(\theta, \varphi)} h^2 + \frac{2A}{B \alpha(\theta, \varphi)} \cos \theta \sin \theta \cos \varphi h T + \frac{A}{B \alpha(\theta, \varphi)} (B^2 \sin^2 \theta \sin^2 \varphi + \cos^2 \theta) T^2. \quad (39)$$

When used together with (34) and (39), (38) expresses the dual-node directional cross section in terms of the two single-node directional cross sections, but a calculation of the latter cross sections is still needed. The ‘‘alpha-law’’ (19) calculates the directional cross sections from the normal-incident cross sections, so all that is needed is a fitting function for each normal-incident cross section. Experience has found that the two-parameter fit derived in [3] often (not always) fits measured data at least as well as (and sometimes better than) the four-parameter Weibull function. This fit has the form

$$\sigma_N(L) = \sigma_{sat} \exp\left(-\frac{L_{1/e}}{L}\right)$$

where the constants σ_{sat} and $L_{1/e}$ are adjustable fitting parameters. This type of fit does not always give good agreement with measured data, so we will increase the flexibility by including one additional fitting parameter P and use the fit

$$\sigma_N(L) = \sigma_{sat} \exp\left(-\left[\frac{L_{1/e}}{L}\right]^P\right).$$

For the dual-node problem consisting of two single nodes, we need two sets of fitting parameters, one for each of the two single-node cross sections. To shorten the notation, we write σ_0 and L_0 instead of σ_{sat} and $L_{1/e}$, and then include an additional subscript to distinguish between the two nodes. The same P will be used for both, so the fits become

$$\sigma_{N,1}(L) = \sigma_{0,1} \exp\left(-\left[\frac{L_{0,1}}{L}\right]^P\right), \quad \sigma_{N,2}(L) = \sigma_{0,2} \exp\left(-\left[\frac{L_{0,2}}{L}\right]^P\right). \quad (40)$$

Using (19) with (40), the directional cross sections are calculated from

$$\sigma_1(L, \theta, \varphi) = \sigma_{0,1} \alpha(\theta, \varphi) \exp\left(-\left[\frac{L_{0,1} \alpha(\theta, \varphi)}{L}\right]^P\right)$$

$$\sigma_2(L, \theta, \varphi) = \sigma_{0,2} \alpha(\theta, \varphi) \exp\left(-\left[\frac{L_{0,2} \alpha(\theta, \varphi)}{L}\right]^P\right).$$

C. Summary of the Final Equations

The important equations are surrounded by derivations in the above paragraphs, so they are repeated here for easy reference. The model contains a number of fitting parameters. One possible objective is to find the optimum values for these parameters by assigning trial values and then comparing measured cross section data to the model-predicted directional cross section. Another possible objective is to calculate the model-predicted directional cross section after optimum values have already been found and assigned to the fitting parameters. In either case, numerical values (either trial values or optimum values) have been assigned to the fitting parameters, and the goal is to calculate the directional cross section. A recipe is given here for calculating the directional cross section after values have been assigned to the fitting parameters.

Recall that the x-axis used in the theory connects node centers, and the rotation angle is measured from this line. Depending on the individual example, the rotation angle reported in the laboratory data may or may not be measured from this same line. If not, then before comparing predictions to measurements, the rotation angle in the laboratory data should be converted, by adding or subtracting a constant “off-set angle,” to obtain an “adjusted rotation angle” that conforms to the theory. This off-set angle, denoted φ_{off} , is a fitting parameter that was not previously mentioned. In all discussions below, the rotation angle reported with the laboratory data is denoted φ_{data} , and the adjusted rotation angle that conforms to the theory is denoted φ .

The fitting parameters that appear in the equations below are φ_{off} , A , B , $L_{0,1}$, $L_{0,2}$, $\sigma_{0,1}$, $\sigma_{0,2}$, P , and h . It is assumed that an estimate is available for the node-to-node separation T (if no estimate is available, then T becomes another fitting parameter). The arguments at which the directional cross section is evaluated are L , θ , and φ_{data} . After assigning numerical values to each of these thirteen quantities, the dual-node directional cross section is calculated by solving for each quantity in the order they are listed in the equations

$$\varphi = \varphi_{off} + \varphi_{data} \quad (41)$$

$$\alpha(\theta, \varphi) \equiv \sqrt{(A^2 \cos^2 \varphi + B^2 \sin^2 \varphi) \sin^2 \theta + \cos^2 \theta} \quad (42)$$

$$\sigma_1(L, \theta, \varphi) = \sigma_{0,1} \alpha(\theta, \varphi) \exp\left(-\left[\frac{L_{0,1} \alpha(\theta, \varphi)}{L}\right]^P\right) \quad (43a)$$

$$\sigma_2(L, \theta, \varphi) = \sigma_{0,2} \alpha(\theta, \varphi) \exp\left(-\left[\frac{L_{0,2} \alpha(\theta, \varphi)}{L}\right]^P\right). \quad (43b)$$

$$R_1(L, \theta, \varphi) \equiv \left[\frac{\sigma_1(L, \theta, \varphi)}{\pi}\right]^{1/2}, \quad R_2(L, \theta, \varphi) \equiv \left[\frac{\sigma_2(L, \theta, \varphi)}{\pi}\right]^{1/2}. \quad (44)$$

$$D(\theta, \varphi) = \left[\frac{\alpha^2(\theta, \varphi) - \cos^2 \theta}{A B \alpha(\theta, \varphi)} h^2 + \frac{2A}{B \alpha(\theta, \varphi)} \cos \theta \sin \theta \cos \varphi h T \right. \\ \left. + \frac{A}{B \alpha(\theta, \varphi)} (B^2 \sin^2 \theta \sin^2 \varphi + \cos^2 \theta) T^2 \right]^{1/2} \quad (45)$$

$$\sigma(L, \theta, \varphi) = I(R_1(L, \theta, \varphi), R_2(L, \theta, \varphi), D(\theta, \varphi)) \quad (46)$$

where the function I is defined by (36) and is calculated in Appendix C.

VIII. CODES AND AN EXAMPLE

This section gives a step-by-step recipe for converting test data into rate predictions. The recipe is based on fitting data to the physical model in Section VII, but it is not necessary for the reader to follow the mathematical details that were given there because the calculations can be done using codes provided here. An example device is used for illustration. This is an early version of the device that Xilinx has labeled SRAM6 with the $2\mu\text{m}$ node-to-node separation (T), $2\mu\text{m}$ epi thickness, and 65nm feature size. Test data provided by Xilinx for this early version were obtained from a test performed on May 25, 2007. The device was tested in two bit patterns. An inspection of the data shows that the device is very much harder in the 0-state than in the 1-state. The softer 1-state was selected for rate calculations, and provides a worst-case rate estimate for an arbitrary bit pattern. The example environment is galactic cosmic rays in interplanetary space during the solar minimum time period. By using this example as a template, similar calculations can be performed for other devices in which similar types of measured data sets are available.

The recipe uses several tools but does not include tutorials on the general use of these tools. One of these tools is SigmaPlot, which is a commercial spreadsheet software package. To use the recipe, the user is required to be able to perform certain tasks, which are:

- (a) Open and edit a SigmaPlot worksheet.
- (b) Open, edit, and run a SigmaPlot Regression Wizard file.
- (c) Open, edit, and run a SigmaPlot Transform.
- (d) Convert a FORTRAN source code (hard copy is provided) into an executable file.
- (e) Obtain environmental flux data (e.g., from CREME96) if the environment of interest is not the one included in the example, and interpolate the table so that the flux is evaluated at selected LETs.

The model contains several fitting parameters that are selected to fit data. The parameters were previously defined but a review is given as a reminder. The node-to-node separation T is regarded as given so it is not included as a fitting parameter. The others discussed below are fitting parameters.

The A and B parameters are measures of the eccentricities of the single-node charge-collection efficiency functions, and control the directional dependence of the single-node cross sections. If we make an analogy with the more familiar RPP model (a visualization aid), A is analogous to the RPP dimension ratio Z/X , and B is analogous to the RPP dimension ratio Z/Y . If $A \ll 1$ and $B \ll 1$, an approximate cosine law applies to the single-node cross sections. If $A = B = 1$, the single-node cross sections are isotropic, although there will still be a directional dependence in the dual-node cross section associated with the degree of alignment between the ion trajectory and the line connecting the nodes. The directional dependence of the dual-node cross section depends on the alignment between the beam and the node-connecting-line, and on the directional dependence of each of the two single-node cross sections. It was assumed that the strongest control over the dual-node directional dependence comes from two of these

factors; the beam alignment, and the directional dependence of that single node having the strongest directional dependence. Therefore, the same A and B parameters are used for both nodes. The offset rotation angle is used to compensate for the possibility that the rotation angle reported with the laboratory test data might not be measured from the same reference line as assumed in the theory (the reference line used in the theory connects node centers). The parameters $L_{0,1}$, $L_{0,2}$, $\sigma_{0,1}$, $\sigma_{0,2}$, and P describe the normal-incident cross sections for the two single nodes as given by (40). Finally, the parameter h is the height difference between the centroids of the two single-node charge collection efficiency functions, and can be positive or negative.

The step-by-step recipe is as follows:

Step 1: Enter Data into a Worksheet

Data for the 65nm SRAM6 (early version) in the all-1's pattern, provided by Xilinx, are shown in Fig. 10. Run numbers and part numbers in the first two columns are not essential (part numbers are not listed in Fig. 10) but might be desired so that points can easily be traced to the test log in case questions arise. The measured data are entered in Columns 3 through 6. The LET is particle LET (not effective LET) in units of MeV-cm²/mg. The rotation and tilt angles are entered in degrees. The cross section in Column 6 is the measured directional cross section and is entered in the units of $\mu\text{m}^2/\text{bit}$. These units were selected because the Regression Wizard appears to be more temperamental when working with the extreme powers of ten that accompany the cm² units, but less temperamental when working with the more modest powers of ten that accompany the μm^2 units.

Fig. 10. Measured Data for an Early Version of SRAM6 in all-1's.

	1-Run #	2-Part #	3-LET	4-Rotation	5-Tilt	6-XS ($\mu\text{m}^2/\text{bit}$)
1	573		58.70	180	70	3.45e-1
2	575		31.30	180	70	2.58e-1
3	578		31.30	180	0	6.10e-4
4	579		21.00	180	0	0.000
5	580		21.00	180	0	0.000
6	583		21.00	180	0	2.29e-5
7	584		21.00	180	15	0.000
8	586		21.00	180	25	0.000
9	588		21.00	180	35	3.05e-5
10	590		21.00	180	45	1.28e-3
11	592		21.00	180	55	3.05e-2
12	595		21.00	180	65	9.61e-2
13	596		21.00	180	65	1.00e-1
14	597		21.00	180	75	1.17e-1
15	603		21.00	180	75	1.09e-1
16	605		9.70	180	75	7.11e-2
17	606		9.70	180	0	0.000
18	608		3.40	180	0	0.000
19	609		3.40	180	75	2.46e-2

	1-Run #	2-Part #	3-LET	4-Rotation	5-Tilt	6-XS ($\mu\text{m}^2/\text{bit}$)
20	614		3.40	170	75	1.55e-2
21	615		3.40	160	75	9.46e-3
22	617		3.40	150	75	3.36e-3
23	620		3.40	140	75	4.58e-4
24	621		3.40	130	75	0.000
25	623		3.40	190	75	1.42e-2
26	625		3.40	200	75	1.00e-2
27	626		3.40	210	75	2.82e-3
28	627		3.40	220	75	2.75e-4
29	628		3.40	230	75	7.63e-6
30	629		3.40	240	75	0.000
31	630		3.40	250	75	7.63e-6
32	631		3.40	260	75	0.000
33	632		3.40	270	75	0.000
34	633		3.40	280	75	0.000
35	634		3.40	290	75	0.000
36	635		3.40	300	75	0.000
37	636		3.40	310	75	2.29e-5
38	637		3.40	320	75	2.44e-4
39	638		3.40	330	75	3.03e-3
40	639		3.40	340	75	9.70e-3
41	640		3.40	350	75	1.29e-2
42	641		3.40	360	75	2.26e-2
43	642		3.40	370	75	1.29e-2
44	643		3.40	380	75	9.18e-3
45	644		3.40	390	75	3.17e-3
46	645		3.40	400	75	5.26e-4
47	646		3.40	410	75	3.05e-5
48	647		3.40	420	75	0.000
49	648		3.40	430	75	0.000
50	649		3.40	440	75	0.000
51	650		3.40	90	75	0.000
52	651		3.40	100	75	0.000
53	652		3.40	110	75	0.000
54	653		3.40	120	75	0.000
55	654		3.40	130	75	7.63e-6
56	655		3.40	180	75	2.29e-2
57	656		3.40	180	75	2.49e-2
58	657		3.40	180	70	1.07e-2
59	658		3.40	180	65	3.27e-3
60	659		3.40	180	60	3.36e-4
61	660		3.40	180	60	4.27e-4
62	661		3.40	180	55	9.16e-5
63	662		3.40	180	50	2.54e-5
64	663		3.40	180	45	1.02e-5
65	664		3.40	180	35	0.000
66	665		3.40	180	25	0.000
67	666		3.40	180	15	0.000

	1-Run #	2-Part #	3-LET	4-Rotation	5-Tilt	6-XS ($\mu\text{m}^2/\text{bit}$)
68	667		3.40	180	0	0.000
69	668		2.22	180	60	5.59e-5
70	669		2.22	180	65	1.88e-4
71	670		2.22	180	70	5.16e-3
72	671		2.22	180	75	9.81e-3
73	672		2.22	190	75	5.32e-3
74	673		2.22	160	75	3.22e-3
75	674		2.22	150	75	7.93e-4
76	675		2.22	140	75	5.34e-5
77	676		2.22	190	75	5.91e-3
78	677		2.22	190	75	5.16e-3
79	678		2.22	200	75	2.43e-3
80	679		2.22	210	75	6.87e-4
81	680		2.22	220	75	4.58e-5
82	681		2.22	230	75	0.000
83	682		2.22	240	75	0.000
84	683		2.22	270	75	0.000
85	684		2.22	300	75	0.000
86	685		2.22	310	75	1.53e-5
87	686		2.22	320	75	6.10e-5
88	687		2.22	330	75	7.63e-4
89	688		2.22	345	75	3.77e-3
90	689		2.22	360	75	9.08e-3
91	690		2.22	375	75	4.29e-3
92	691		2.22	390	75	8.70e-4
93	692		2.22	405	75	1.53e-5
94	693		2.22	420	75	0.000
95	694		2.22	435	75	0.000
96	695		0.87	390	75	3.05e-5
97	696		0.87	375	75	1.98e-4
98	697		0.87	360	75	2.29e-4
99	698		0.87	345	75	1.83e-4
100	699		0.87	330	75	3.05e-5
101	700		0.87	180	75	3.97e-4
102	701		0.87	165	75	1.53e-4
103	702		0.87	195	75	1.07e-4
104	703		0.87	180	70	9.16e-5
105	704		0.87	180	65	0.000
106	705		0.87	180	60	0.000

Step 2: Extract the Fitting Parameters

The Regression Wizard is used to find the fitting parameters that produce the best (as defined by some error measure) fit between model predictions and data. A hard copy of the programming is listed in Appendix D. The user can type this in at the keyboard. Before running the Regression Wizard, verify that the trig button is set for radians (needed for inverse trig functions called by the program). The code recognizes that angles in the worksheet are in degrees and makes the necessary conversions within the program.

The Regression Wizard searches for a local minimum in a weighted least square error, with a weight specified by the user. The weight factor already included in the program in Appendix D warrants some explanation. Some investigators have argued that a plot of cross section versus LET should be done using a linear scale for the cross section because the smaller LETs, at which the cross section is too small to have adequate resolution when using a linear scale, do not make a significant contribution to the upset rate. This argument may have some validity with the more traditional single-node problem that roughly satisfies a “cosine law” because the dominant contribution from the smaller-LET particles is from the subset that hit the device at large tilt angles, producing a large effective LET. However, the cross section that will be used here for rate calculations is a directional-average cross section which is integrated with the raw flux in (3) (“raw flux” as opposed to an “effective flux” that has an assumed directional dependence of the device already built into the flux) to produce an upset rate. Small cross sections at low LET are important if the raw flux at low LET is correspondingly large. In fact, it will be seen later that the smaller LETs have the greatest influence on the estimated SEU rate, so the weight factor was selected to favor the smaller LETs. Numerical investigations have found that a $1/L^3$ weighting results in the fits having the best conformity to the data on the most relevant range of LETs, and this is the weighting used in the program in Appendix D.

The only portion of Appendix D that is expected to require editing for different examples is the “Initial Parameters” section which assigns an initial guess to the fitting parameters, but this often requires editing for each new example. The Regression Wizard finds a local minimum in the error measure. If the initial guess is unlucky, the local minimum might not be even remotely close to the global minimum (the user will become aware of this in Step 3). Some trial and error with the initial guess is sometimes needed before an acceptable fit is obtained. When an initial guess is tried, one of two outcomes are commonly encountered. The first outcome is the message “convergence with no parameter changes” returned by the Regression Wizard. This will occur if the initial guess produces a cross section that is zero, or small enough to be indistinguishable from zero, for each data point. If neighboring parameters selected by the Regression Wizard produce the same result, the Regression Wizard detects no change in the error measure when changing parameters, so the Regression Wizard concludes that the initial guess is already at a relative minimum. When this problem is encountered, the initial guess should be changed to one that produces larger cross sections (e.g., decrease one or more of the parameters $L_{0,1}$, $L_{0,2}$, or P). The other likely outcome is that the Regression Wizard will find a true relative minimum in the error measure. However, this might not be the global

minimum. When the Regression Wizard starts with an initial guess and then converges to final estimates for the fitting parameters, the final estimates will be listed together with a numerical value assigned to the “norm” (this is the error measure). It is recommended that this norm be recorded. Then try another initial guess and determine whether the final estimates for the parameters are the same as before. If not, then the estimates accompanied by the smaller norm are the better estimates. This process will have to be repeated whenever it is found that different initial guesses produce significantly different final estimates for the fitting parameters.

The above process was already done for the example considered here, and the initial parameters listed in Appendix D produce the best final values for the parameters. Running the Regression Wizard using the inputs in Appendix D together with the data in Fig. 10 produces the final parameter values shown in Table 2.

Table 2. Final parameters returned by the Regression Wizard for an early version of SRAM6 in all-1's

A = 0.2234	B = 0.6953
L01 = 0	L02 = 43.85
S01 = 2.914	S02 = 1.215
phi_off = 1.685e-2	h = 6.583e-3
P = 0.7075	

Although T is assumed known in this example, it is tempting to include T as another adjustable fitting parameter for fine tuning. Unfortunately, this produces a numerical problem for the example data set considered here. With T included as another fitting parameter, parameter determination becomes very weak in the sense that different parameter choices can produce different fits with one almost as good as another (a change in one parameter can be compensated by suitable changes in other parameters). Also, this creates a high density of relative minimums in the error measure, and the Regression Wizard will almost always find a relative minimum that does not even remotely resemble the global minimum. Very small changes in the initial guess can cause the Regression Wizard to converge to very different final results (in this example), and it is very unlikely that any final result will produce a good fit. If T is not known, or if fine tuning is desired, it is recommended that trial values for T be assigned manually in the equation section of the Regression Wizard, so that T is treated as a constant in the Regression Wizard calculations. By keeping a record of the values assigned to the norm in the Regression Wizard output, it is possible to identify the best fit. For the example outputs shown Table 2, T was set equal to $2\mu\text{m}$ without fine tuning.

Step 3: Compare Fits to Data and Modify as Needed

In view of the numerical issues discussed in Step 2, it is essential that fits be compared to data to verify that a good fit was actually found. The comparison is done here by constructing plots. We begin by plotting the data. Excluding the first three runs in Fig. 10, all other points can be represented by plots consisting of several rotation sweeps (the rotation angle is varied with tilt angle and LET fixed), several tilt sweeps (the tilt angle is varied with rotation angle and LET fixed), and an LET sweep (the LET is varied with

rotation angle and tilt angle fixed). Some of the data points will belong to more than one sweep. We first consider the rotation sweep at an LET of 3.4 and a 75° tilt angle. All of the points in Fig. 10 showing the stated LET and tilt are copied into another worksheet for plotting (it is actually easier to copy all entries and then delete the ones that do not belong). This produces Columns 1 through 6 in Fig. 11 (the other columns are explained later), which are used to plot the data as points by plotting Column 6 versus Column 4. The points are shown in Fig. 12 (the curves are explained later).

Fig. 11. A Rotation Sweep (data and fits) for an Early Version of SRAM6 in all-1's.

	1-Run #	2-Part #	3-LET	4-Rot	5-Tilt	6-XS Data	7-fit Rot	8-hi XS	9-nom XS
1	609		3.40	180	75	2.46e-2	90.0	0.00	0.00
2	614		3.40	170	75	1.55e-2	95.0	0.00	0.00
3	615		3.40	160	75	9.46e-3	100.0	0.00	0.00
4	617		3.40	150	75	3.36e-3	105.0	0.00	0.00
5	620		3.40	140	75	4.58e-4	110.0	0.000	0.000
6	621		3.40	130	75	0.000	115.0	0.000	0.000
7	623		3.40	190	75	1.42e-2	120.0	0.000	0.000
8	625		3.40	200	75	1.00e-2	125.0	0.000	0.000
9	626		3.40	210	75	2.82e-3	130.0	0.000	0.000
10	627		3.40	220	75	2.75e-4	135.0	0.000	0.000
11	628		3.40	230	75	7.63e-6	140.0	0.000	0.000
12	629		3.40	240	75	0.000	145.0	1.13e-3	2.48e-4
13	630		3.40	250	75	7.63e-6	150.0	3.80e-3	2.22e-3
14	631		3.40	260	75	0.000	155.0	7.64e-3	5.47e-3
15	632		3.40	270	75	0.000	160.0	1.24e-2	9.65e-3
16	633		3.40	280	75	0.000	165.0	1.75e-2	1.42e-2
17	634		3.40	290	75	0.000	170.0	2.21e-2	1.83e-2
18	635		3.40	300	75	0.000	175.0	2.51e-2	2.09e-2
19	636		3.40	310	75	2.29e-5	176.0	2.54e-2	2.12e-2
20	637		3.40	320	75	2.44e-4	177.0	2.56e-2	2.14e-2
21	638		3.40	330	75	3.03e-3	178.0	2.58e-2	2.15e-2
22	639		3.40	340	75	9.70e-3	179.0	2.58e-2	2.16e-2
23	640		3.40	350	75	1.29e-2	180.0	2.58e-2	2.15e-2
24	641		3.40	360	75	2.26e-2	181.0	2.57e-2	2.14e-2
25	642		3.40	370	75	1.29e-2	182.0	2.54e-2	2.12e-2
26	643		3.40	380	75	9.18e-3	183.0	2.51e-2	2.09e-2
27	644		3.40	390	75	3.17e-3	184.0	2.47e-2	2.05e-2
28	645		3.40	400	75	5.26e-4	185.0	2.41e-2	2.01e-2
29	646		3.40	410	75	3.05e-5	190.0	2.04e-2	1.68e-2
30	647		3.40	420	75	0.000	195.0	1.55e-2	1.25e-2
31	648		3.40	430	75	0.000	200.0	1.05e-2	7.95e-3
32	649		3.40	440	75	0.000	205.0	6.03e-3	4.09e-3
33	650		3.40	90	75	0.000	210.0	2.62e-3	1.29e-3
34	651		3.40	100	75	0.000	215.0	4.62e-4	0.000
35	652		3.40	110	75	0.000	220.0	0.000	0.000
36	653		3.40	120	75	0.000	225.0	0.000	0.000
37	654		3.40	130	75	7.63e-6	230.0	0.000	0.000

	1-Run #	2-Part #	3-LET	4-Rot	5-Tilt	6-XS Data	7-fit Rot	8-hi XS	9-nom XS
38	655		3.40	180	75	2.29e-2	235.0	0.000	0.000
39	656		3.40	180	75	2.49e-2	240.0	0.000	0.000
40							245.0	0.000	0.000
41							250.0	0.000	0.000
42							255.0	0.000	0.000
43							260.0	0.000	0.000
44							265.0	0.000	0.000
45							270.0	0.000	0.000
46							275.0	0.000	0.000
47							280.0	0.000	0.000
48							285.0	0.000	0.000
49							290.0	0.000	0.000
50							295.0	0.000	0.000
51							300.0	0.000	0.000
52							305.0	0.000	0.000
53							310.0	0.000	0.000
54							315.0	0.000	0.000
55							320.0	0.000	0.000
56							325.0	7.01e-4	3.40e-5
57							330.0	3.02e-3	1.60e-3
58							332.0	4.29e-3	2.63e-3
59							334.0	5.74e-3	3.83e-3
60							336.0	7.33e-3	5.20e-3
61							338.0	9.07e-3	6.71e-3
62							340.0	1.09e-2	8.33e-3
63							342.0	1.28e-2	1.00e-2
64							344.0	1.47e-2	1.17e-2
65							346.0	1.66e-2	1.34e-2
66							348.0	1.84e-2	1.50e-2
67							350.0	2.00e-2	1.65e-2
68							352.0	2.14e-2	1.77e-2
69							354.0	2.25e-2	1.87e-2
70							355.0	2.29e-2	1.91e-2
71							356.0	2.33e-2	1.94e-2
72							357.0	2.35e-2	1.96e-2
73							358.0	2.36e-2	1.97e-2
74							359.0	2.37e-2	1.98e-2
75							360.0	2.37e-2	1.97e-2
76							361.0	2.35e-2	1.96e-2
77							362.0	2.33e-2	1.94e-2
78							363.0	2.29e-2	1.91e-2
79							364.0	2.25e-2	1.87e-2
80							365.0	2.20e-2	1.83e-2
81							366.0	2.14e-2	1.78e-2
82							368.0	2.01e-2	1.65e-2
83							370.0	1.85e-2	1.51e-2
84							375.0	1.38e-2	1.09e-2

	1-Run #	2-Part #	3-LET	4-Rot	5-Tilt	6-XS Data	7-fit Rot	8-hi XS	9-nom XS
85							380.0	9.13e-3	6.77e-3
86							385.0	5.04e-3	3.25e-3
87							390.0	1.98e-3	8.08e-4
88							395.0	1.79e-4	0.000
89							400.0	0.000	0.000
90							405.0	0.000	0.000
91							410.0	0.000	0.000
92							415.0	0.000	0.000
93							420.0	0.000	0.000
94							425.0	0.000	0.000
95							430.0	0.000	0.000
96							435.0	0.000	0.000
97							440.0	0.000	0.000
98							445.0	0.000	0.000
99							450.0	0.000	0.000

We next plot the fit, i.e., the model prediction. The first step is to manually enter the items in Column 7 of Fig. 11, which are the rotation angles that the fit is plotted against. A SigmaPlot Transform is used to construct model predictions for each rotation angle listed in this column. A hard copy of the programming is listed in Appendix E. The user can type this in at the keyboard. Before running the Transform, verify that the trig button is set for radians (needed for inverse trig functions called by the program). The code recognizes that angles in the worksheet are in degrees and makes the necessary conversions within the program. The numerical values in the “Assign parameters” box were taken from Table 2 and are unique to the example considered. The contents of the “Assign variables” box is unique to the type of plot desired. The example in Appendix E is set up for a rotation sweep at an LET of 3.4 and a 75° tilt angle, using the fitting parameters in Table 2, and the model predictions were written in Column 9 of Fig. 11. The “Assign parameters” box, “Assign variables” box, and “Assign output column” box require editing for different jobs (semicolons can be used for comments or for deactivating a line, which simplifies the editing), but the code between these boxes is the same for all jobs. The model prediction constructed by the example in Appendix E is plotted as a curve by plotting Column 9 versus Column 7. The result is shown as the dashed curve (identified as “nominal”) in Fig. 12. Similar steps are used to plot the other sweeps and the results are the dashed curves in Figs. 13 through 19.

For each sweep shown in Figs. 12 through 19, the scales were selected to show the relative importance of various points for SEU rate calculations. For the rotation sweeps, there is no flux weighting that favors one point over another, so what is important is the area under the curve when using a linear scale for the cross section, hence a linear scale was used. For the tilt sweeps, there is a mild weighting by $\sin\theta$ that favors one point over another (having to do with relating solid angle increments to θ increments), but no flux weighting, so linear scales were also used in these plots. For the LET sweep there is a flux weighting that gives more weight to the smaller LET, so a log scale was used to provide resolution at the smaller LETs.

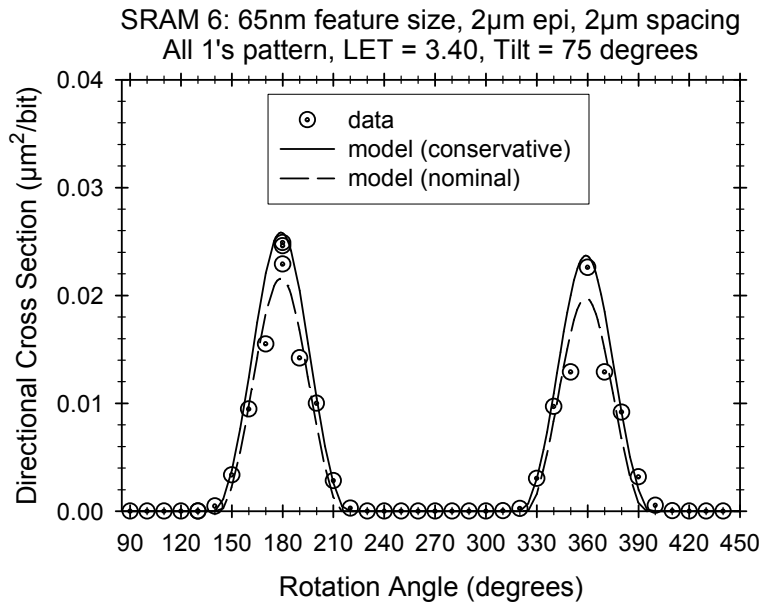


Fig. 12. The model is compared to data for a rotation sweep of an early version of the SRAM6 in all-1's.

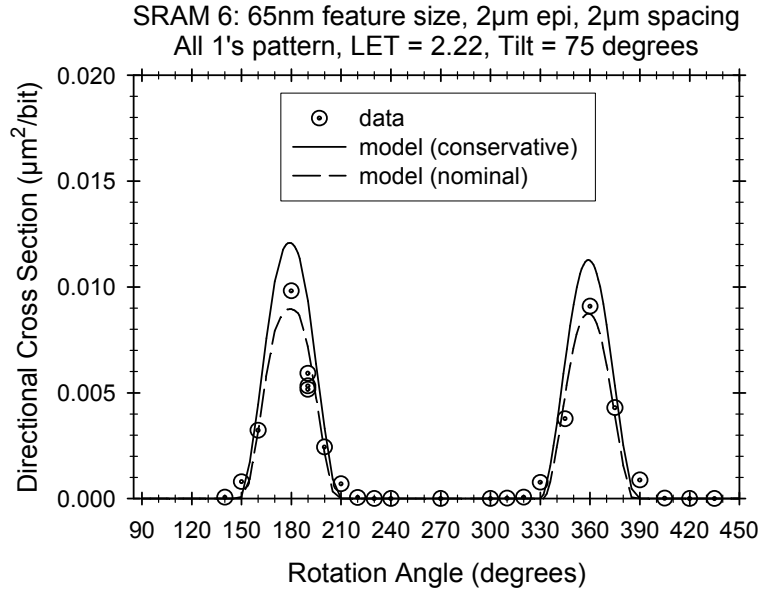


Fig. 13. The model is compared to data for a second rotation sweep of an early version of the SRAM6 in all-1's.

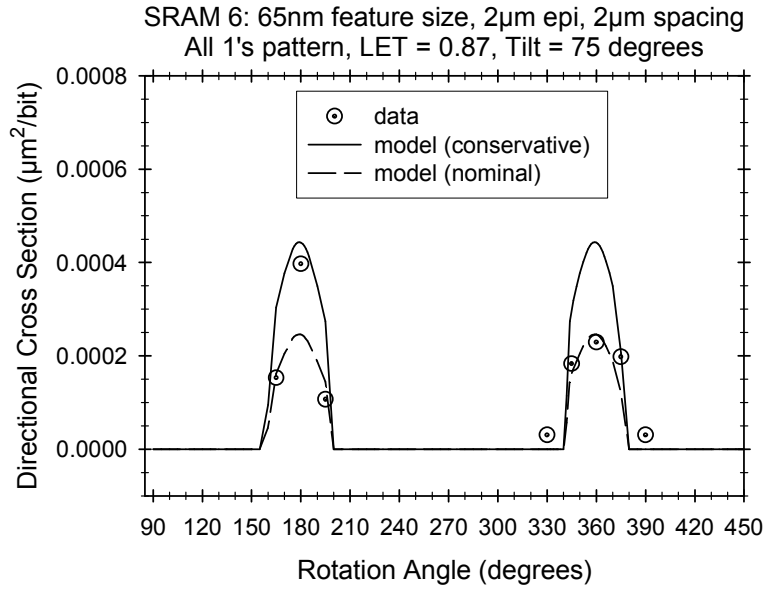


Fig. 14. The model is compared to data for a third rotation sweep of an early version of the SRAM6 in all-1's.

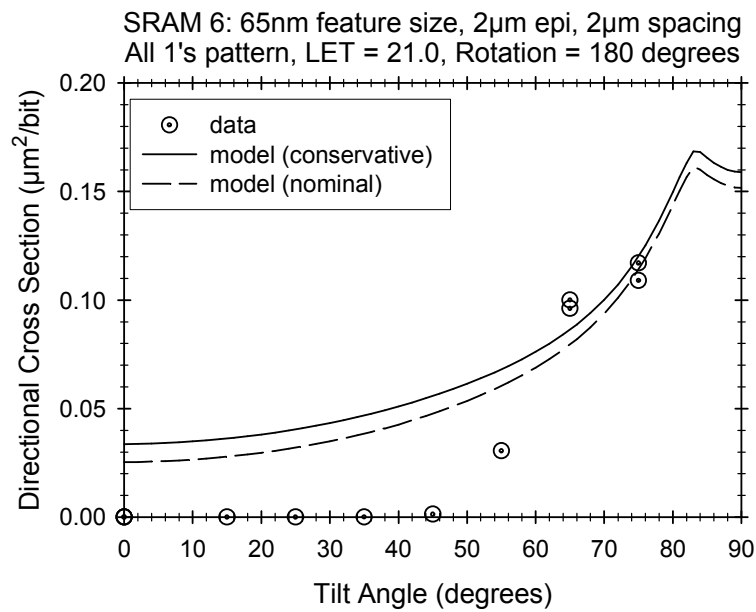


Fig. 15. The model is compared to data for a tilt sweep of an early version of the SRAM6 in all-1's.

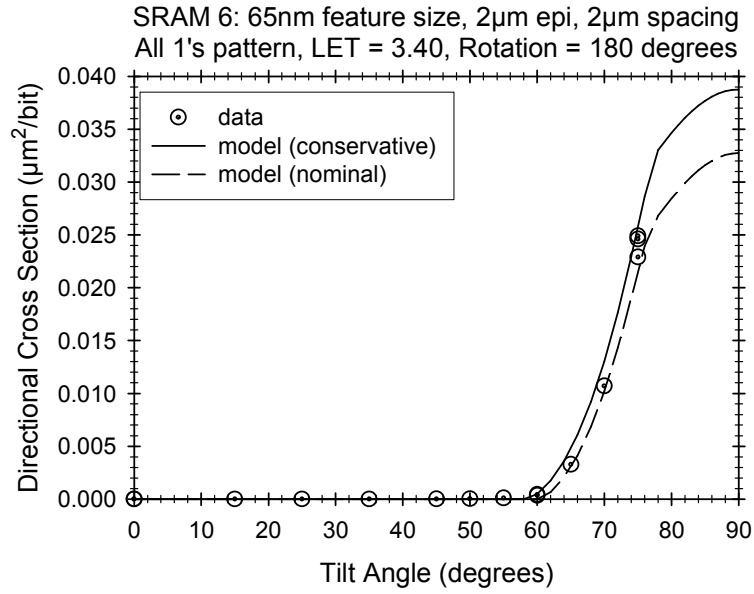


Fig. 16. The model is compared to data for a second tilt sweep of an early version of the SRAM6 in all-1's.

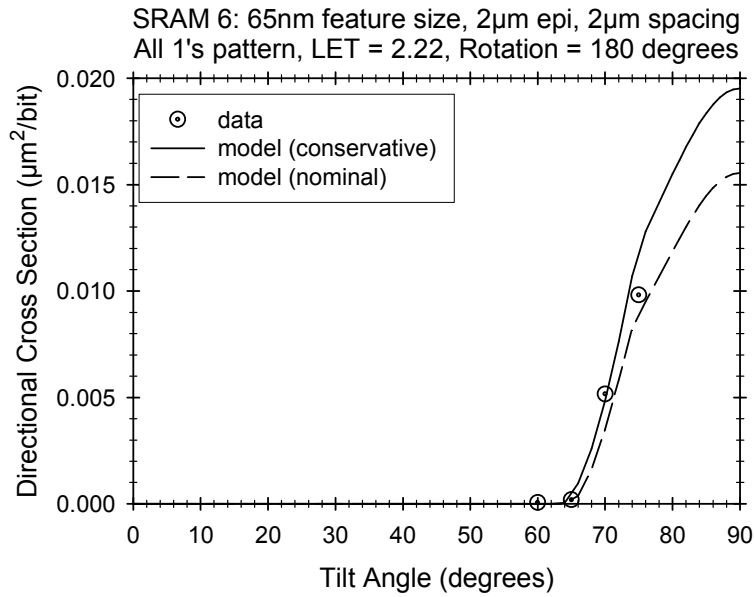


Fig. 17. The model is compared to data for a third tilt sweep of an early version of the SRAM6 in all-1's.

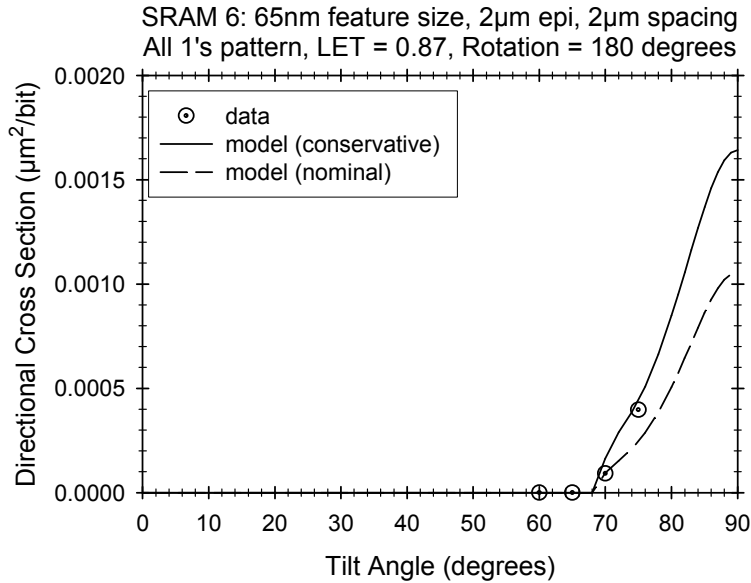


Fig. 18. The model is compared to data for a fourth tilt sweep of an early version of the SRAM6 in all-1's.

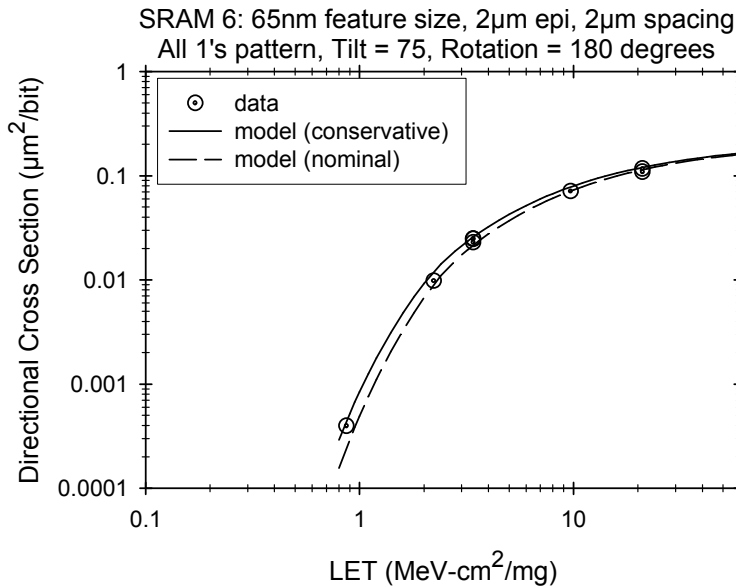


Fig. 19. The model is compared to data for an LET sweep of an early version of the SRAM6 in all-1's.

The model predictions plotted so far are identified as “nominal” in Figs. 12 through 19, because they use the fitting parameters (in Table 2) that produce the best fit as defined by the error measure used by the Regression Wizard. The fit appears very conservative (compared to the data) in Fig. 15, but this is at an LET of 21 and it will be seen later that such large LETs do not have an important influence on the estimated SEU rate (hence the weighting was selected to produce better agreement at the smaller LETs, at the expense of less agreement at the largest LETs). In the other sweeps, the nominal fit goes slightly

under most of the non-zero data points. This motivates including another fit that contains some conservatism. Such a fit also provides a sensitivity test, by showing how sensitive the estimated SEU rate is to the choice of fitting parameters. Conservatism can be included by increasing the single-node cross section for the node having the smaller cross section. According to Table 2, this is Node 2 (note that the nodes are interchangeable in the theory, so the one that is identified as the softer node is an artifact of the path that the Regression Wizard followed, which in turn is controlled by the initial guess for the fitting parameters). However, the nominal fit is already conservative at the largest LETs, so we look for a way to include conservatism at the smaller LETs without increasing the conservatism at the larger LETs. This can be done by leaving the saturation cross section for Node 2 (S_{02} in Table 2) as is, but decreasing L_{02} in Table 2. This produces the conservative parameters in Table 3. Repeating the steps that produced the nominal curves in Figs. 12 through 19, but with parameters now taken from Table 3, produces the conservative curves in the figures. Note that the two sets of curves envelope most of the data points.

Table 3. Conservative parameters for an early version of SRAM6 in all 1's

A = 0.2234	B = 0.6953
L01 = 0	L02 = 39
S01 = 2.914	S02 = 1.215
phi_off = 1.685e-2	h = 6.583e-3
P = 0.7075	T = 2

Step 4: Calculate the Upset Rate

With the fitting parameters extracted and verified to give an adequate representation of the data, they can then be used to estimate the dual-node upset rate in a given heavy-ion environment. The first step calculates the directional-average cross section by numerically evaluating the integrals in (5). This double integral is more conveniently done in FORTRAN77. A hard copy of the source code is listed in Appendix F. The user can type this in at the keyboard and then compile it with a FORTRAN77 compiler, or the user can rewrite it in another language. Inputs are entered at prompts and are self explanatory. The inputs do not ask for the offset rotation angle because this is not needed to perform the integration. The output is in the file “XSAVG.TXT,” which contains a table of directional-average cross section versus LET. Note that a change is made in the units. The cross section units in the output file is cm^2/bit .

Although not necessary for rate calculations, it may be interesting to see a plot of the directional-average cross section. Plots can be constructed by importing the contents of XSAVG.TXT to a plotter routine. The dashed curve in Fig. 20 was produced by entering the Table 2 parameters together with $T = 2\mu\text{m}$ when running the FORTRAN code, and the solid curve was produced by the Table 3 parameters.

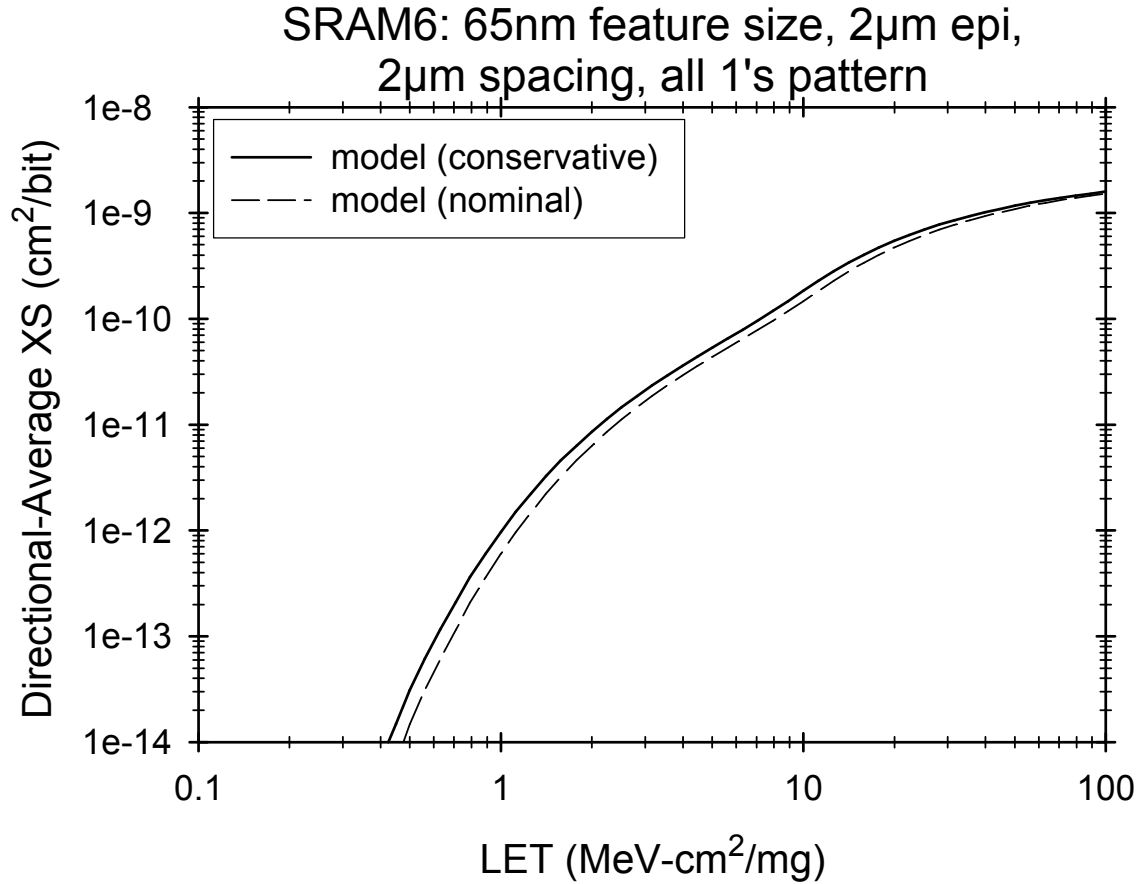


Fig. 20. The directional cross section is calculated by the model for each direction, and angular integrations convert this into a directional-average cross section. This cross section can be combined with the LET spectrum of any heavy-ion environment to obtain an estimate of the SEU rate in that environment. The plots shown here apply to an early version of the SRAM6 in all-1's.

Rate calculations are performed by importing the contents of XSAVG.TXT to a SigmaPlot worksheet. An example is shown in the first two columns of Fig. 21. The nominal parameters from Table 2 together with $T = 2\mu\text{m}$ were used for this example. The LET units in Column 1 are MeV-cm²/mg, and the directional-average cross section units in Column 2 are cm²/bit. The objective is to numerically evaluate the LET integral in (3). Note that the flux in (3) is a differential flux, but the integral can also be expressed as a sum of cross sections multiplied by increments of the integral flux. The integral LET flux was obtained from CREME96 and represents galactic cosmic rays in interplanetary space during solar minimum conditions, and behind 100mils of spherical aluminum shielding (all heavy ions are included but protons are not). Converting the directional flux in units of 1/m²-sec-ster into an omnidirectional flux in the units of 1/cm²-day (by multiplying by 108.6), and converting LET units in the CREME96 output (converting g to mg), and then interpolating the flux table to obtain the flux at the LETs in Column 1 of Fig. 21, produces the entries in Column 3 of Fig. 21. The incremental integral flux can be calculated using the SigmaPlot Quick Transform with the line `col(4)=-diff(col(3))` (the minus sign is intentional). This produces the entries in Column 4

in Fig. 21, except for the entry in Row 1 that is manually changed to zero. Then Column 2 is multiplied by Column 4 and the result is placed in Column 5. Finally, the increments are summed using the SigmaPlot Quick Transform with the line $col(6) = sum(col(5))$, which places a running total in Column 6. The estimated upset rate is the bottom row entry, or 1.49×10^{-9} /bit-day. Note that the running total in Column 6 also shows which LET values make the largest contribution to the final total. In this example, about half the total was produced by LET values up to 3.98, and about 95% of the total was obtained when the LET reaches a value of 19.95. This verifies the earlier claims that the smaller LET values are the most important. Repeating these calculations, but with parameters taken from Table 3, produces a conservative upset rate estimate of 2×10^{-9} /bit-day, which is fairly close to the nominal estimate. Recall that this estimate is for the all-1's pattern, and the 1-state is worst case, so the estimate is conservative for any other bit pattern.

Fig. 21. Upset Rate Calculation for an early version of the SRAM6 in all-1's.

	1-LET	2-XSAVG	3-flux	4-delta flux	5-XS*delta f	6-SUM
1	0.10	9.90e-23	2.223e+3	0.0000	0.0000	0.0000
2	0.11	8.07e-22	1.915e+3	3.079e+2	2.484e-19	2.48e-19
3	0.13	5.63e-21	1.495e+3	4.197e+2	2.363e-18	2.61e-18
4	0.14	3.40e-20	1.384e+3	1.117e+2	3.797e-18	6.41e-18
5	0.16	1.80e-19	1.232e+3	1.516e+2	2.730e-17	3.37e-17
6	0.18	8.43e-19	1.078e+3	1.537e+2	1.296e-16	1.63e-16
7	0.20	3.53e-18	9.826e+2	9.586e+1	3.384e-16	5.02e-16
8	0.22	1.34e-17	9.066e+2	7.601e+1	1.019e-15	1.52e-15
9	0.25	4.59e-17	7.800e+2	1.266e+2	5.810e-15	7.33e-15
10	0.28	1.44e-16	6.852e+2	9.480e+1	1.365e-14	2.10e-14
11	0.32	4.18e-16	5.986e+2	8.657e+1	3.619e-14	5.72e-14
12	0.35	1.13e-15	5.118e+2	8.686e+1	9.815e-14	1.55e-13
13	0.40	2.82e-15	4.351e+2	7.672e+1	2.163e-13	3.72e-13
14	0.45	6.63e-15	3.807e+2	5.436e+1	3.604e-13	7.32e-13
15	0.50	1.47e-14	3.426e+2	3.808e+1	5.597e-13	1.29e-12
16	0.56	3.07e-14	3.086e+2	3.405e+1	1.045e-12	2.34e-12
17	0.63	6.09e-14	2.780e+2	3.059e+1	1.863e-12	4.20e-12
18	0.71	1.15e-13	2.465e+2	3.148e+1	3.620e-12	7.82e-12
19	0.79	2.08e-13	2.245e+2	2.204e+1	4.584e-12	1.24e-11
20	0.89	3.60e-13	2.008e+2	2.363e+1	8.506e-12	2.09e-11
21	1.00	5.98e-13	1.797e+2	2.115e+1	1.265e-11	3.36e-11
22	1.12	9.59e-13	1.583e+2	2.140e+1	2.052e-11	5.41e-11
23	1.26	1.48e-12	1.023e+2	5.600e+1	8.288e-11	1.37e-10
24	1.41	2.22e-12	7.484e+1	2.746e+1	6.096e-11	1.98e-10
25	1.58	3.23e-12	5.709e+1	1.775e+1	5.733e-11	2.55e-10
26	1.78	4.58e-12	4.410e+1	1.299e+1	5.949e-11	3.15e-10
27	2.00	6.31e-12	3.438e+1	9.723e+0	6.135e-11	3.76e-10
28	2.24	8.51e-12	2.701e+1	7.376e+0	6.277e-11	4.39e-10
29	2.51	1.12e-11	2.123e+1	5.771e+0	6.464e-11	5.03e-10
30	2.82	1.46e-11	1.655e+1	4.679e+0	6.832e-11	5.72e-10
31	3.16	1.86e-11	1.293e+1	3.627e+0	6.745e-11	6.39e-10
32	3.55	2.34e-11	1.005e+1	2.882e+0	6.743e-11	7.07e-10

	1-LET	2-XSAVG	3-flux	4-delta flux	5-XS*delta f	6-SUM
33	3.98	2.91e-11	7.808e+0	2.239e+0	6.515e-11	7.72e-10
34	4.47	3.59e-11	6.024e+0	1.784e+0	6.405e-11	8.36e-10
35	5.01	4.39e-11	4.644e+0	1.380e+0	6.056e-11	8.96e-10
36	5.62	5.35e-11	3.563e+0	1.081e+0	5.784e-11	9.54e-10
37	6.31	6.49e-11	2.717e+0	8.459e-1	5.490e-11	1.01e-9
38	7.08	7.88e-11	2.070e+0	6.475e-1	5.102e-11	1.06e-9
39	7.94	9.60e-11	1.578e+0	4.915e-1	4.719e-11	1.11e-9
40	8.91	1.18e-10	1.212e+0	3.660e-1	4.319e-11	1.15e-9
41	10.00	1.47e-10	9.199e-1	2.924e-1	4.298e-11	1.19e-9
42	11.22	1.83e-10	6.940e-1	2.258e-1	4.133e-11	1.23e-9
43	12.59	2.28e-10	5.110e-1	1.831e-1	4.174e-11	1.28e-9
44	14.13	2.80e-10	3.710e-1	1.399e-1	3.918e-11	1.32e-9
45	15.85	3.38e-10	2.708e-1	1.003e-1	3.389e-11	1.35e-9
46	17.78	4.02e-10	1.933e-1	7.745e-2	3.114e-11	1.38e-9
47	19.95	4.70e-10	1.318e-1	6.150e-2	2.891e-11	1.41e-9
48	22.39	5.42e-10	8.202e-2	4.977e-2	2.698e-11	1.44e-9
49	25.12	6.17e-10	4.223e-2	3.979e-2	2.455e-11	1.46e-9
50	28.18	6.95e-10	3.630e-3	3.860e-2	2.683e-11	1.49e-9
51	31.62	7.74e-10	1.251e-4	3.505e-3	2.713e-12	1.49e-9
52	35.48	8.53e-10	6.470e-5	6.036e-5	5.149e-14	1.49e-9
53	39.81	9.33e-10	4.302e-5	2.168e-5	2.022e-14	1.49e-9
54	44.67	1.01e-9	2.907e-5	1.396e-5	1.410e-14	1.49e-9
55	50.12	1.09e-9	1.983e-5	9.240e-6	1.007e-14	1.49e-9
56	56.23	1.17e-9	1.274e-5	7.085e-6	8.289e-15	1.49e-9
57	63.10	1.24e-9	7.404e-6	5.340e-6	6.621e-15	1.49e-9
58	70.79	1.32e-9	4.129e-6	3.275e-6	4.323e-15	1.49e-9
59	79.43	1.39e-9	1.853e-6	2.276e-6	3.164e-15	1.49e-9
60	89.13	1.46e-9	2.856e-7	1.567e-6	2.288e-15	1.49e-9
61	100.00	1.52e-9	1.359e-8	2.720e-7	4.134e-16	1.49e-9

IX. A SECOND EXAMPLE

The example device discussed here is a later version of the SRAM6. This is a test chip designed so that ions at large incident angles (close to 90 degrees) will be able to reach the active regions without having to penetrate a large path length of device material, hence large-angle tests can be performed. The device was tested in both the all-1's bit pattern and all-0's bit pattern (it will be seen later that the all-1's pattern is more susceptible to upsets). Raw test data for this later version, provided by Xilinx, were obtained from tests performed on 8/24/08, 9/25/08, and 2/12/09. However, a great deal of processing was needed to present these data sets in a readable and organized format. Gregory R. Allen (JPL) performed this processing and presented the data in column format in [11]. The all-1's and all-0's are discussed separately below.

A. The All-1's Pattern

The data from [11] for the all-1's are reproduced here in Fig. 22. Blocks of data are shown side-by-side in the figure, but one block is above another in the spreadsheet, so all LET entries (in MeV-cm²/mg) are in Column 1 of the spreadsheet, all tilt angle entries (degrees) are in Column 2, all rotation angle entries (degrees) are in Column 3, and all cross section entries (μm²/bit) are in Column 4. This is a very large data set (976 data points) and many sweeps (tilt, rotation, or LET) are needed to represent all points in a graphical format. The set of sweeps was selected so that every data point is included in at least one sweep, with the number of sweeps being the smallest number that can include all points. This produces the set of rotation sweeps, tilt sweeps, and LET sweeps shown as the points in Figs. 23 to 25 (the curves are discussed later).

Fig. 22. Measured Data for a later version of SRAM6 in all-1's.

LET	Tilt	Rot	XS	LET	Tilt	Rot	XS	LET	Tilt	Rot	XS
25.00	85.0	-90.0	0.000	25.00	85.0	40.0	2.14e-4	25.00	85.0	195.0	1.27e-1
25.00	85.0	-65.0	9.75e-5	25.00	85.0	40.0	3.36e-4	25.00	85.0	200.0	4.09e-2
25.00	85.0	-60.0	2.12e-3	25.00	85.0	45.0	1.05e-4	25.00	85.0	200.0	7.32e-2
25.00	85.0	-60.0	3.67e-3	25.00	85.0	50.0	3.05e-5	25.00	85.0	205.0	2.95e-2
25.00	85.0	-50.0	2.01e-2	25.00	85.0	60.0	6.10e-6	25.00	85.0	210.0	7.04e-3
25.00	85.0	-45.0	1.27e-2	25.00	85.0	60.0	5.98e-6	25.00	85.0	210.0	4.69e-3
25.00	85.0	-40.0	3.92e-2	25.00	85.0	65.0	3.65e-5	25.00	85.0	215.0	2.69e-3
25.00	85.0	-40.0	4.41e-2	25.00	85.0	90.0	1.74e-5	25.00	85.0	215.0	7.35e-4
25.00	85.0	-35.0	5.38e-2	25.00	85.0	90.0	5.23e-5	25.00	85.0	220.0	5.03e-4
25.00	85.0	-35.0	5.14e-2	25.00	85.0	115.0	7.31e-5	25.00	85.0	220.0	1.40e-4
25.00	85.0	-30.0	7.53e-2	25.00	85.0	120.0	1.34e-4	25.00	85.0	225.0	1.63e-4
25.00	85.0	-30.0	6.82e-2	25.00	85.0	120.0	1.80e-4	25.00	85.0	230.0	6.10e-6
25.00	85.0	-25.0	8.38e-2	25.00	85.0	130.0	1.21e-2	25.00	85.0	240.0	5.98e-6
25.00	85.0	-20.0	6.92e-2	25.00	85.0	135.0	9.91e-3	25.00	85.0	240.0	1.83e-5
25.00	85.0	-20.0	1.33e-1	25.00	85.0	140.0	2.84e-2	25.00	85.0	245.0	0.000
25.00	85.0	-15.0	1.55e-1	25.00	85.0	140.0	2.15e-2	25.00	85.0	270.0	6.98e-5
25.00	85.0	-15.0	1.47e-1	25.00	85.0	145.0	3.65e-2	25.00	83.0	-90.0	5.55e-6
25.00	85.0	-10.0	0.000	25.00	85.0	145.0	3.11e-2	25.00	83.0	-75.0	1.26e-5
25.00	85.0	-10.0	1.45e-1	25.00	85.0	150.0	5.31e-2	25.00	83.0	-75.0	2.52e-5
25.00	85.0	-10.0	1.31e-1	25.00	85.0	150.0	5.41e-2	25.00	83.0	-60.0	4.06e-4
25.00	85.0	-5.0	1.20e-1	25.00	85.0	155.0	6.71e-2	25.00	83.0	-60.0	3.72e-4

LET	Tilt	Rot	XS
25.00	85.0	-5.0	1.05e-1
25.00	85.0	0.0	5.58e-2
25.00	85.0	0.0	5.31e-2
25.00	85.0	0.0	9.32e-2
25.00	85.0	0.0	8.43e-2
25.00	85.0	5.0	8.54e-2
25.00	85.0	5.0	7.28e-2
25.00	85.0	10.0	0.000
25.00	85.0	10.0	9.26e-2
25.00	85.0	10.0	8.05e-2
25.00	85.0	15.0	1.04e-1
25.00	85.0	15.0	8.44e-2
25.00	85.0	20.0	4.89e-2
25.00	85.0	20.0	1.71e-2
25.00	85.0	25.0	1.58e-2
25.00	85.0	30.0	6.36e-3
25.00	85.0	30.0	5.15e-3
25.00	85.0	35.0	1.85e-3
25.00	85.0	35.0	1.46e-3
25.00	83.0	75.0	5.04e-6
25.00	83.0	90.0	0.000
25.00	83.0	90.0	5.55e-6
25.00	83.0	105.0	0.000
25.00	83.0	105.0	1.26e-5
25.00	83.0	120.0	2.44e-5
25.00	83.0	120.0	1.33e-5
25.00	83.0	135.0	1.03e-2
25.00	83.0	135.0	7.92e-3
25.00	83.0	150.0	3.94e-2
25.00	83.0	150.0	3.78e-2
25.00	83.0	165.0	1.02e-1
25.00	83.0	165.0	9.90e-2
25.00	83.0	175.0	3.95e-2
25.00	83.0	180.0	5.27e-2
25.00	83.0	180.0	5.74e-2
25.00	83.0	185.0	7.73e-2
25.00	83.0	195.0	1.48e-1
25.00	83.0	195.0	1.35e-1
25.00	83.0	210.0	6.67e-3
25.00	83.0	210.0	3.60e-3
25.00	83.0	225.0	3.76e-5
25.00	83.0	225.0	4.22e-5
25.00	83.0	240.0	0.000
25.00	83.0	240.0	2.00e-5
25.00	83.0	255.0	5.04e-6
25.00	83.0	255.0	6.31e-6
25.00	83.0	270.0	1.66e-5
25.00	82.5	-25.0	7.06e-3
25.00	82.5	0.0	5.61e-2
25.00	82.5	0.0	5.20e-2
25.00	82.5	0.0	6.65e-2
25.00	82.5	0.0	6.90e-2
25.00	82.5	25.0	4.94e-2

LET	Tilt	Rot	XS
25.00	85.0	160.0	9.16e-2
25.00	85.0	160.0	4.93e-2
25.00	85.0	165.0	9.30e-2
25.00	85.0	165.0	8.34e-2
25.00	85.0	170.0	7.26e-2
25.00	85.0	170.0	5.47e-2
25.00	85.0	170.0	0.000
25.00	85.0	175.0	7.40e-2
25.00	85.0	175.0	6.93e-2
25.00	85.0	180.0	8.02e-2
25.00	85.0	180.0	7.47e-2
25.00	85.0	180.0	5.57e-2
25.00	85.0	180.0	5.29e-2
25.00	85.0	185.0	1.04e-1
25.00	85.0	185.0	9.33e-2
25.00	85.0	190.0	1.40e-1
25.00	85.0	190.0	1.27e-1
25.00	85.0	190.0	0.000
25.00	85.0	195.0	1.37e-1
25.00	80.0	-90.0	1.39e-5
25.00	80.0	-75.0	1.46e-4
25.00	80.0	-75.0	1.50e-4
25.00	80.0	-70.0	0.000
25.00	80.0	-70.0	0.000
25.00	80.0	-60.0	1.03e-3
25.00	80.0	-60.0	9.64e-4
25.00	80.0	-55.0	0.000
25.00	80.0	-55.0	0.000
25.00	80.0	-50.0	1.49e-2
25.00	80.0	-45.0	1.20e-2
25.00	80.0	-45.0	1.28e-2
25.00	80.0	-40.0	3.24e-2
25.00	80.0	-35.0	4.42e-2
25.00	80.0	-30.0	4.79e-2
25.00	80.0	-30.0	4.14e-2
25.00	80.0	-30.0	5.66e-2
25.00	80.0	-30.0	5.82e-2
25.00	80.0	-25.0	6.11e-2
25.00	80.0	-20.0	8.49e-2
25.00	80.0	-20.0	7.65e-2
25.00	80.0	-15.0	1.21e-1
25.00	80.0	-15.0	1.39e-1
25.00	80.0	-15.0	1.35e-1
25.00	80.0	-10.0	0.000
25.00	80.0	-10.0	1.17e-1
25.00	80.0	-10.0	1.43e-1
25.00	80.0	-5.0	9.13e-2
25.00	80.0	-5.0	1.28e-1
25.00	80.0	0.0	8.96e-2
25.00	80.0	0.0	8.46e-2
25.00	80.0	0.0	9.44e-2
25.00	80.0	0.0	9.64e-2
25.00	80.0	5.0	1.01e-1

LET	Tilt	Rot	XS
25.00	83.0	-45.0	1.07e-2
25.00	83.0	-45.0	1.30e-2
25.00	83.0	-30.0	6.92e-2
25.00	83.0	-30.0	6.66e-2
25.00	83.0	-15.0	1.57e-1
25.00	83.0	-15.0	1.57e-1
25.00	83.0	-5.0	7.10e-2
25.00	83.0	0.0	7.43e-2
25.00	83.0	0.0	7.00e-2
25.00	83.0	5.0	5.57e-2
25.00	83.0	15.0	8.61e-2
25.00	83.0	15.0	8.46e-2
25.00	83.0	30.0	6.71e-4
25.00	83.0	30.0	8.64e-4
25.00	83.0	45.0	7.03e-5
25.00	83.0	45.0	2.82e-5
25.00	83.0	60.0	6.66e-6
25.00	83.0	60.0	0.000
25.00	83.0	75.0	1.26e-5
25.00	80.0	15.0	7.67e-2
25.00	80.0	20.0	1.00e-2
25.00	80.0	20.0	8.16e-3
25.00	80.0	25.0	7.76e-4
25.00	80.0	30.0	2.38e-4
25.00	80.0	30.0	2.86e-4
25.00	80.0	30.0	2.76e-4
25.00	80.0	30.0	4.70e-4
25.00	80.0	35.0	2.03e-4
25.00	80.0	40.0	2.49e-4
25.00	80.0	45.0	2.44e-5
25.00	80.0	45.0	8.54e-5
25.00	80.0	50.0	6.31e-5
25.00	80.0	55.0	3.16e-3
25.00	80.0	55.0	2.50e-3
25.00	80.0	60.0	0.000
25.00	80.0	60.0	1.40e-5
25.00	80.0	70.0	3.05e-5
25.00	80.0	70.0	0.000
25.00	80.0	75.0	6.10e-6
25.00	80.0	75.0	5.76e-6
25.00	80.0	90.0	0.000
25.00	80.0	90.0	8.36e-6
25.00	80.0	105.0	4.03e-5
25.00	80.0	105.0	1.22e-5
25.00	80.0	110.0	0.000
25.00	80.0	110.0	0.000
25.00	80.0	120.0	2.10e-5
25.00	80.0	120.0	6.10e-6
25.00	80.0	125.0	0.000
25.00	80.0	125.0	0.000
25.00	80.0	130.0	2.74e-4
25.00	80.0	135.0	6.35e-4
25.00	80.0	135.0	4.39e-4

LET	Tilt	Rot	XS
25.00	82.5	155.0	3.53e-3
25.00	82.5	180.0	5.00e-2
25.00	82.5	180.0	4.94e-2
25.00	82.5	180.0	3.22e-2
25.00	82.5	180.0	2.76e-2
25.00	82.5	205.0	4.85e-2
25.00	80.0	155.0	4.16e-2
25.00	80.0	160.0	6.12e-2
25.00	80.0	160.0	5.94e-2
25.00	80.0	165.0	8.60e-2
25.00	80.0	165.0	8.19e-2
25.00	80.0	165.0	7.01e-2
25.00	80.0	170.0	9.68e-2
25.00	80.0	170.0	7.20e-2
25.00	80.0	170.0	0.000
25.00	80.0	175.0	6.78e-2
25.00	80.0	175.0	4.94e-2
25.00	80.0	180.0	5.77e-2
25.00	80.0	180.0	5.71e-2
25.00	80.0	180.0	5.14e-2
25.00	80.0	180.0	4.72e-2
25.00	80.0	185.0	9.05e-2
25.00	80.0	185.0	1.34e-1
25.00	80.0	190.0	1.39e-1
25.00	80.0	190.0	1.65e-1
25.00	80.0	190.0	0.000
25.00	80.0	195.0	1.30e-1
25.00	80.0	195.0	1.09e-1
25.00	80.0	195.0	9.57e-2
25.00	80.0	200.0	7.22e-2
25.00	80.0	200.0	6.29e-2
25.00	80.0	205.0	3.72e-2
25.00	80.0	210.0	1.12e-2
25.00	80.0	210.0	7.70e-3
25.00	80.0	210.0	9.04e-3
25.00	80.0	210.0	6.24e-3
25.00	80.0	215.0	1.48e-4
25.00	80.0	220.0	2.35e-5
25.00	80.0	225.0	0.000
25.00	80.0	225.0	1.22e-5
25.00	80.0	230.0	4.21e-6
25.00	80.0	235.0	2.99e-3
25.00	80.0	235.0	3.77e-3
25.00	80.0	240.0	0.000
25.00	80.0	240.0	6.10e-6
25.00	80.0	250.0	0.000
25.00	75.0	135.0	2.03e-4
25.00	75.0	140.0	2.98e-4
25.00	75.0	145.0	4.86e-4
25.00	75.0	150.0	1.00e-3
25.00	75.0	150.0	2.26e-3
25.00	75.0	150.0	1.46e-3
25.00	75.0	150.0	4.88e-4

LET	Tilt	Rot	XS
25.00	80.0	5.0	7.56e-2
25.00	80.0	10.0	0.000
25.00	80.0	10.0	1.02e-1
25.00	80.0	10.0	8.54e-2
25.00	80.0	15.0	5.48e-2
25.00	80.0	15.0	5.97e-2
25.00	80.0	250.0	0.000
25.00	80.0	255.0	5.76e-6
25.00	80.0	255.0	6.10e-6
25.00	80.0	270.0	1.39e-5
25.00	77.5	-25.0	5.55e-4
25.00	77.5	0.0	1.35e-1
25.00	77.5	0.0	1.26e-1
25.00	77.5	25.0	3.33e-2
25.00	77.5	155.0	1.66e-3
25.00	77.5	180.0	1.39e-1
25.00	77.5	180.0	1.16e-1
25.00	77.5	205.0	2.89e-2
25.00	75.0	-90.0	3.04e-5
25.00	75.0	-90.0	3.05e-5
25.00	75.0	-75.0	4.43e-4
25.00	75.0	-60.0	8.54e-4
25.00	75.0	-60.0	7.32e-4
25.00	75.0	-60.0	2.69e-3
25.00	75.0	-60.0	4.65e-3
25.00	75.0	-50.0	1.59e-2
25.00	75.0	-45.0	2.14e-2
25.00	75.0	-40.0	3.30e-2
25.00	75.0	-35.0	2.14e-2
25.00	75.0	-30.0	3.52e-2
25.00	75.0	-30.0	2.75e-2
25.00	75.0	-30.0	4.51e-2
25.00	75.0	-30.0	4.29e-2
25.00	75.0	-25.0	4.16e-2
25.00	75.0	-25.0	4.23e-2
25.00	75.0	-20.0	6.61e-2
25.00	75.0	-20.0	6.37e-2
25.00	75.0	-15.0	9.94e-2
25.00	75.0	-15.0	9.21e-2
25.00	75.0	-12.5	6.71e-2
25.00	75.0	-10.0	1.55e-1
25.00	75.0	-10.0	1.24e-1
25.00	75.0	-7.5	8.15e-2
25.00	75.0	-5.0	1.31e-1
25.00	75.0	-5.0	1.54e-1
25.00	75.0	-2.5	8.75e-2
25.00	75.0	210.0	1.11e-2
25.00	75.0	215.0	2.43e-4
25.00	75.0	220.0	2.29e-5
25.00	75.0	225.0	0.000
25.00	75.0	230.0	0.000
25.00	75.0	240.0	0.000
25.00	75.0	240.0	7.62e-6

LET	Tilt	Rot	XS
25.00	80.0	140.0	3.12e-3
25.00	80.0	145.0	6.33e-3
25.00	80.0	150.0	1.36e-2
25.00	80.0	150.0	1.20e-2
25.00	80.0	150.0	7.75e-3
25.00	80.0	150.0	9.19e-3
25.00	75.0	0.0	1.22e-1
25.00	75.0	0.0	1.15e-1
25.00	75.0	0.0	1.25e-1
25.00	75.0	0.0	1.17e-1
25.00	75.0	2.5	1.11e-1
25.00	75.0	5.0	1.22e-1
25.00	75.0	5.0	1.12e-1
25.00	75.0	7.5	6.81e-2
25.00	75.0	10.0	6.98e-2
25.00	75.0	10.0	8.96e-2
25.00	75.0	12.5	2.05e-2
25.00	75.0	15.0	1.31e-2
25.00	75.0	15.0	1.82e-2
25.00	75.0	20.0	1.71e-3
25.00	75.0	20.0	1.82e-3
25.00	75.0	25.0	2.94e-3
25.00	75.0	25.0	5.18e-4
25.00	75.0	30.0	1.53e-4
25.00	75.0	30.0	9.16e-5
25.00	75.0	30.0	2.06e-4
25.00	75.0	30.0	3.09e-4
25.00	75.0	35.0	2.43e-4
25.00	75.0	40.0	6.88e-5
25.00	75.0	45.0	2.84e-4
25.00	75.0	50.0	8.52e-5
25.00	75.0	60.0	0.000
25.00	75.0	60.0	0.000
25.00	75.0	60.0	1.91e-5
25.00	75.0	60.0	0.000
25.00	75.0	75.0	1.22e-5
25.00	75.0	90.0	0.000
25.00	75.0	90.0	0.000
25.00	75.0	90.0	3.04e-5
25.00	75.0	90.0	0.000
25.00	75.0	105.0	0.000
25.00	75.0	120.0	4.57e-5
25.00	75.0	120.0	0.000
25.00	75.0	120.0	6.10e-5
25.00	75.0	120.0	0.000
25.00	75.0	130.0	4.26e-5
25.00	30.0	155.0	1.15e-5
25.00	30.0	180.0	0.000
25.00	30.0	180.0	1.22e-5
25.00	30.0	205.0	1.15e-5
25.00	0.0	-25.0	0.000
25.00	0.0	0.0	6.10e-6
25.00	0.0	0.0	1.22e-5

LET	Tilt	Rot	XS
25.00	75.0	155.0	1.77e-2
25.00	75.0	155.0	1.96e-2
25.00	75.0	160.0	4.78e-2
25.00	75.0	160.0	4.76e-2
25.00	75.0	165.0	6.46e-2
25.00	75.0	165.0	6.34e-2
25.00	75.0	167.5	5.44e-2
25.00	75.0	170.0	8.40e-2
25.00	75.0	170.0	9.52e-2
25.00	75.0	172.5	8.88e-2
25.00	75.0	175.0	1.21e-1
25.00	75.0	175.0	1.04e-1
25.00	75.0	177.5	1.19e-1
25.00	75.0	180.0	1.23e-1
25.00	75.0	180.0	1.16e-1
25.00	75.0	180.0	1.16e-1
25.00	75.0	180.0	1.11e-1
25.00	75.0	182.5	7.54e-2
25.00	75.0	185.0	1.31e-1
25.00	75.0	185.0	1.45e-1
25.00	75.0	187.5	6.08e-2
25.00	75.0	190.0	1.40e-1
25.00	75.0	190.0	1.07e-1
25.00	75.0	192.5	6.28e-2
25.00	75.0	195.0	9.75e-2
25.00	75.0	195.0	8.48e-2
25.00	75.0	200.0	6.95e-2
25.00	75.0	200.0	6.14e-2
25.00	75.0	205.0	3.62e-2
25.00	75.0	205.0	3.07e-2
25.00	75.0	210.0	1.62e-2
25.00	75.0	210.0	9.22e-3
25.00	75.0	210.0	1.04e-2
17.00	85.0	180.0	9.18e-2
17.00	85.0	180.0	8.18e-2
17.00	85.0	185.0	8.26e-2
17.00	85.0	190.0	7.53e-2
17.00	85.0	200.0	5.03e-2
17.00	85.0	210.0	6.10e-4
17.00	85.0	240.0	0.000
17.00	85.0	270.0	0.000
17.00	82.5	0.0	5.42e-2
17.00	82.5	0.0	5.44e-2
17.00	82.5	180.0	2.45e-2
17.00	82.5	180.0	2.07e-2
17.00	80.0	-40.0	1.10e-3
17.00	80.0	-30.0	2.36e-2
17.00	80.0	-25.0	5.24e-4
17.00	80.0	-20.0	5.10e-2
17.00	80.0	-10.0	8.51e-2
17.00	80.0	-5.0	8.05e-2
17.00	80.0	-5.0	1.13e-1
17.00	80.0	0.0	7.38e-2

LET	Tilt	Rot	XS
25.00	75.0	240.0	0.000
25.00	75.0	240.0	3.05e-5
25.00	75.0	255.0	4.07e-6
25.00	75.0	270.0	0.000
25.00	75.0	270.0	2.73e-4
25.00	70.0	-25.0	1.16e-4
25.00	70.0	0.0	2.18e-3
25.00	70.0	0.0	1.67e-3
25.00	70.0	25.0	6.29e-3
25.00	70.0	155.0	1.16e-4
25.00	70.0	180.0	3.66e-3
25.00	70.0	180.0	3.57e-3
25.00	70.0	205.0	5.94e-3
25.00	65.0	-25.0	0.000
25.00	65.0	0.0	1.10e-4
25.00	65.0	0.0	9.75e-5
25.00	65.0	25.0	1.15e-3
25.00	65.0	155.0	0.000
25.00	65.0	180.0	3.65e-5
25.00	65.0	180.0	4.87e-5
25.00	65.0	205.0	8.14e-4
25.00	60.0	-25.0	0.000
25.00	60.0	0.0	1.17e-2
25.00	60.0	0.0	1.09e-2
25.00	60.0	25.0	3.90e-4
25.00	60.0	155.0	0.000
25.00	60.0	180.0	5.59e-3
25.00	60.0	180.0	5.54e-3
25.00	60.0	205.0	2.41e-4
25.00	30.0	-25.0	0.000
25.00	30.0	0.0	0.000
25.00	30.0	0.0	1.22e-5
25.00	30.0	25.0	1.15e-5
17.00	80.0	180.0	1.85e-2
17.00	80.0	185.0	5.06e-2
17.00	80.0	185.0	7.65e-2
17.00	80.0	190.0	8.88e-2
17.00	80.0	200.0	3.30e-2
17.00	80.0	205.0	2.31e-2
17.00	80.0	210.0	1.12e-3
17.00	80.0	220.0	0.000
17.00	77.5	0.0	1.37e-1
17.00	77.5	0.0	1.40e-1
17.00	77.5	180.0	6.41e-2
17.00	77.5	180.0	5.31e-2
17.00	75.0	-90.0	0.000
17.00	75.0	-75.0	0.000
17.00	75.0	-60.0	1.22e-4
17.00	75.0	-45.0	7.93e-4
17.00	75.0	-35.0	9.73e-4
17.00	75.0	-25.0	1.03e-2
17.00	75.0	-20.0	1.74e-2
17.00	75.0	-15.0	2.39e-2

LET	Tilt	Rot	XS
25.00	0.0	0.0	3.66e-5
25.00	0.0	0.0	0.000
25.00	0.0	25.0	1.22e-5
25.00	0.0	155.0	0.000
25.00	0.0	180.0	9.16e-6
25.00	0.0	180.0	0.000
25.00	0.0	180.0	0.000
25.00	0.0	180.0	1.22e-5
25.00	0.0	205.0	0.000
17.00	85.0	-90.0	0.000
17.00	85.0	-60.0	2.03e-4
17.00	85.0	-30.0	4.84e-2
17.00	85.0	-20.0	7.83e-2
17.00	85.0	-10.0	1.05e-1
17.00	85.0	-5.0	1.03e-1
17.00	85.0	0.0	7.83e-2
17.00	85.0	0.0	6.91e-2
17.00	85.0	0.0	1.30e-1
17.00	85.0	0.0	1.14e-1
17.00	85.0	5.0	1.08e-1
17.00	85.0	10.0	9.26e-2
17.00	85.0	20.0	1.83e-2
17.00	85.0	30.0	0.000
17.00	85.0	60.0	0.000
17.00	85.0	90.0	0.000
17.00	85.0	90.0	0.000
17.00	85.0	120.0	0.000
17.00	85.0	150.0	3.01e-2
17.00	85.0	160.0	6.33e-2
17.00	85.0	170.0	4.37e-2
17.00	85.0	175.0	5.27e-2
17.00	85.0	180.0	7.84e-2
17.00	85.0	180.0	8.09e-2
17.00	75.0	75.0	0.000
17.00	75.0	90.0	0.000
17.00	75.0	90.0	0.000
17.00	75.0	105.0	0.000
17.00	75.0	120.0	0.000
17.00	75.0	135.0	0.000
17.00	75.0	145.0	0.000
17.00	75.0	155.0	6.08e-4
17.00	75.0	160.0	5.73e-3
17.00	75.0	165.0	1.67e-2
17.00	75.0	170.0	2.18e-2
17.00	75.0	172.5	3.16e-2
17.00	75.0	175.0	3.22e-2
17.00	75.0	177.5	4.55e-2
17.00	75.0	177.5	2.24e-2
17.00	75.0	180.0	6.53e-2
17.00	75.0	180.0	5.78e-2
17.00	75.0	180.0	4.79e-2
17.00	75.0	180.0	4.59e-2
17.00	75.0	182.5	5.10e-2

LET	Tilt	Rot	XS
17.00	80.0	0.0	6.52e-2
17.00	80.0	0.0	1.05e-1
17.00	80.0	0.0	1.03e-1
17.00	80.0	5.0	8.25e-2
17.00	80.0	5.0	1.09e-1
17.00	80.0	10.0	7.40e-2
17.00	80.0	20.0	6.10e-4
17.00	80.0	25.0	2.25e-2
17.00	80.0	30.0	0.000
17.00	80.0	40.0	0.000
17.00	80.0	140.0	2.44e-4
17.00	80.0	150.0	7.11e-4
17.00	80.0	155.0	0.000
17.00	80.0	160.0	3.08e-2
17.00	80.0	170.0	4.69e-2
17.00	80.0	175.0	4.18e-2
17.00	80.0	175.0	2.76e-2
17.00	80.0	180.0	2.35e-2
17.00	80.0	180.0	1.56e-2
17.00	80.0	180.0	2.09e-2
17.00	45.0	0.0	1.83e-3
17.00	45.0	0.0	2.14e-3
17.00	45.0	180.0	0.000
17.00	45.0	180.0	0.000
17.00	0.0	0.0	3.46e-6
17.00	0.0	0.0	6.91e-6
17.00	0.0	180.0	0.000
17.00	0.0	180.0	0.000
7.50	87.0	-50.0	4.07e-6
7.50	87.0	-30.0	1.62e-3
7.50	87.0	-25.0	1.32e-2
7.50	87.0	-20.0	2.50e-2
7.50	87.0	-15.0	2.61e-2
7.50	87.0	-10.0	2.48e-2
7.50	87.0	-10.0	2.02e-2
7.50	87.0	-5.0	2.84e-2
7.50	87.0	0.0	5.91e-2
7.50	87.0	0.0	6.36e-2
7.50	87.0	5.0	4.37e-2
7.50	87.0	10.0	3.50e-2
7.50	87.0	10.0	3.24e-2
7.50	87.0	15.0	1.34e-2
7.50	87.0	20.0	8.72e-4
7.50	87.0	25.0	0.000
7.50	87.0	30.0	0.000
7.50	87.0	50.0	4.07e-6
7.50	87.0	130.0	3.26e-5
7.50	87.0	150.0	8.85e-4
7.50	87.0	155.0	5.35e-3
7.50	87.0	160.0	1.48e-2
7.50	87.0	165.0	1.76e-2
7.50	87.0	170.0	1.44e-2
7.50	87.0	170.0	1.11e-2

LET	Tilt	Rot	XS
17.00	75.0	-10.0	3.31e-2
17.00	75.0	-7.5	2.88e-2
17.00	75.0	-5.0	3.22e-2
17.00	75.0	-2.5	5.21e-2
17.00	75.0	-2.5	3.67e-2
17.00	75.0	0.0	6.34e-2
17.00	75.0	0.0	5.17e-2
17.00	75.0	0.0	6.37e-2
17.00	75.0	0.0	5.75e-2
17.00	75.0	2.5	3.70e-2
17.00	75.0	2.5	2.62e-2
17.00	75.0	5.0	2.98e-2
17.00	75.0	7.5	2.00e-2
17.00	75.0	10.0	1.16e-2
17.00	75.0	15.0	1.95e-3
17.00	75.0	20.0	3.65e-4
17.00	75.0	25.0	0.000
17.00	75.0	35.0	0.000
17.00	75.0	45.0	0.000
17.00	75.0	60.0	0.000
7.50	87.0	200.0	8.72e-4
7.50	87.0	205.0	5.76e-5
7.50	87.0	210.0	3.05e-5
7.50	87.0	230.0	4.07e-6
7.50	85.0	-90.0	0.000
7.50	85.0	-60.0	0.000
7.50	85.0	-50.0	0.000
7.50	85.0	-30.0	1.27e-3
7.50	85.0	-20.0	3.30e-2
7.50	85.0	-15.0	3.22e-2
7.50	85.0	-10.0	2.96e-2
7.50	85.0	-5.0	2.64e-2
7.50	85.0	-2.0	2.95e-2
7.50	85.0	0.0	6.39e-2
7.50	85.0	0.0	4.83e-2
7.50	85.0	2.0	5.96e-2
7.50	85.0	5.0	5.43e-2
7.50	85.0	10.0	4.20e-2
7.50	85.0	15.0	5.71e-3
7.50	85.0	20.0	9.47e-4
7.50	85.0	30.0	2.36e-5
7.50	85.0	50.0	3.55e-6
7.50	85.0	60.0	6.10e-6
7.50	85.0	90.0	6.10e-6
7.50	85.0	90.0	0.000
7.50	85.0	120.0	0.000
7.50	85.0	130.0	1.95e-5
7.50	85.0	150.0	4.91e-4
7.50	85.0	160.0	1.48e-2
7.50	85.0	165.0	1.24e-2
7.50	85.0	170.0	5.03e-3
7.50	85.0	175.0	5.12e-3
7.50	85.0	178.0	7.51e-3

LET	Tilt	Rot	XS
17.00	75.0	182.5	3.19e-2
17.00	75.0	185.0	3.13e-2
17.00	75.0	187.5	3.70e-2
17.00	75.0	190.0	3.00e-2
17.00	75.0	195.0	2.34e-2
17.00	75.0	200.0	1.73e-2
17.00	75.0	205.0	4.26e-3
17.00	75.0	215.0	0.000
17.00	75.0	225.0	0.000
17.00	75.0	240.0	0.000
17.00	75.0	255.0	0.000
17.00	75.0	270.0	6.10e-5
17.00	70.0	0.0	2.11e-2
17.00	70.0	0.0	1.13e-2
17.00	70.0	180.0	6.47e-2
17.00	70.0	180.0	5.77e-2
17.00	60.0	0.0	2.11e-2
17.00	60.0	0.0	1.98e-2
17.00	60.0	180.0	1.46e-2
17.00	60.0	180.0	1.25e-2
7.50	85.0	210.0	1.96e-5
7.50	85.0	230.0	1.77e-6
7.50	85.0	240.0	0.000
7.50	85.0	270.0	0.000
7.50	80.0	-90.0	0.000
7.50	80.0	-55.0	6.10e-6
7.50	80.0	-40.0	3.66e-5
7.50	80.0	-30.0	6.84e-4
7.50	80.0	-25.0	1.28e-3
7.50	80.0	-20.0	9.02e-3
7.50	80.0	-15.0	1.64e-2
7.50	80.0	-10.0	2.37e-2
7.50	80.0	-5.0	3.35e-2
7.50	80.0	0.0	2.11e-2
7.50	80.0	0.0	2.24e-2
7.50	80.0	5.0	1.25e-2
7.50	80.0	10.0	6.53e-3
7.50	80.0	15.0	7.15e-3
7.50	80.0	20.0	6.78e-3
7.50	80.0	25.0	3.73e-3
7.50	80.0	30.0	1.10e-4
7.50	80.0	40.0	0.000
7.50	80.0	55.0	0.000
7.50	80.0	90.0	0.000
7.50	80.0	90.0	0.000
7.50	80.0	125.0	0.000
7.50	80.0	140.0	0.000
7.50	80.0	150.0	4.88e-5
7.50	80.0	155.0	5.45e-5
7.50	80.0	160.0	2.50e-4
7.50	80.0	165.0	5.68e-4
7.50	80.0	170.0	1.64e-3
7.50	80.0	175.0	1.82e-3

LET	Tilt	Rot	XS
7.50	87.0	175.0	1.21e-2
7.50	87.0	180.0	2.88e-2
7.50	87.0	180.0	1.82e-2
7.50	87.0	185.0	1.86e-2
7.50	87.0	190.0	2.48e-2
7.50	87.0	190.0	2.02e-2
7.50	87.0	195.0	1.10e-2
7.50	80.0	210.0	6.71e-5
7.50	80.0	220.0	0.000
7.50	80.0	235.0	0.000
7.50	80.0	270.0	6.10e-6
7.50	75.0	-90.0	0.000
7.50	75.0	-60.0	0.000
7.50	75.0	-30.0	7.43e-4
7.50	75.0	-20.0	1.26e-2
7.50	75.0	-10.0	2.88e-2
7.50	75.0	-5.0	3.45e-2
7.50	75.0	0.0	2.85e-2
7.50	75.0	0.0	1.95e-2
7.50	75.0	5.0	1.18e-2
7.50	75.0	10.0	6.46e-3
7.50	75.0	20.0	9.52e-3
7.50	75.0	30.0	1.44e-3
7.50	75.0	60.0	6.10e-6
7.50	75.0	90.0	0.000
7.50	75.0	90.0	0.000
7.50	75.0	120.0	0.000
7.50	75.0	150.0	1.22e-5
7.50	75.0	160.0	3.05e-4
7.50	75.0	170.0	2.31e-3
7.50	75.0	175.0	1.70e-3
7.50	75.0	180.0	5.59e-3
7.50	75.0	180.0	4.39e-3
7.50	75.0	185.0	2.87e-3
7.50	75.0	190.0	4.99e-3
7.50	75.0	200.0	2.81e-3
7.50	75.0	210.0	9.75e-5
7.50	75.0	240.0	6.10e-6
7.50	75.0	270.0	0.000
7.50	0.0	0.0	0.000
7.50	0.0	0.0	4.07e-6
7.50	0.0	180.0	0.000
7.50	0.0	180.0	2.03e-6
2.38	87.0	-25.0	2.64e-4
2.38	87.0	-20.0	9.03e-4
2.38	87.0	-15.0	2.88e-3
2.38	87.0	-10.0	3.74e-3
2.38	80.0	-90.0	0.000
2.38	80.0	-60.0	0.000
2.38	80.0	-30.0	3.05e-6
2.38	80.0	-25.0	7.16e-6
2.38	80.0	-20.0	1.61e-4
2.38	80.0	-15.0	2.86e-4

LET	Tilt	Rot	XS
7.50	85.0	180.0	9.19e-3
7.50	85.0	180.0	7.50e-3
7.50	85.0	182.0	4.01e-3
7.50	85.0	185.0	4.42e-3
7.50	85.0	190.0	1.48e-2
7.50	85.0	195.0	8.40e-3
7.50	85.0	200.0	1.26e-3
2.38	87.0	-10.0	3.10e-3
2.38	87.0	-5.0	1.80e-3
2.38	87.0	0.0	4.52e-3
2.38	87.0	0.0	5.86e-3
2.38	87.0	5.0	3.02e-3
2.38	87.0	10.0	1.14e-3
2.38	87.0	10.0	1.55e-3
2.38	87.0	15.0	4.96e-4
2.38	87.0	20.0	2.44e-5
2.38	87.0	25.0	0.000
2.38	87.0	155.0	1.51e-4
2.38	87.0	160.0	7.32e-4
2.38	87.0	165.0	6.45e-4
2.38	87.0	170.0	4.48e-4
2.38	87.0	170.0	2.82e-4
2.38	87.0	175.0	6.10e-4
2.38	87.0	180.0	1.46e-3
2.38	87.0	180.0	1.46e-3
2.38	87.0	185.0	7.93e-4
2.38	87.0	190.0	2.03e-4
2.38	87.0	190.0	4.23e-4
2.38	87.0	195.0	1.49e-4
2.38	87.0	200.0	4.88e-5
2.38	87.0	205.0	0.000
2.38	85.0	-90.0	0.000
2.38	85.0	-60.0	0.000
2.38	85.0	-50.0	6.10e-6
2.38	85.0	-30.0	5.49e-5
2.38	85.0	-20.0	9.16e-4
2.38	85.0	-15.0	1.32e-3
2.38	85.0	-12.0	3.29e-3
2.38	85.0	-10.0	4.78e-3
2.38	85.0	-5.0	3.33e-3
2.38	85.0	-2.0	3.66e-3
2.38	85.0	0.0	1.98e-3
2.38	85.0	0.0	2.01e-3
2.38	85.0	0.0	4.19e-3
2.38	85.0	0.0	2.99e-3
2.38	85.0	2.0	3.61e-3
2.38	85.0	5.0	2.24e-3
2.38	80.0	185.0	3.05e-5
2.38	80.0	190.0	4.40e-5
2.38	80.0	195.0	6.66e-5
2.38	80.0	200.0	3.90e-5
2.38	80.0	205.0	3.58e-5
2.38	80.0	210.0	0.000

LET	Tilt	Rot	XS
7.50	80.0	180.0	1.30e-3
7.50	80.0	180.0	9.52e-4
7.50	80.0	185.0	2.32e-3
7.50	80.0	190.0	5.86e-3
7.50	80.0	195.0	4.96e-3
7.50	80.0	200.0	1.45e-3
7.50	80.0	205.0	5.77e-4
2.38	85.0	10.0	1.58e-3
2.38	85.0	12.0	9.26e-4
2.38	85.0	15.0	1.58e-4
2.38	85.0	20.0	2.01e-4
2.38	85.0	30.0	5.49e-5
2.38	85.0	50.0	0.000
2.38	85.0	60.0	0.000
2.38	85.0	90.0	0.000
2.38	85.0	90.0	0.000
2.38	85.0	120.0	0.000
2.38	85.0	130.0	0.000
2.38	85.0	150.0	1.22e-5
2.38	85.0	160.0	3.42e-4
2.38	85.0	165.0	2.76e-4
2.38	85.0	168.0	2.40e-4
2.38	85.0	170.0	1.41e-4
2.38	85.0	175.0	1.90e-4
2.38	85.0	178.0	2.06e-4
2.38	85.0	180.0	3.62e-4
2.38	85.0	180.0	3.52e-4
2.38	85.0	180.0	4.73e-4
2.38	85.0	180.0	4.43e-4
2.38	85.0	182.0	7.21e-4
2.38	85.0	185.0	1.90e-4
2.38	85.0	190.0	2.57e-4
2.38	85.0	192.0	2.74e-4
2.38	85.0	195.0	8.44e-5
2.38	85.0	200.0	5.49e-5
2.38	85.0	210.0	6.10e-6
2.38	85.0	230.0	0.000
2.38	85.0	240.0	0.000
2.38	85.0	270.0	0.000
2.38	83.0	-3.5	5.52e-3
2.38	83.0	3.5	2.25e-3
2.38	83.0	176.5	3.89e-5
2.38	83.0	183.5	5.96e-5
2.38	82.5	0.0	2.90e-3
2.38	82.5	0.0	2.32e-3
2.38	82.5	180.0	0.000
2.38	82.5	180.0	1.22e-4
2.38	75.0	180.0	1.08e-5
2.38	75.0	180.0	6.10e-5
2.38	75.0	180.0	0.000
2.38	75.0	182.5	1.83e-5
2.38	75.0	183.5	2.05e-5
2.38	75.0	185.0	0.000

LET	Tilt	Rot	XS
2.38	80.0	-10.0	6.93e-4
2.38	80.0	-5.0	5.10e-3
2.38	80.0	-5.0	1.23e-3
2.38	80.0	-3.5	5.07e-3
2.38	80.0	0.0	2.96e-3
2.38	80.0	0.0	2.35e-3
2.38	80.0	0.0	1.38e-3
2.38	80.0	0.0	1.30e-3
2.38	80.0	3.5	1.72e-3
2.38	80.0	5.0	5.05e-4
2.38	80.0	5.0	1.74e-3
2.38	80.0	10.0	1.96e-3
2.38	80.0	15.0	1.92e-3
2.38	80.0	20.0	3.93e-4
2.38	80.0	25.0	3.58e-5
2.38	80.0	30.0	2.44e-5
2.38	80.0	60.0	0.000
2.38	80.0	90.0	0.000
2.38	80.0	90.0	0.000
2.38	80.0	120.0	0.000
2.38	80.0	150.0	3.05e-6
2.38	80.0	155.0	0.000
2.38	80.0	160.0	4.88e-6
2.38	80.0	165.0	8.32e-6
2.38	80.0	170.0	1.81e-5
2.38	80.0	175.0	1.39e-5
2.38	80.0	175.0	0.000
2.38	80.0	176.5	5.31e-6
2.38	80.0	180.0	3.15e-5
2.38	80.0	180.0	2.76e-5
2.38	80.0	180.0	3.05e-5
2.38	80.0	180.0	3.05e-5
2.38	80.0	183.5	1.59e-5
2.38	80.0	185.0	9.16e-5

LET	Tilt	Rot	XS
2.38	80.0	240.0	0.000
2.38	80.0	270.0	0.000
2.38	75.0	-25.0	0.000
2.38	75.0	-20.0	7.32e-5
2.38	75.0	-15.0	2.38e-4
2.38	75.0	-10.0	4.27e-4
2.38	75.0	-7.5	4.03e-4
2.38	75.0	-5.0	5.47e-4
2.38	75.0	-5.0	4.52e-4
2.38	75.0	-3.5	6.84e-4
2.38	75.0	-2.5	3.85e-4
2.38	75.0	0.0	3.05e-4
2.38	75.0	0.0	2.14e-4
2.38	75.0	0.0	2.00e-3
2.38	75.0	0.0	1.48e-3
2.38	75.0	2.5	2.75e-4
2.38	75.0	3.5	2.46e-4
2.38	75.0	5.0	2.69e-4
2.38	75.0	5.0	6.07e-5
2.38	75.0	7.5	3.54e-4
2.38	75.0	10.0	9.22e-4
2.38	75.0	15.0	4.58e-4
2.38	75.0	20.0	1.40e-4
2.38	75.0	25.0	1.83e-5
2.38	75.0	155.0	0.000
2.38	75.0	160.0	0.000
2.38	75.0	165.0	0.000
2.38	75.0	170.0	2.44e-5
2.38	75.0	172.5	1.83e-5
2.38	75.0	175.0	1.22e-5
2.38	75.0	175.0	0.000
2.38	75.0	176.5	1.76e-5
2.38	75.0	177.5	1.83e-5
2.38	75.0	180.0	4.67e-5

LET	Tilt	Rot	XS
2.38	75.0	185.0	1.22e-5
2.38	75.0	187.5	4.88e-5
2.38	75.0	190.0	0.000
2.38	75.0	195.0	1.22e-5
2.38	75.0	200.0	1.83e-5
2.38	75.0	205.0	0.000
2.38	70.0	-3.5	3.66e-5
2.38	70.0	3.5	3.05e-5
2.38	70.0	176.5	0.000
2.38	70.0	183.5	2.14e-5
2.38	65.0	-3.5	0.000
2.38	65.0	3.5	1.83e-5
2.38	65.0	176.5	0.000
2.38	65.0	183.5	1.53e-5
1.29	87.0	0.0	5.04e-4
1.29	87.0	0.0	3.05e-4
1.29	87.0	180.0	3.51e-4
1.29	87.0	180.0	1.37e-4
1.29	85.0	-60.0	0.000
1.29	85.0	-50.0	0.000
1.29	85.0	-30.0	9.16e-6
1.29	85.0	-10.0	2.30e-4
1.29	85.0	-5.0	2.20e-4
1.29	85.0	-4.0	1.66e-4
1.29	85.0	-2.0	1.83e-4
1.29	85.0	0.0	3.96e-4
1.29	85.0	0.0	3.30e-4
1.29	85.0	2.0	3.31e-4
1.29	85.0	4.0	2.17e-4
1.29	85.0	5.0	3.17e-4
1.29	85.0	10.0	1.73e-4
1.29	85.0	30.0	1.53e-5
1.29	85.0	50.0	0.000
1.29	85.0	60.0	0.000

1.29	85.0	120.0	0.000
1.29	85.0	130.0	0.000
1.29	85.0	150.0	0.000
1.29	85.0	170.0	2.64e-5
1.29	85.0	175.0	2.44e-5
1.29	85.0	176.0	2.52e-5
1.29	85.0	178.0	6.79e-5
1.29	85.0	180.0	4.71e-5
1.29	85.0	180.0	5.66e-5
1.29	85.0	182.0	4.24e-5
1.29	85.0	184.0	4.04e-5
1.29	85.0	185.0	4.27e-5
1.29	85.0	190.0	3.66e-5
1.29	85.0	210.0	0.000
1.29	85.0	230.0	0.000
1.29	85.0	240.0	0.000

Section VIII provided the template for all calculation methods, so here we just discuss the differences between the calculations used there and the calculations used here. One difference is that the example data set considered here has much more scatter than the example in Section VIII (e.g., compare the points in Fig. 23 to the points in Fig. 12). In view of this scatter, no fit to the data is going to be a good fit. The best fit as defined by a least-square error measure will go through the center of the scatter. The fit will underestimate some points and overestimate others. A small amount of conservatism can be built into the fit by reducing the underestimates at the expense of increasing some of the overestimates. This is done through a weighting factor used in the least-square error measure. Recall from Section VIII that the weight factor w in Appendix D was selected to give more weight to the smaller LETs because the upset rate is weighted by flux which gives more weight to the smaller LETs. This is still desired, but now we want to also give more weight to the larger cross sections when comparing different cross sections at the same LET so that the larger cross sections associated with scatter in the data will be favored over the smaller cross sections. The weight factor is now a product of two terms, the first is weighted by LET and the second is weighted by cross section. Also, LET is now in Column 1 of the spreadsheet and cross section is in Column 4, so the single line for w in Appendix D is replaced by the three lines:

$$\begin{aligned}
 w1 &= 1/\text{col}(1)^3 \\
 w2 &= (1+1e6*\text{col}(4))^{0.5} \\
 w &= w1*w2
 \end{aligned}$$

Another difference between this example and the previous example is that, for this example, assigning $2\mu\text{m}$ to T does not give a good fit to the data regardless of how the other parameters are selected. Therefore, T is now made to be one of the adjustable parameters. This is done by deactivating the line containing T (by inserting a semicolon to the left of the line) in the “Equation” box of Appendix D, and activating the lines containing T (by removing the semicolons but leaving the remainder of the lines as is) in the “Constraints” and “Initial Parameters” boxes. Other than these modifications, and changing all column numbers to reflect the new locations of the variables in the spreadsheet, the Regression Wizard programming is given in Appendix D. The values for the fitting parameters obtained from the Regression Wizard for this example are shown in the upper portion (denoted “Model Parameters”) of Table 4. Recall that the fitting parameters tend to be slightly conservative because of the cross section weighting.

Table 4. Model and Weibull parameters for a later version of SRAM6 in all-1's

Model Parameters (slightly conservative)	
A = 0.1474	B = 0.7419
L01 = 0	L02 = 1.850e7
S01 = 0.4613	S02 = 2.371e4
phi_off = -8.898e-3	h = -6.067e-2
P = 0.1868	T = 1.079
Weibull Parameters (inputs for a CREME96 calculation of heavy-ion rates in space)	
Onset = 0.2 MeV-cm ² /mg	Width = 61.06 MeV-cm ² /mg
Exponent = 2.552	Limiting XS = 0.310 μm ² /bit
X = Y = Z = 0.557 μm	funnel = 0

Note: A CREME96 calculation using the Weibull parameters gives a GCR rate of 1.6×10^{-10} /bit-day for the all-1's pattern.

Data used to plot the fits are constructed from the transform in Appendix E as explained in Section VIII, except that the entries in the “Assign parameters” box are taken from Table 4, and the column numbers in the “Assign variables” and “Assign output column” boxes are changed to reflect the new locations of the variables in the spreadsheet. Plotting the data produces the curves in Figs. 23 to 25.

When inspecting Figs. 23 to 25 to see how well the curves represent the points, three issues should be considered. The first issue is that scatter in the data makes a good fit impossible. The second issue, regarding rotation sweeps, is that calculated upset rates in space are controlled by the areas under the curves when cross section is plotted on a linear scale (which was done in these plots). This is not exactly true for the tilt sweeps because calculated rates in space are weighted by the sine of the tilt angle, but most of the contribution to calculated rates is from the larger tilt angles where this weighting is roughly uniform, so calculated rates in space are roughly controlled by the areas under the curves. Therefore, for either a rotation sweep or a tilt sweep, a good fit to individual points is less essential compared to having the fit produce the correct area under the curve. The third issue involves conservatism. A small amount of conservatism was intentionally included (via a cross section weighting) so that calculated rates in space are unlikely to be underestimates. The conservatism might appear to be excessive when the LET is 25, e.g., the areas under the tilt sweep curves at an LET of 25 appear to be excessively large. The reason is that the LET weighting used by the fitting algorithm gives the smallest weight to the largest LET, so a large amount of conservatism at an LET of 25 is tolerated by the fitting algorithm when this improves the fit at the smaller LETs. However, calculated rates in space also give the least weighting to the largest LETs (via a flux weighting). Therefore, what might appear to be excessive conservatism at an LET of 25, when looking at the areas under the curves in the rotation sweeps and tilt sweeps, actually corresponds to only a small amount of conservatism in calculated rates.

The upset rate from galactic cosmic rays in interplanetary space during solar minimum and behind 100 mils of spacecraft shielding is calculated the same way as in the previous

section, using the same flux data as in Fig. 21, but this time the entries in the “XSAVG” column were obtained by using the upper portion of Table 4 as the input to the FORTRAN code in Appendix F. The calculated rate for the newer version of SRAM6 in the all-1’s pattern is 2.05×10^{-10} /bit-day. The spreadsheet calculation shows that only about 10% of this calculated rate is from ions having an LET less than 1.58 MeV-cm²/mg, and only about 27% is from LET greater than 17.8 MeV-cm²/mg. The most important contribution is from ions having LET between 1.58 and 18 MeV-cm²/mg.

The above rate calculation requires users to import flux data from a source such as CREME96 and then construct a spreadsheet that numerically integrates cross section with flux. An alternate and nearly equivalent calculation can be performed entirely by CREME96.³ This calculation method would be convenient when considering other heavy-ion environments for which flux data have not been given here. Inputs needed for this calculation include Weibull parameters describing the directional-average cross section. The directional-average cross section is obtained from the code in Appendix F, using inputs in the upper portion of Table 4, and is shown as the solid curve in Fig. 26. As pointed out in the previous paragraph, the cross section for LET less than 1 MeV-cm²/mg is too small to be an important contribution to the upset rate, so Fig. 26 starts the plot at an LET of 1 MeV-cm²/mg. The dashed curve is a Weibull fit to the solid curve using Weibull parameters indicated in the lower portion of Table 4 (the X, Y, and Z table entries are discussed below). Recall that the directional-average cross section has the directional dependence of device susceptibility already built into it, so this cross section is integrated with a raw (meaning that no directional effects are built into it) heavy-ion flux (as a function of LET) to obtain the upset rate. The rate calculation is the same calculation that would be used if device susceptibility were isotropic and described by the curve in Fig. 26 for all directions. Therefore, the rate calculation that uses this curve should reflect an isotropic device. CREME96 uses the RPP model for rate calculations, so RPP dimensions should be chosen to represent an isotropic device. This is done by selecting the RPPs to be cubes (i.e., all three RPP dimensions are equal), which are not perfectly isotropic but are as close to isotropic as the RPP model can be. Taking the RPP dimensions to be the square root of the asymptotic value of the cross section produces the remainder of the entries in the lower portion of Table 4. This table lists all of the device-related inputs needed by CREME96 to perform a heavy-ion rate calculation after a heavy-ion environment has been constructed by CREME96. In particular, the upset rate from galactic cosmic rays in interplanetary space during solar minimum and behind 100 mils of spacecraft shielding is calculated by CREME96 using Table 4 inputs to be 1.63×10^{-10} /bit-day. This is very close to the spreadsheet calculation (2.05×10^{-10} /bit-day) given in the previous paragraph.

³ CREME96 has been replaced by CRÈME-MC at the new website <https://creme.isde.vanderbilt.edu/>. However, the new code includes (among other things) all of the data sets and algorithms used by the original CREME96, so calculations performed by the original code can be duplicated by the new code.

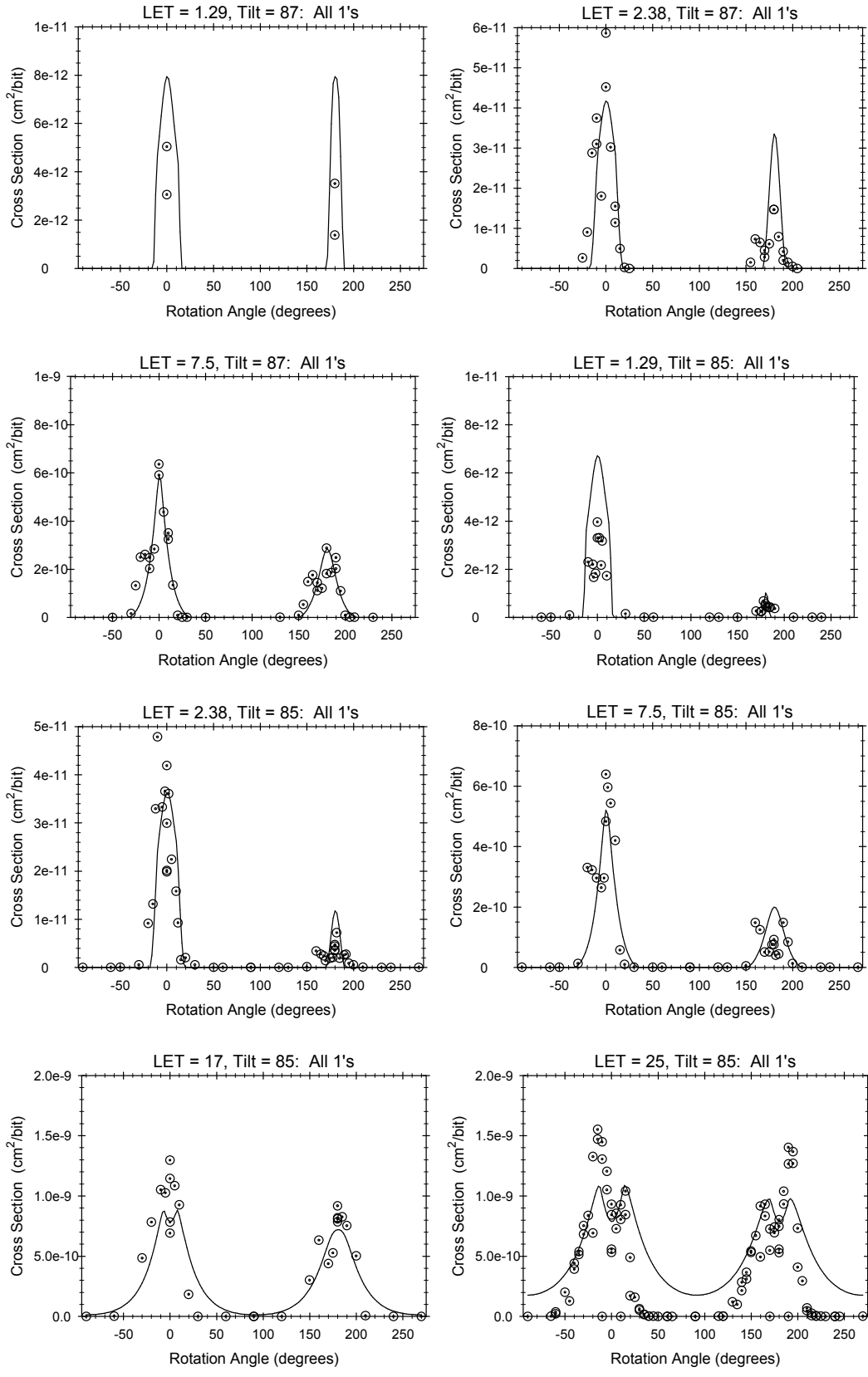


Fig. 23. Rotation sweeps for a later version of SRAM6 in all-1's (page 1 of 3).

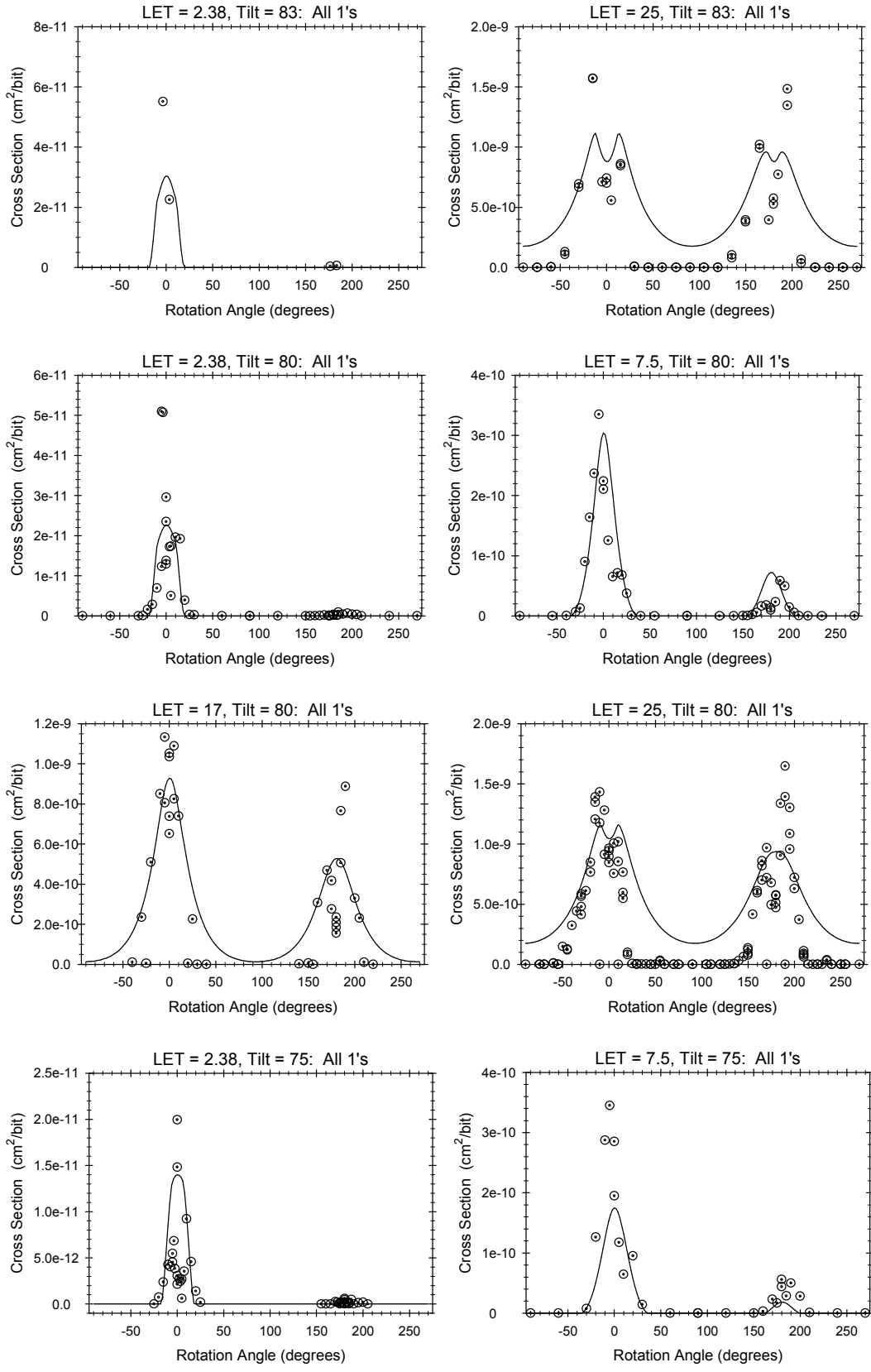


Fig. 23. Rotation sweeps for a later version of SRAM6 in all-1's (page 2 of 3).

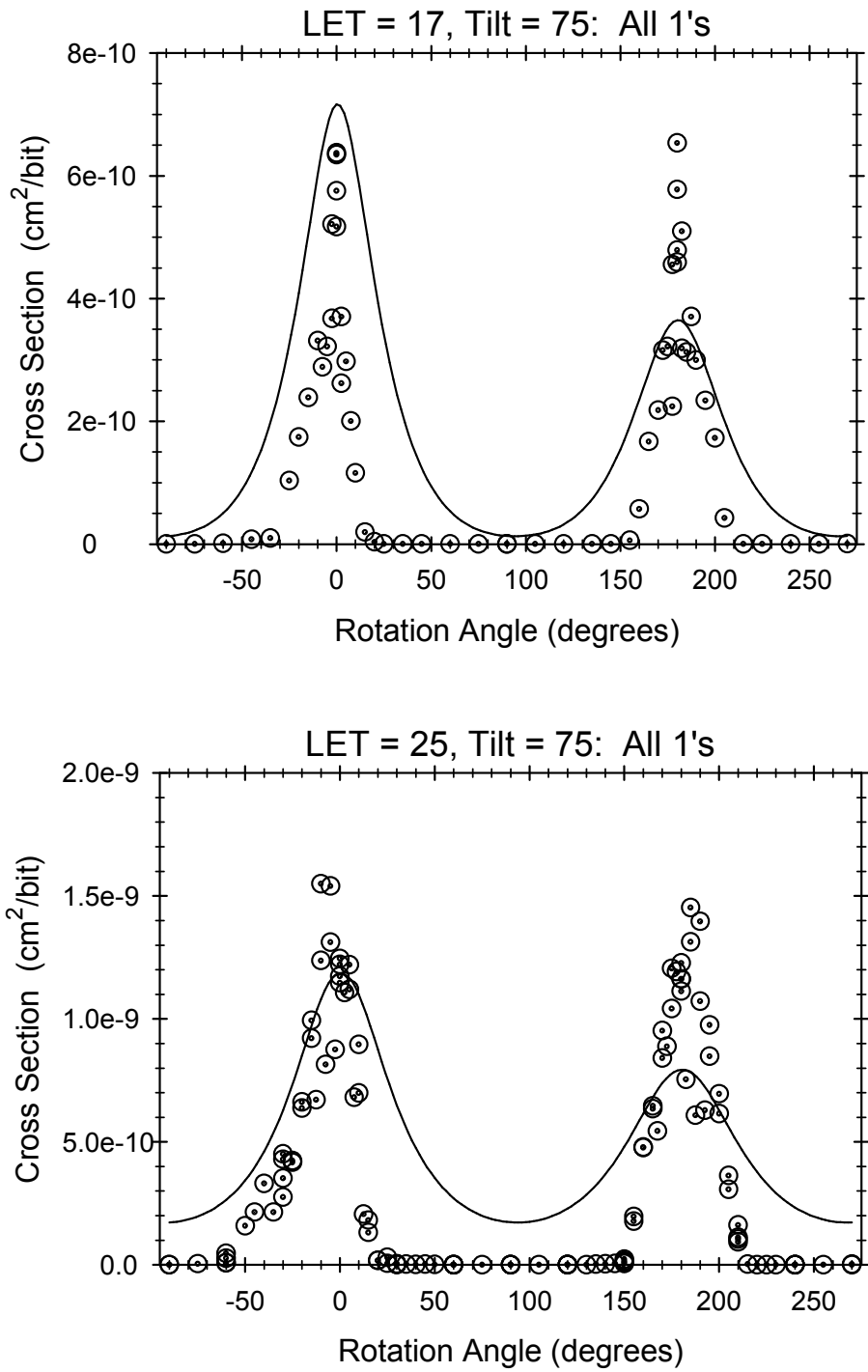


Fig. 23. Rotation sweeps for a later version of SRAM6 in all-1's (page 3 of 3).

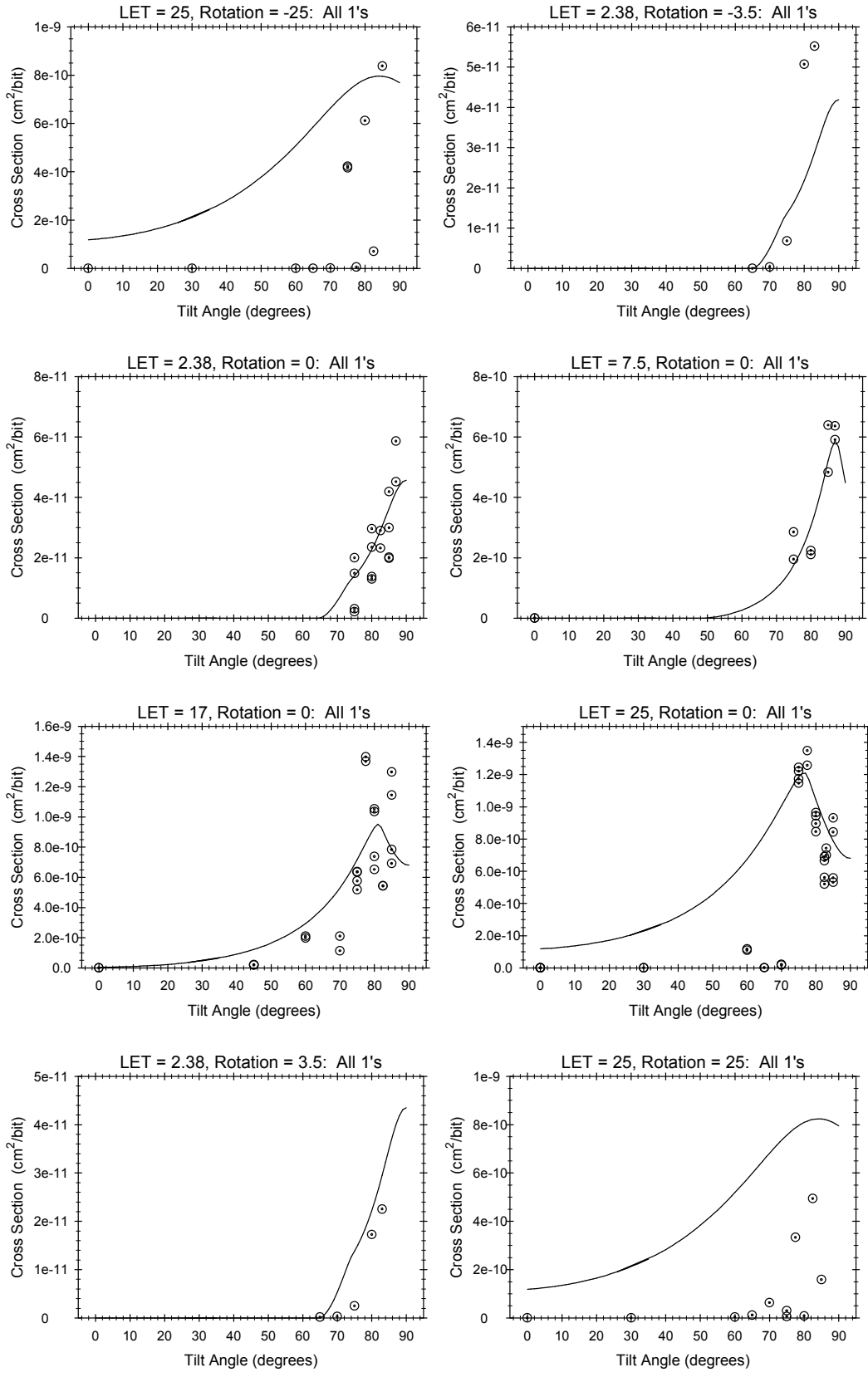


Fig. 24. Tilt sweeps for a later version of SRAM6 in all-1's (page 1 of 2).

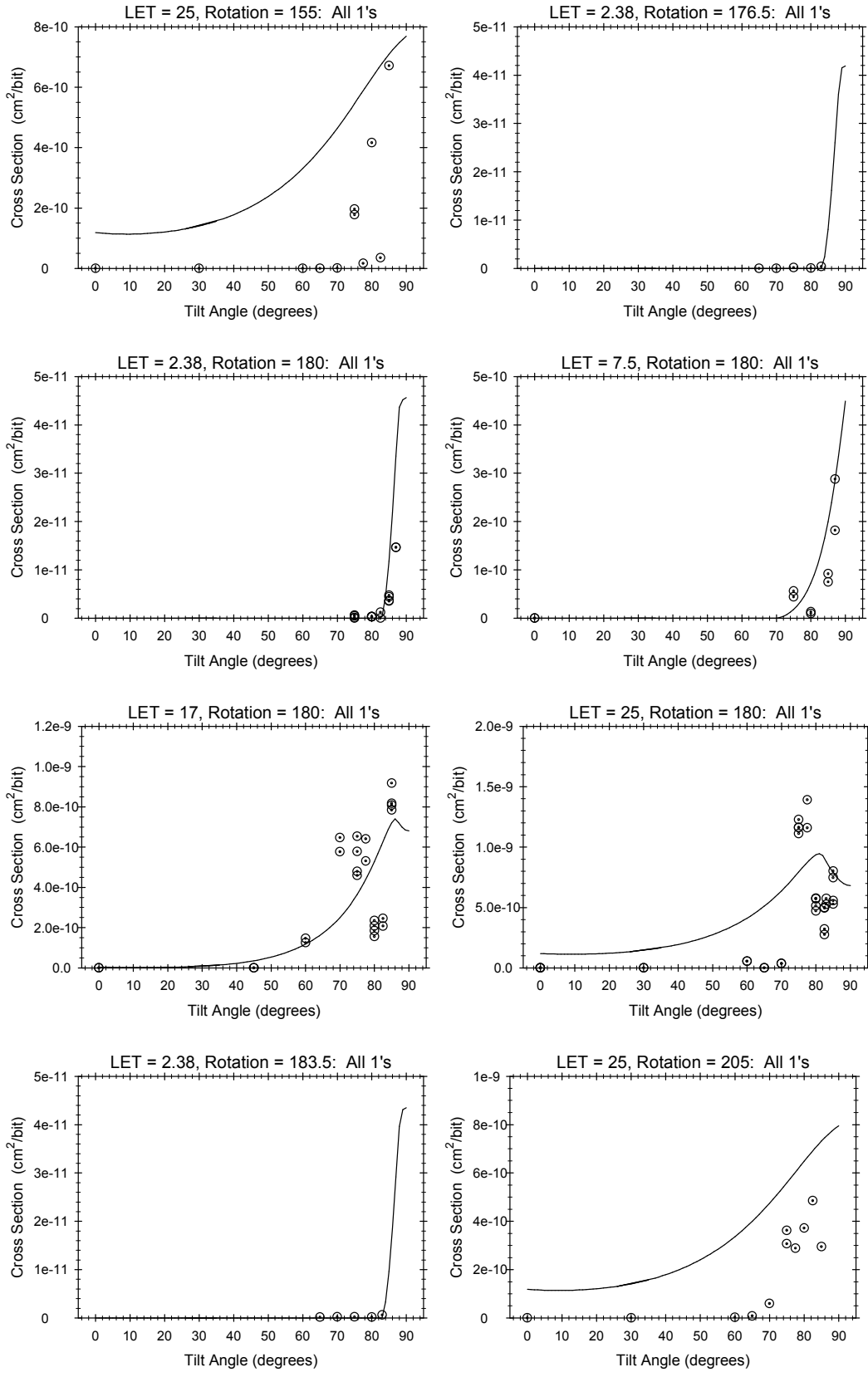


Fig. 24. Tilt sweeps for a later version of SRAM6 in all-1's (page 2 of 2).

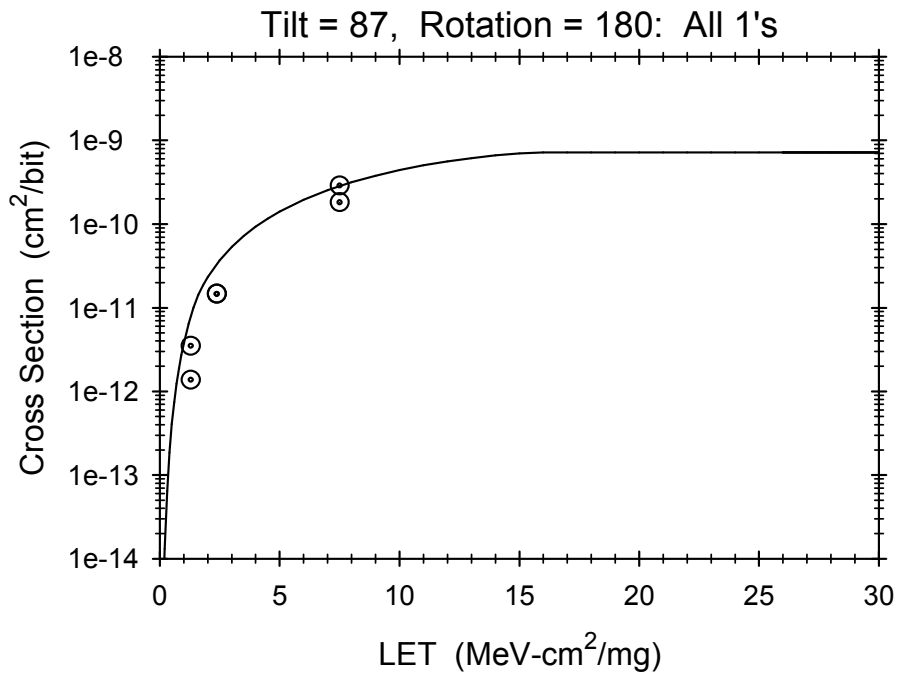
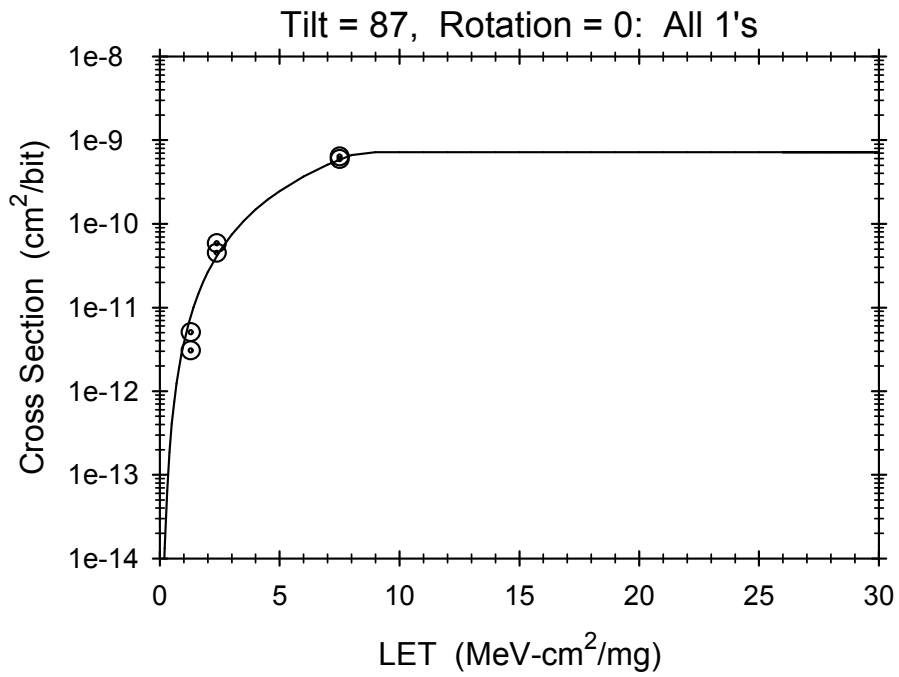


Fig. 25. LET sweeps for a later version of SRAM6 in all-1's.

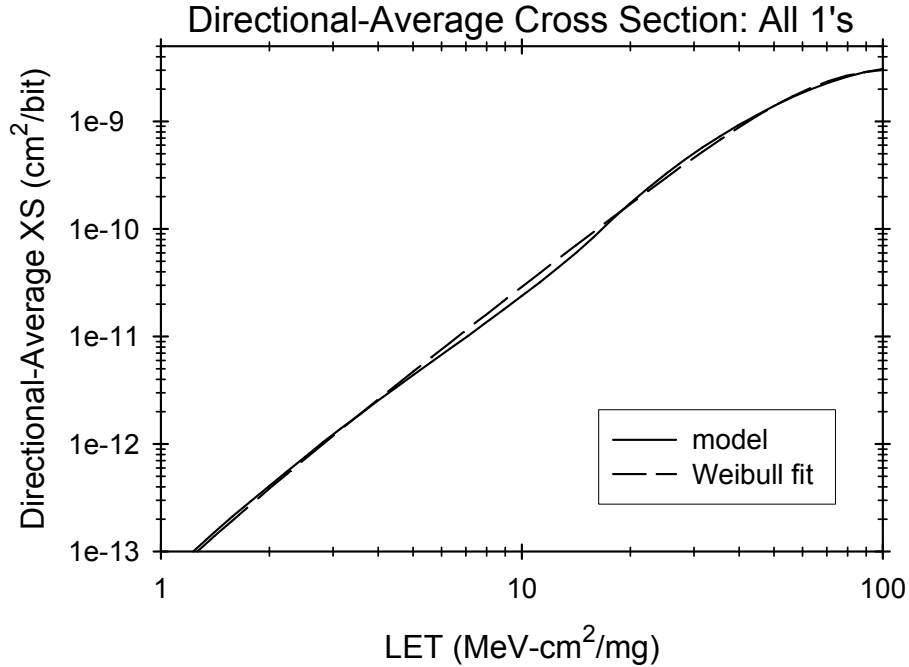


Fig. 26. The directional-average cross section (solid curve) produced by the code in Appendix F using inputs from Table IV applies to the later version of the SRAM6 in all-1's. The Weibull fit (dashed curve), using Weibull parameters in Table V, is nearly identical to the original curve over the plotted range. The plotted range represents the LET values that are most important for calculating heavy-ion rates in space.

B. The All-0's Pattern

The data from [11] for the all-0's are reproduced here in Fig. 27. A set of sweeps selected so that every data point is included in at least one sweep is shown as the set of points in Figs. 28, 29, and 30 (the curves are discussed later). As pointed out in previous discussions regarding the way different angles are weighted by flux when calculating SEU rates, the relative importance of different angles at the same LET can be seen by using the same vertical scale in the plots. Therefore, to show the relative importance of different angles, all rotation sweeps and tilt sweeps at the same LET use the same linear vertical scale in Figs. 28 and 29.

Fig. 27. Measured Data for a later version of SRAM6 in all-0's.

LET	Tilt	Rot	XS	LET	Tilt	Rot	XS	LET	Tilt	Rot	XS
25.00	85.0	-90.0	0.000	25.00	85.0	40.0	0.000	25.00	85.0	200.0	4.82e-5
25.00	85.0	-60.0	0.000	25.00	85.0	40.0	6.10e-6	25.00	85.0	200.0	8.54e-5
25.00	85.0	-50.0	1.22e-5	25.00	85.0	45.0	0.000	25.00	85.0	200.0	1.83e-5
25.00	85.0	-45.0	9.99e-6	25.00	85.0	50.0	0.000	25.00	85.0	205.0	1.83e-5
25.00	85.0	-40.0	0.000	25.00	85.0	60.0	6.10e-6	25.00	85.0	210.0	0.000
25.00	85.0	-40.0	1.53e-5	25.00	85.0	90.0	0.000	25.00	85.0	215.0	0.000
25.00	85.0	-35.0	0.000	25.00	85.0	90.0	0.000	25.00	85.0	220.0	0.000
25.00	85.0	-30.0	0.000	25.00	85.0	120.0	6.10e-6	25.00	85.0	220.0	3.05e-5
25.00	85.0	-25.0	6.10e-6	25.00	85.0	130.0	0.000	25.00	85.0	225.0	0.000
25.00	85.0	-20.0	3.86e-5	25.00	85.0	135.0	2.00e-5	25.00	85.0	230.0	1.22e-5
25.00	85.0	-20.0	9.16e-5	25.00	85.0	140.0	0.000	25.00	85.0	240.0	0.000
25.00	85.0	-20.0	3.05e-5	25.00	85.0	140.0	0.000	25.00	85.0	270.0	0.000
25.00	85.0	-15.0	3.24e-4	25.00	85.0	145.0	0.000	25.00	83.0	-90.0	0.000
25.00	85.0	-15.0	4.27e-4	25.00	85.0	150.0	0.000	25.00	83.0	-75.0	6.36e-6
25.00	85.0	-15.0	4.58e-4	25.00	85.0	155.0	9.77e-5	25.00	83.0	-60.0	0.000
25.00	85.0	-10.0	2.32e-2	25.00	85.0	160.0	5.90e-3	25.00	83.0	-60.0	5.35e-6
25.00	85.0	-10.0	3.43e-2	25.00	85.0	160.0	7.52e-4	25.00	83.0	-45.0	0.000
25.00	85.0	-5.0	1.37e-1	25.00	85.0	160.0	4.73e-3	25.00	83.0	-45.0	0.000
25.00	85.0	-5.0	1.76e-1	25.00	85.0	165.0	6.14e-2	25.00	83.0	-30.0	1.22e-5
25.00	85.0	0.0	1.75e-1	25.00	85.0	165.0	2.00e-3	25.00	83.0	-30.0	5.87e-6
25.00	85.0	0.0	2.16e-1	25.00	85.0	165.0	5.59e-2	25.00	83.0	-15.0	4.91e-4
25.00	85.0	0.0	1.85e-1	25.00	85.0	170.0	1.52e-1	25.00	83.0	-15.0	1.63e-4
25.00	85.0	0.0	2.15e-1	25.00	85.0	170.0	1.51e-1	25.00	83.0	0.0	1.74e-1
25.00	85.0	0.0	2.24e-1	25.00	85.0	175.0	2.68e-1	25.00	83.0	0.0	1.53e-1
25.00	85.0	0.0	2.57e-1	25.00	85.0	175.0	2.83e-1	25.00	83.0	15.0	2.72e-2
25.00	85.0	0.0	2.56e-1	25.00	85.0	180.0	2.80e-1	25.00	83.0	15.0	4.31e-2
25.00	85.0	0.0	2.83e-1	25.00	85.0	180.0	3.18e-1	25.00	83.0	30.0	1.17e-5
25.00	85.0	5.0	2.79e-1	25.00	85.0	180.0	2.98e-1	25.00	83.0	30.0	0.000
25.00	85.0	5.0	3.02e-1	25.00	85.0	180.0	3.35e-1	25.00	83.0	45.0	0.000
25.00	85.0	10.0	2.00e-1	25.00	85.0	180.0	2.12e-1	25.00	83.0	45.0	0.000
25.00	85.0	10.0	2.06e-1	25.00	85.0	180.0	2.78e-1	25.00	83.0	60.0	5.87e-6
25.00	85.0	15.0	7.65e-2	25.00	85.0	180.0	2.21e-1	25.00	83.0	60.0	5.35e-6
25.00	85.0	15.0	2.79e-3	25.00	85.0	180.0	2.65e-1	25.00	83.0	75.0	0.000
25.00	85.0	15.0	6.71e-2	25.00	85.0	185.0	2.38e-1	25.00	83.0	90.0	0.000
25.00	85.0	20.0	4.93e-3	25.00	85.0	185.0	2.44e-1	25.00	83.0	90.0	0.000
25.00	85.0	20.0	5.50e-4	25.00	85.0	190.0	2.16e-2	25.00	83.0	105.0	0.000
25.00	85.0	20.0	3.38e-3	25.00	85.0	190.0	3.64e-2	25.00	83.0	120.0	0.000
25.00	85.0	25.0	6.10e-5	25.00	85.0	195.0	2.59e-4	25.00	83.0	120.0	5.87e-6
25.00	85.0	30.0	1.83e-5	25.00	85.0	195.0	5.09e-4	25.00	83.0	135.0	0.000
25.00	85.0	35.0	2.03e-5	25.00	85.0	195.0	7.93e-4	25.00	83.0	135.0	0.000
25.00	83.0	150.0	0.000	25.00	80.0	-15.0	1.78e-4	25.00	80.0	160.0	1.00e-3
25.00	83.0	150.0	1.22e-5	25.00	80.0	-10.0	2.65e-3	25.00	80.0	165.0	1.90e-2
25.00	83.0	165.0	2.93e-2	25.00	80.0	-10.0	8.63e-3	25.00	80.0	165.0	2.95e-2
25.00	83.0	165.0	4.75e-2	25.00	80.0	-5.0	4.50e-2	25.00	80.0	165.0	2.02e-2
25.00	83.0	180.0	2.64e-1	25.00	80.0	0.0	1.08e-1	25.00	80.0	165.0	1.04e-4
25.00	83.0	180.0	2.74e-1	25.00	80.0	0.0	1.00e-1	25.00	80.0	170.0	6.91e-2
25.00	83.0	195.0	6.75e-4	25.00	80.0	0.0	1.14e-1	25.00	80.0	170.0	6.82e-2
25.00	83.0	195.0	3.87e-4	25.00	80.0	0.0	1.21e-1	25.00	80.0	175.0	1.08e-1
25.00	83.0	210.0	2.43e-5	25.00	80.0	5.0	1.05e-1	25.00	80.0	180.0	1.33e-1
25.00	83.0	210.0	2.35e-5	25.00	80.0	10.0	6.22e-2	25.00	80.0	180.0	1.34e-1
25.00	83.0	225.0	0.000	25.00	80.0	10.0	5.89e-2	25.00	80.0	180.0	1.30e-1

LET	Tilt	Rot	XS
25.00	83.0	225.0	0.000
25.00	83.0	240.0	5.35e-6
25.00	83.0	240.0	0.000
25.00	83.0	255.0	0.000
25.00	83.0	270.0	0.000
25.00	82.5	0.0	1.19e-1
25.00	82.5	0.0	1.28e-1
25.00	82.5	0.0	1.93e-1
25.00	82.5	0.0	2.02e-1
25.00	82.5	180.0	1.70e-1
25.00	82.5	180.0	1.73e-1
25.00	82.5	180.0	1.47e-1
25.00	82.5	180.0	1.56e-1
25.00	80.0	-90.0	0.000
25.00	80.0	-70.0	0.000
25.00	80.0	-70.0	0.000
25.00	80.0	-55.0	0.000
25.00	80.0	-55.0	0.000
25.00	80.0	-45.0	0.000
25.00	80.0	-40.0	0.000
25.00	80.0	-30.0	0.000
25.00	80.0	-30.0	4.07e-6
25.00	80.0	-25.0	1.36e-5
25.00	80.0	-25.0	0.000
25.00	80.0	-20.0	6.57e-5
25.00	80.0	-20.0	1.05e-5
25.00	80.0	-15.0	2.44e-5
25.00	80.0	-15.0	6.67e-5
25.00	80.0	-15.0	4.88e-4
25.00	75.0	-30.0	0.000
25.00	75.0	-30.0	5.08e-6
25.00	75.0	-25.0	0.000
25.00	75.0	-20.0	6.10e-6
25.00	75.0	-20.0	1.02e-5
25.00	75.0	-15.0	7.93e-5
25.00	75.0	-15.0	6.10e-5
25.00	75.0	-10.0	2.08e-4
25.00	75.0	-10.0	1.44e-4
25.00	75.0	-5.0	8.00e-4
25.00	75.0	-5.0	9.16e-4
25.00	75.0	0.0	1.96e-3
25.00	75.0	0.0	1.61e-3
25.00	75.0	0.0	1.71e-3
25.00	75.0	0.0	2.77e-3
25.00	75.0	5.0	2.95e-3
25.00	75.0	5.0	2.05e-3
25.00	75.0	10.0	2.10e-3
25.00	75.0	10.0	1.56e-3
25.00	75.0	15.0	7.63e-4
25.00	75.0	15.0	8.18e-4
25.00	75.0	20.0	6.10e-5
25.00	75.0	20.0	1.40e-4
25.00	75.0	25.0	6.10e-6

LET	Tilt	Rot	XS
25.00	80.0	15.0	1.20e-2
25.00	80.0	15.0	1.40e-4
25.00	80.0	15.0	1.17e-2
25.00	80.0	15.0	1.87e-2
25.00	80.0	20.0	1.69e-3
25.00	80.0	20.0	6.19e-4
25.00	80.0	25.0	0.000
25.00	80.0	25.0	4.07e-5
25.00	80.0	30.0	6.10e-6
25.00	80.0	30.0	4.07e-6
25.00	80.0	40.0	5.81e-6
25.00	80.0	45.0	0.000
25.00	80.0	55.0	0.000
25.00	80.0	55.0	0.000
25.00	80.0	70.0	0.000
25.00	80.0	70.0	0.000
25.00	80.0	90.0	0.000
25.00	80.0	90.0	0.000
25.00	80.0	110.0	0.000
25.00	80.0	110.0	0.000
25.00	80.0	125.0	0.000
25.00	80.0	125.0	0.000
25.00	80.0	135.0	0.000
25.00	80.0	140.0	0.000
25.00	80.0	150.0	4.88e-5
25.00	80.0	150.0	1.83e-5
25.00	80.0	155.0	0.000
25.00	80.0	155.0	2.98e-4
25.00	80.0	160.0	3.40e-3
25.00	75.0	165.0	1.45e-3
25.00	75.0	170.0	3.22e-3
25.00	75.0	170.0	2.53e-3
25.00	75.0	175.0	4.50e-3
25.00	75.0	175.0	3.36e-3
25.00	75.0	180.0	3.68e-3
25.00	75.0	180.0	4.52e-3
25.00	75.0	180.0	2.86e-3
25.00	75.0	180.0	3.57e-3
25.00	75.0	185.0	2.28e-3
25.00	75.0	185.0	3.22e-3
25.00	75.0	190.0	1.20e-3
25.00	75.0	190.0	1.48e-3
25.00	75.0	195.0	6.10e-4
25.00	75.0	195.0	4.76e-4
25.00	75.0	200.0	1.71e-4
25.00	75.0	200.0	1.47e-4
25.00	75.0	205.0	3.05e-5
25.00	75.0	210.0	6.10e-6
25.00	75.0	210.0	5.08e-6
25.00	75.0	225.0	0.000
25.00	75.0	230.0	0.000
25.00	75.0	240.0	0.000
25.00	75.0	270.0	0.000

LET	Tilt	Rot	XS
25.00	80.0	180.0	1.23e-1
25.00	80.0	185.0	6.27e-2
25.00	80.0	190.0	9.12e-3
25.00	80.0	190.0	1.81e-2
25.00	80.0	195.0	1.15e-3
25.00	80.0	195.0	6.99e-4
25.00	80.0	195.0	4.27e-5
25.00	80.0	195.0	7.12e-4
25.00	80.0	200.0	1.37e-4
25.00	80.0	200.0	2.46e-4
25.00	80.0	205.0	9.49e-5
25.00	80.0	205.0	0.000
25.00	80.0	210.0	0.000
25.00	80.0	210.0	6.10e-6
25.00	80.0	220.0	0.000
25.00	80.0	225.0	0.000
25.00	80.0	235.0	0.000
25.00	80.0	235.0	0.000
25.00	80.0	250.0	0.000
25.00	80.0	250.0	0.000
25.00	80.0	270.0	0.000
25.00	77.5	0.0	4.12e-2
25.00	77.5	0.0	4.84e-2
25.00	77.5	180.0	5.50e-2
25.00	77.5	180.0	5.81e-2
25.00	75.0	-90.0	0.000
25.00	75.0	-60.0	0.000
25.00	75.0	-50.0	0.000
25.00	75.0	-45.0	0.000
17.00	85.0	0.0	6.23e-2
17.00	85.0	5.0	5.00e-2
17.00	85.0	10.0	2.30e-2
17.00	85.0	20.0	4.07e-4
17.00	85.0	30.0	0.000
17.00	85.0	60.0	0.000
17.00	85.0	120.0	0.000
17.00	85.0	150.0	0.000
17.00	85.0	160.0	0.000
17.00	85.0	170.0	1.87e-2
17.00	85.0	175.0	8.10e-2
17.00	85.0	180.0	1.95e-1
17.00	85.0	180.0	2.15e-1
17.00	85.0	180.0	1.78e-1
17.00	85.0	180.0	1.75e-1
17.00	85.0	185.0	1.29e-1
17.00	85.0	190.0	1.83e-3
17.00	85.0	200.0	0.000
17.00	85.0	210.0	0.000
17.00	85.0	240.0	0.000
17.00	82.5	0.0	1.31e-2
17.00	82.5	0.0	1.68e-2
17.00	82.5	180.0	2.18e-2
17.00	82.5	180.0	2.58e-2

LET	Tilt	Rot	XS
25.00	75.0	30.0	1.02e-5
25.00	75.0	30.0	1.22e-5
25.00	75.0	45.0	0.000
25.00	75.0	50.0	0.000
25.00	75.0	60.0	0.000
25.00	75.0	90.0	0.000
25.00	75.0	90.0	0.000
25.00	75.0	120.0	0.000
25.00	75.0	130.0	6.10e-6
25.00	75.0	135.0	0.000
25.00	75.0	150.0	0.000
25.00	75.0	150.0	6.10e-6
25.00	75.0	155.0	9.16e-5
25.00	75.0	160.0	7.22e-4
25.00	75.0	160.0	7.20e-4
25.00	75.0	165.0	1.37e-3
17.00	80.0	180.0	2.18e-3
17.00	80.0	185.0	1.95e-3
17.00	80.0	190.0	6.09e-4
17.00	80.0	205.0	0.000
17.00	77.5	0.0	5.49e-3
17.00	77.5	0.0	6.71e-3
17.00	77.5	180.0	5.19e-3
17.00	77.5	180.0	4.88e-3
17.00	75.0	0.0	6.10e-4
17.00	75.0	0.0	5.19e-4
17.00	75.0	0.0	3.97e-3
17.00	75.0	0.0	5.19e-3
17.00	75.0	180.0	6.41e-3
17.00	75.0	180.0	5.19e-3
17.00	75.0	180.0	1.37e-3
17.00	75.0	180.0	1.13e-3
17.00	60.0	0.0	0.000
17.00	60.0	0.0	0.000
17.00	60.0	180.0	0.000
17.00	60.0	180.0	0.000
7.50	87.0	-10.0	8.17e-5
7.50	87.0	-5.0	7.76e-3
7.50	87.0	0.0	1.41e-2
7.50	87.0	0.0	1.21e-2
7.50	87.0	5.0	1.07e-3
7.50	87.0	10.0	7.21e-5
7.50	87.0	170.0	8.17e-5
7.50	87.0	175.0	6.16e-3
7.50	87.0	180.0	4.91e-2
7.50	87.0	180.0	5.92e-2
7.50	87.0	185.0	1.37e-2
7.50	87.0	190.0	1.25e-4
7.50	85.0	-90.0	0.000
7.50	85.0	-60.0	0.000
7.50	85.0	-30.0	0.000
7.50	85.0	-20.0	0.000
7.50	85.0	-15.0	0.000

LET	Tilt	Rot	XS
25.00	70.0	0.0	3.26e-4
25.00	70.0	0.0	3.46e-4
25.00	70.0	180.0	1.83e-3
25.00	70.0	180.0	1.97e-3
25.00	60.0	0.0	4.88e-6
25.00	60.0	0.0	0.000
25.00	60.0	180.0	4.88e-6
25.00	60.0	180.0	1.46e-5
17.00	85.0	-60.0	0.000
17.00	85.0	-30.0	0.000
17.00	85.0	-20.0	0.000
17.00	85.0	-10.0	1.22e-3
17.00	85.0	-5.0	3.58e-2
17.00	85.0	0.0	1.21e-1
17.00	85.0	0.0	1.38e-1
17.00	85.0	0.0	5.34e-2
7.50	85.0	0.0	7.95e-3
7.50	85.0	0.0	9.32e-3
7.50	85.0	2.0	3.21e-3
7.50	85.0	5.0	1.51e-3
7.50	85.0	10.0	4.13e-5
7.50	85.0	15.0	4.77e-6
7.50	85.0	20.0	0.000
7.50	85.0	30.0	0.000
7.50	85.0	60.0	0.000
7.50	85.0	90.0	0.000
7.50	85.0	90.0	0.000
7.50	85.0	120.0	0.000
7.50	85.0	150.0	0.000
7.50	85.0	160.0	0.000
7.50	85.0	165.0	4.77e-6
7.50	85.0	170.0	2.22e-5
7.50	85.0	175.0	4.49e-3
7.50	85.0	178.0	1.38e-2
7.50	85.0	180.0	3.20e-2
7.50	85.0	180.0	3.30e-2
7.50	85.0	182.0	2.09e-2
7.50	85.0	185.0	5.92e-3
7.50	85.0	190.0	6.98e-5
7.50	85.0	195.0	0.000
7.50	85.0	200.0	0.000
7.50	85.0	210.0	0.000
7.50	85.0	240.0	0.000
7.50	85.0	270.0	0.000
7.50	80.0	-25.0	0.000
7.50	80.0	0.0	2.43e-5
7.50	80.0	0.0	1.52e-5
7.50	80.0	25.0	0.000
7.50	80.0	155.0	0.000
7.50	80.0	180.0	4.25e-5
7.50	80.0	180.0	3.95e-5
7.50	80.0	205.0	0.000
7.50	75.0	-90.0	0.000

LET	Tilt	Rot	XS
17.00	80.0	-25.0	0.000
17.00	80.0	-10.0	1.22e-4
17.00	80.0	-5.0	1.22e-3
17.00	80.0	0.0	2.95e-3
17.00	80.0	0.0	2.82e-3
17.00	80.0	0.0	6.10e-3
17.00	80.0	0.0	5.95e-3
17.00	80.0	5.0	3.53e-3
17.00	80.0	10.0	2.31e-3
17.00	80.0	25.0	0.000
17.00	80.0	155.0	0.000
17.00	80.0	170.0	1.95e-3
17.00	80.0	175.0	3.41e-3
17.00	80.0	180.0	5.34e-3
17.00	80.0	180.0	6.87e-3
17.00	80.0	180.0	2.24e-3
7.50	75.0	-10.0	1.22e-5
7.50	75.0	-5.0	6.10e-6
7.50	75.0	0.0	7.63e-6
7.50	75.0	0.0	7.63e-6
7.50	75.0	5.0	1.22e-5
7.50	75.0	10.0	2.44e-5
7.50	75.0	20.0	6.10e-6
7.50	75.0	30.0	0.000
7.50	75.0	60.0	0.000
7.50	75.0	90.0	0.000
7.50	75.0	90.0	0.000
7.50	75.0	120.0	0.000
7.50	75.0	150.0	0.000
7.50	75.0	160.0	0.000
7.50	75.0	170.0	1.22e-5
7.50	75.0	175.0	2.44e-5
7.50	75.0	180.0	1.72e-5
7.50	75.0	180.0	1.34e-5
7.50	75.0	185.0	1.83e-5
7.50	75.0	190.0	0.000
7.50	75.0	200.0	0.000
7.50	75.0	210.0	0.000
7.50	75.0	240.0	0.000
7.50	75.0	270.0	0.000
2.38	87.0	-10.0	1.83e-5
2.38	87.0	-5.0	2.69e-4
2.38	87.0	0.0	1.45e-3
2.38	87.0	0.0	1.07e-3
2.38	87.0	5.0	1.46e-4
2.38	87.0	10.0	1.22e-5
2.38	87.0	170.0	1.83e-5
2.38	87.0	175.0	2.80e-4
2.38	87.0	180.0	3.43e-3
2.38	87.0	180.0	3.43e-3
2.38	87.0	185.0	5.71e-4
2.38	87.0	190.0	1.22e-5
2.38	85.0	-90.0	0.000

It was pointed out in Section VIII that the Regression Wizard finds fitting parameters that produce a local minimum in the error measure, and it sometimes happens that these parameters do not even remotely resemble the parameters that produce the global minimum. That tendency was great enough when applied to the all-0's data that a good initial guess becomes essential for finding an acceptable fit to the data. The default initial parameters in Appendix D cannot be used for this example. An improved initial guess is obtained by starting with the fitting parameters for the 1's pattern (upper portion of Table 4) and then making modifications that roughly account for the differences between the 0's pattern and the 1's pattern. When comparing the 1's data (e.g., the points in Fig. 23) to the 0's data (e.g., the points in Fig. 28), three observations are made. The first observation is that, when comparing points at the same LET, the peak (maximized in direction) cross sections are comparable for the two bit patterns at the smaller LETs, but the peak cross section is about a factor of 2 larger for the 0's than the 1's at the larger LETs. The second observation is that the peak is at a rotation of about 180° for the 0's, compared to 0° for the 1's. The third observation is that the solid angle of susceptibility is smaller for the 0's, e.g., the pulse-shaped curves are narrower in Fig. 28 than in Fig. 23. The first and third properties have competing effects on upset rates. Model parameters for the 0's were obtained by starting with the fitting parameters for the 1's in Table 4, and then making three modifications. The first modification multiplies each parameter representing a linear dimension by $\sqrt{2}$ (these parameters are h and T) and multiplies each parameter representing an area by 2 (these parameters are $S01$ and $S02$). The result of this modification is to multiply the directional cross section by 2 for each direction. This accounts for the larger peak cross section for the 0's. The second modification reverses the sign of h so that the peak will be at about 180° instead of 0°. The last modification narrows the solid angle of susceptibility without affecting the peak cross section by a further increase in the separation parameter T . An arbitrary value of 2.2 μm was assigned to T . These modifications produced the initial guess shown in the upper portion of Table 5. From this initial guess, the Regression Wizard returned the fitting parameters in the lower portion of Table 5.

Table 5. Preliminary Model parameters for a later version of SRAM6 in all-0's

Initial Guess	A = 0.1474	B = 0.7419
	L01 = 0	L02 = 1.850e7
	S01 = 0.9226	S02 = 4.742e4
	phi_off = -8.898e-3	h = 8.58e-2
	P = 0.1868	T = 2.2
Returned by Regression Wizard	A = 0.1213	B = 0.8341
	L01 = 0	L02 = 1.850e7
	S01 = 1.859	S02 = 5.804e5
	phi_off = -6.606e-3	h = 5.746e-2
	P = 0.2084	T = 4.010

Plots (not shown here) of model predictions using the fitting parameters in the lower portion of Table 5 agree well with the data for some of the examples in Figs. 28 through 30, but in almost all (not all) examples where the agreement is not good, the model prediction under-estimates the measured cross section. In spite of the intention to include some conservatism via the choice of weight factor (explained in the discussion of the 1's data), the fit from the Table 5 parameters appears to be too optimistic. To compensate for this, manual adjustments were made to the parameters in order to make the fit more conservative. This was done by increasing $S01$ to the value of 2.5, and decreasing $L02$ to the value of 1.6×10^7 . These final fitting parameters are indicated in the upper portion of Table 6, and produced the curves in Figs. 28 through 30.

The upset rate from galactic cosmic rays in interplanetary space during solar minimum and behind 100 mils of spacecraft shielding is calculated the same way as for the 1's and the estimate is 5.33×10^{-11} /bit-day for the 0's (incidentally, this is only about twice the rate that would be calculated using the parameters in the lower portion of Table 5, so the conservatism that was manually introduced to obtain the final parameters in Table 6 was not excessive). The spreadsheet calculation shows that only about 10% of this calculated rate is from ions having an LET less than 3.16 MeV-cm²/mg, and only about 11% is from LET greater than 25.12 MeV-cm²/mg. The most important contribution is from ions having LET between 3 and 25 MeV-cm²/mg.

As with the 1's, it is convenient to have parameters that are recognized by CREME96 for the 0's. The directional-average cross section constructed from model parameters for the 0's is shown as the solid curve in Fig. 31, while the dashed curve is a Weibull fit that shows good agreement over the LET range that the previous paragraph identified as the important range. The inputs needed for a CREME96 calculation of rates in space for the 0's are in the lower portion of Table 6. In particular, the upset rate from galactic cosmic rays in interplanetary space during solar minimum and behind 100 mils of spacecraft shielding is calculated by CREME96 using Table 6 inputs to be 4.2×10^{-11} /bit-day, which is fairly close to the spreadsheet calculation of 5.33×10^{-11} /bit-day.

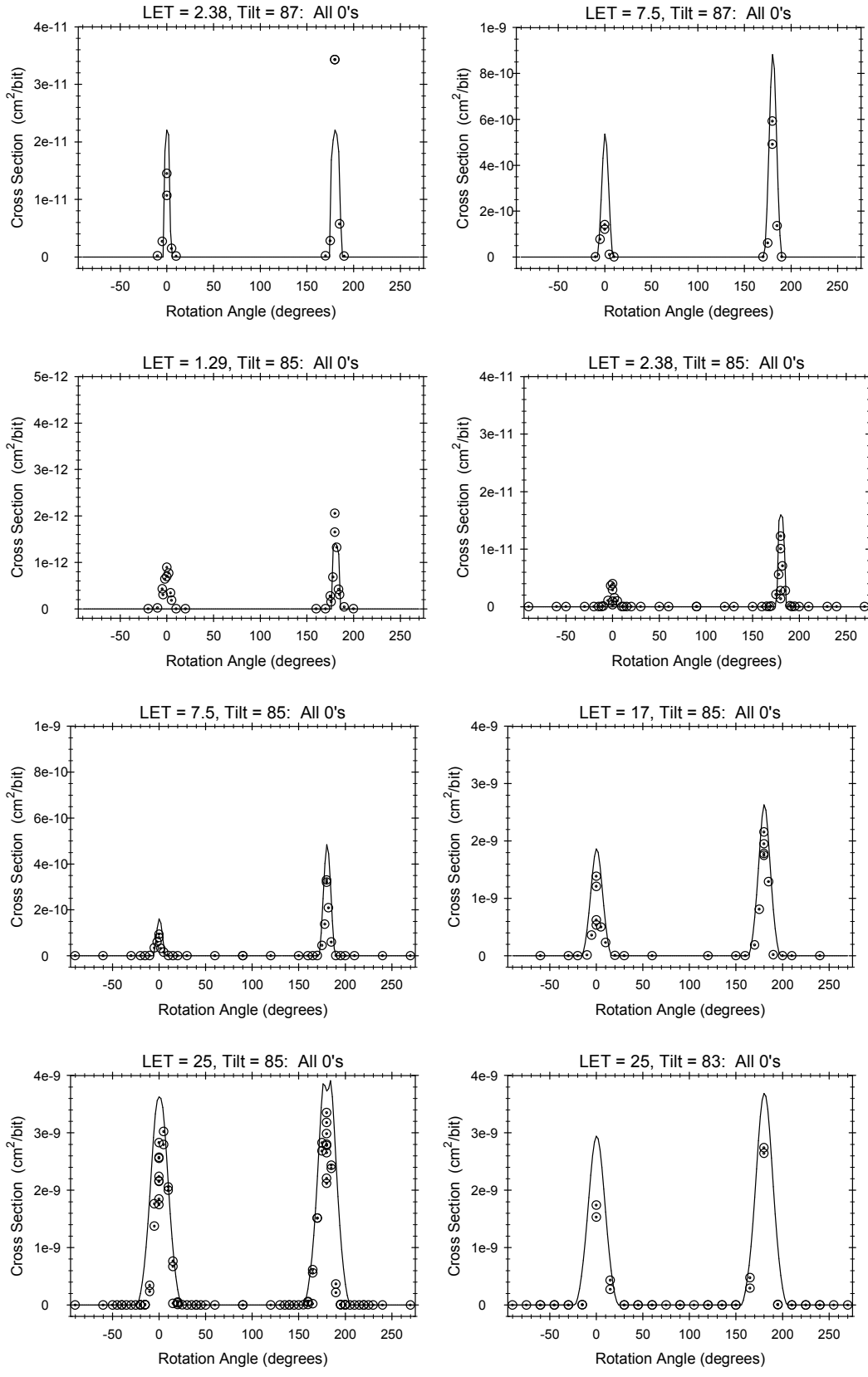


Fig. 28. Rotation sweeps for a later version of the SRAM6 in all-0's (page 1 of 2).

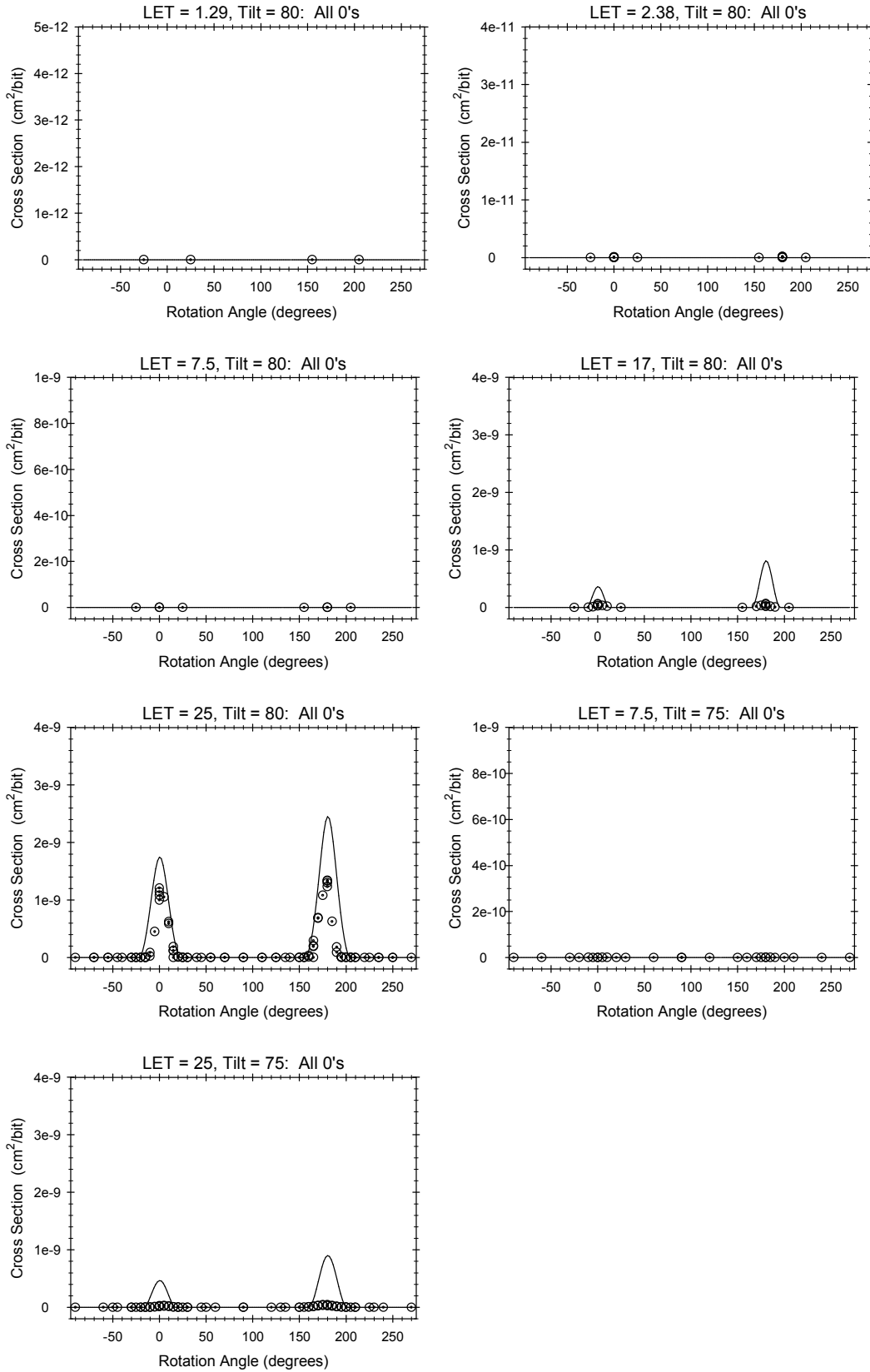


Fig. 28. Rotation sweeps for a later version of the SRAM6 in all-0's (page 2 of 2).

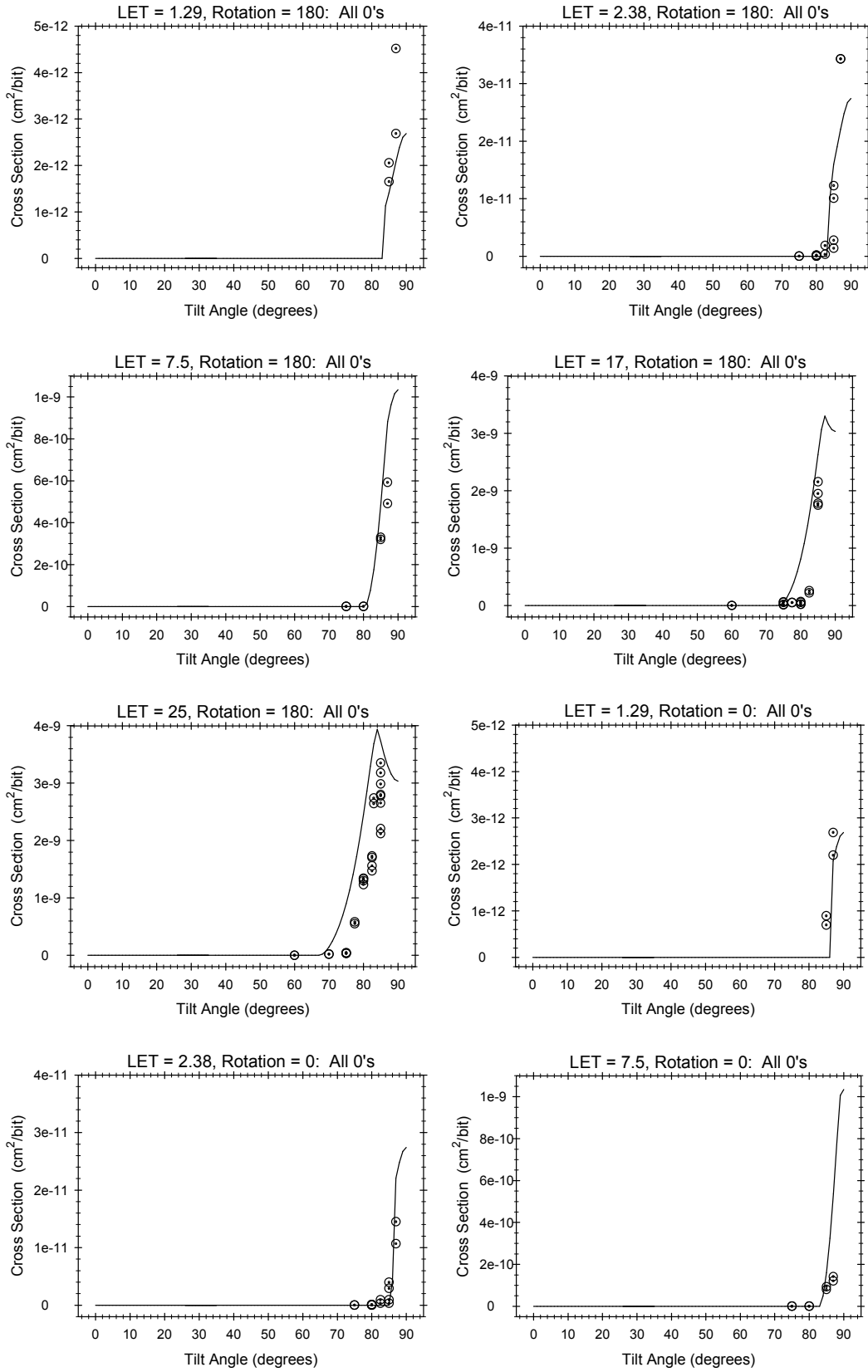


Fig. 29. Tilt sweeps for a later version of the SRAM6 in all-0's (page 1 of 2).

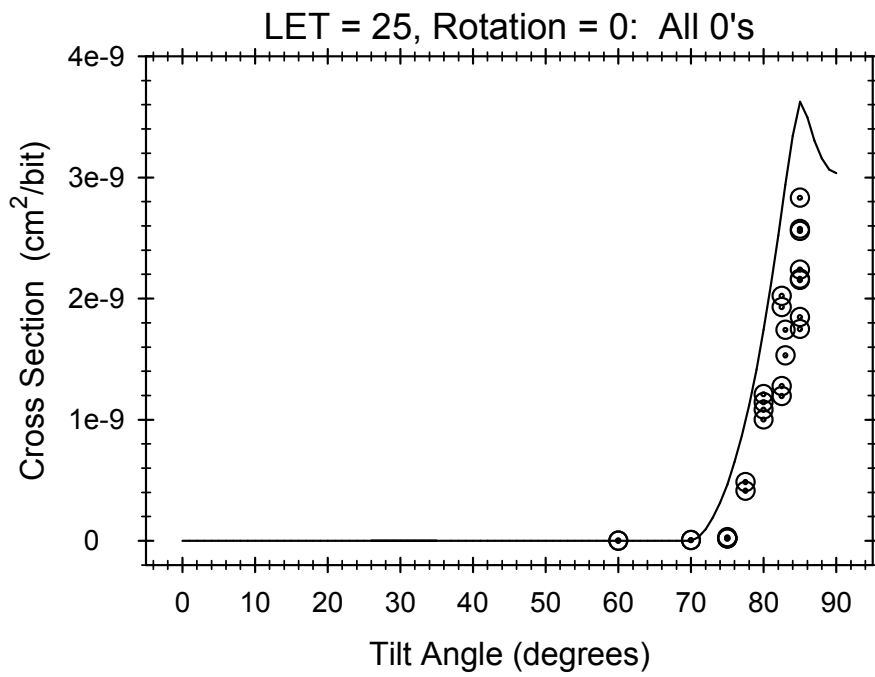
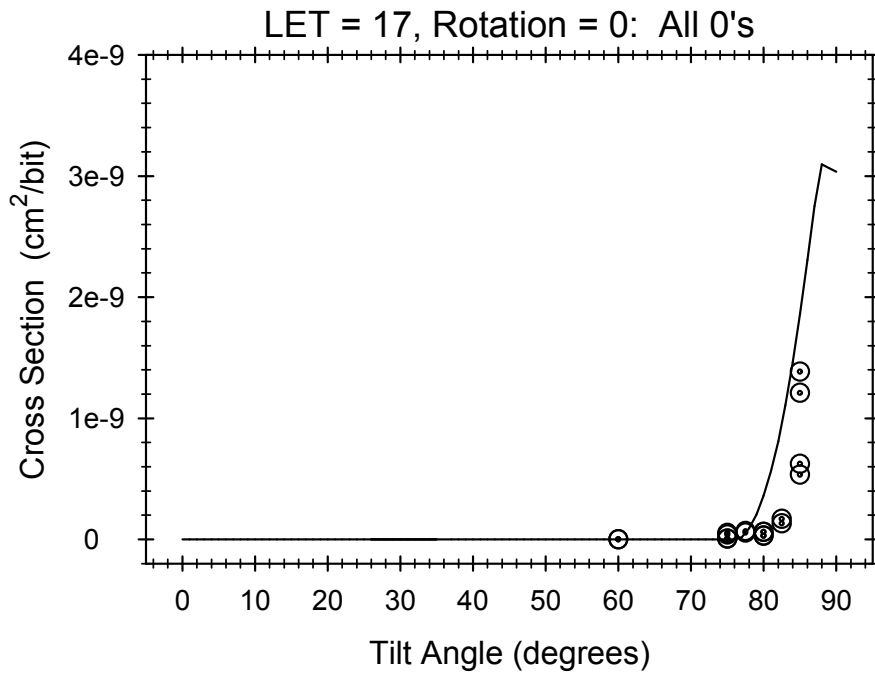


Fig. 29. Tilt sweeps for a later version of the SRAM6 in all-0's (page 2 of 2).

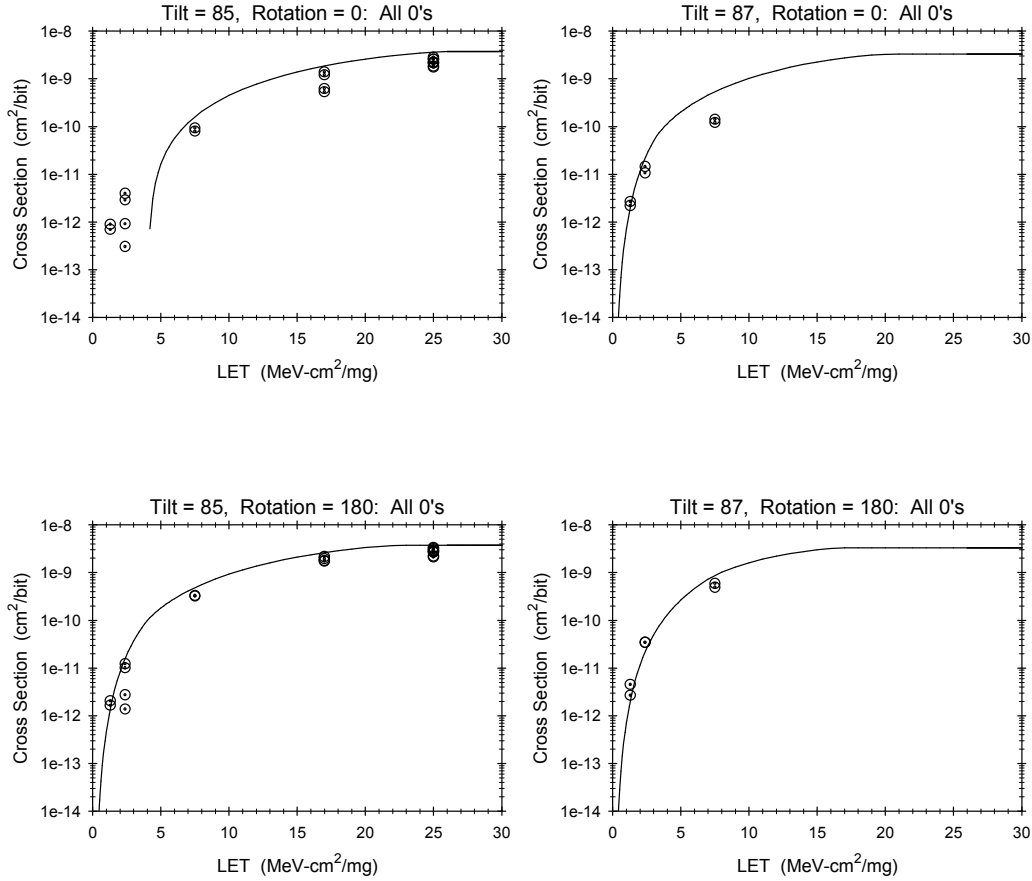


Fig. 30. LET sweeps for a later version of the SRAM6 in all-0's.

Table 6. Final Model and Weibull parameters for a later version of SRAM6 in all-0's

Model Parameters (slightly conservative)	
A = 0.1213	B = 0.8341
L01 = 0	L02 = 1.60e7
S01 = 2.50	S02 = 5.804e5
phi_off = -6.606e-3	h = 5.746e-2
P = 0.2084	T = 4.010
Weibull Parameters (inputs for a CREME96 calculation of heavy-ion rates in space)	
Onset = 0.25 MeV-cm ² /mg	Width = 103 MeV-cm ² /mg
Exponent = 2.95	Limiting XS = 0.80 μm ² /bit
X = Y = Z = 0.894 μm	funnel = 0

Note: A CREME96 calculation using the Weibull parameters gives a GCR rate of 4.2×10^{-11} /bit-day for the all-0's pattern.

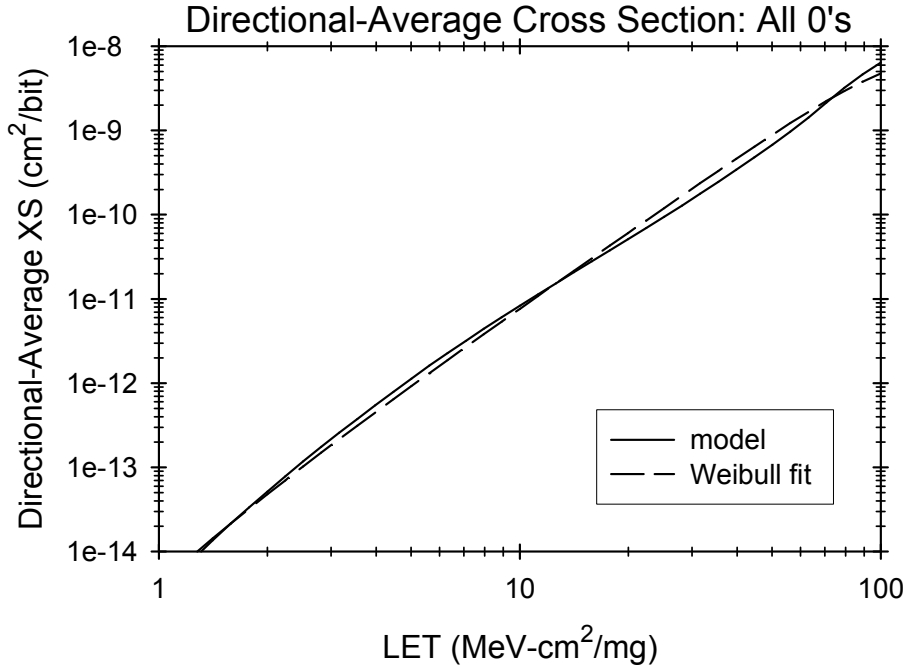


Fig. 31. The directional-average cross section (solid curve) produced by the code in Appendix F using inputs from Table IV applies to the later version of the SRAM6 in all-0's. The Weibull fit (dashed curve), using Weibull parameters in Table V, approximates the original curve over the plotted range. The plotted range represents the LET values that are most important for calculating heavy-ion rates in space.

C. Comparison with SRAM7

Another version of the device, called SRAM7, differs from SRAM6 in minor ways that are not expected to affect the upset rate. Test data for SRAM7 are not nearly as extensive as for SRAM6, but the objective is merely to show that there is agreement between the SRAM7 data and SRAM6 data. The two data sets are compared below.

Raw test data for the SRAM7, provided by Xilinx, were obtained from tests performed on 8/24/08, 9/25/08, and 2/12/09. However, a great deal of processing was needed to present these data sets in a readable and organized format. Gregory R. Allen (JPL) performed this processing and presented the data in column format in [12], which is reproduced here in Fig. 32. A set of sweeps selected so that every data point is included in at least one sweep is shown in Figs. 33 and 34. For each SRAM7 sweep there is a corresponding sweep available for SRAM6, so data points for both devices are included in these figures. It is seen from these figures that agreement between the two devices is well within experimental scatter, which supports the assertion that upset rates calculated for SRAM6 can also be used as estimates for SRAM7.

Fig. 32. Measured Data for the SRAM7. The cross sections are in cm²/bit.

All 1's				All 0's			
LET	Tilt	Rot	XS	LET	Tilt	Rot	XS
25.00	85.0	-90.0	3.49e-13	25.00	85.0	-90.0	0.000
25.00	85.0	0.0	6.59e-10	25.00	85.0	0.0	2.68e-9
25.00	85.0	0.0	6.53e-10	25.00	85.0	0.0	2.74e-9
25.00	85.0	90.0	1.74e-13	25.00	85.0	90.0	0.000
25.00	85.0	90.0	0.000	25.00	85.0	90.0	0.000
25.00	85.0	180.0	6.29e-10	25.00	85.0	180.0	3.22e-9
25.00	85.0	180.0	6.10e-10	25.00	85.0	180.0	2.86e-9
25.00	85.0	270.0	1.74e-13	25.00	85.0	270.0	0.000
25.00	82.5	0.0	6.84e-10	25.00	82.5	0.0	2.13e-9
25.00	82.5	0.0	5.74e-10	25.00	82.5	0.0	2.16e-9
25.00	82.5	180.0	4.27e-10	25.00	82.5	180.0	1.75e-9
25.00	82.5	180.0	4.15e-10	25.00	82.5	180.0	1.85e-9
25.00	80.0	0.0	1.03e-9	25.00	80.0	0.0	1.27e-9
25.00	80.0	0.0	1.01e-9	25.00	80.0	0.0	1.38e-9
25.00	80.0	180.0	9.63e-10	25.00	80.0	180.0	1.27e-9
25.00	80.0	180.0	9.33e-10	25.00	80.0	180.0	1.36e-9
25.00	77.5	0.0	1.39e-9	25.00	77.5	0.0	4.40e-10
25.00	77.5	0.0	1.28e-9	25.00	77.5	0.0	5.54e-10
25.00	77.5	180.0	1.77e-9	25.00	77.5	180.0	6.71e-10
25.00	77.5	180.0	1.41e-9	25.00	77.5	180.0	6.82e-10
25.00	75.0	0.0	1.25e-9	25.00	75.0	0.0	2.18e-11
25.00	75.0	0.0	1.15e-9	25.00	75.0	0.0	2.35e-11
25.00	75.0	180.0	1.49e-9	25.00	75.0	180.0	6.76e-11
25.00	75.0	180.0	1.37e-9	25.00	75.0	180.0	6.39e-11
17.00	75.0	0.0	8.73e-10	25.00	70.0	0.0	2.03e-12
17.00	75.0	0.0	7.38e-10	25.00	70.0	0.0	2.24e-12
17.00	75.0	180.0	1.26e-9	25.00	70.0	180.0	2.16e-11
17.00	75.0	180.0	1.14e-9	25.00	70.0	180.0	2.34e-11
7.50	75.0	0.0	1.99e-10	25.00	60.0	0.0	2.71e-14
7.50	75.0	0.0	1.40e-10	25.00	60.0	0.0	8.14e-14
7.50	75.0	180.0	9.35e-11	25.00	60.0	180.0	2.71e-14
7.50	75.0	180.0	7.27e-11	25.00	60.0	180.0	1.09e-13
2.38	75.0	0.0	3.07e-11	7.50	75.0	0.0	5.55e-14
2.38	75.0	0.0	2.28e-11	7.50	75.0	0.0	1.11e-13
2.38	75.0	180.0	5.59e-13	7.50	75.0	180.0	1.94e-13
2.38	75.0	180.0	4.32e-13	7.50	75.0	180.0	1.11e-13

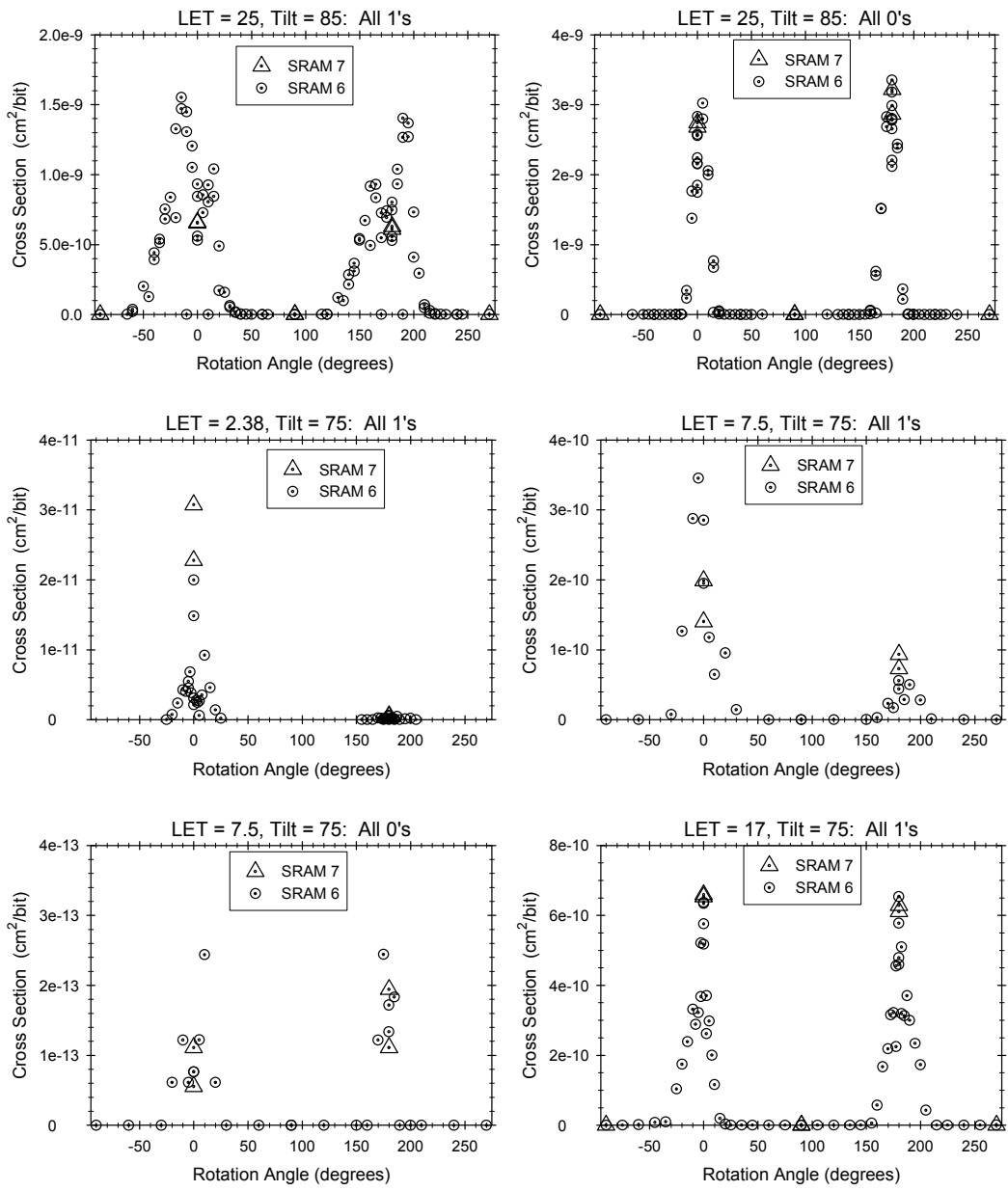


Fig. 33. Rotation sweeps for SRAM7 are compared to SRAM6.

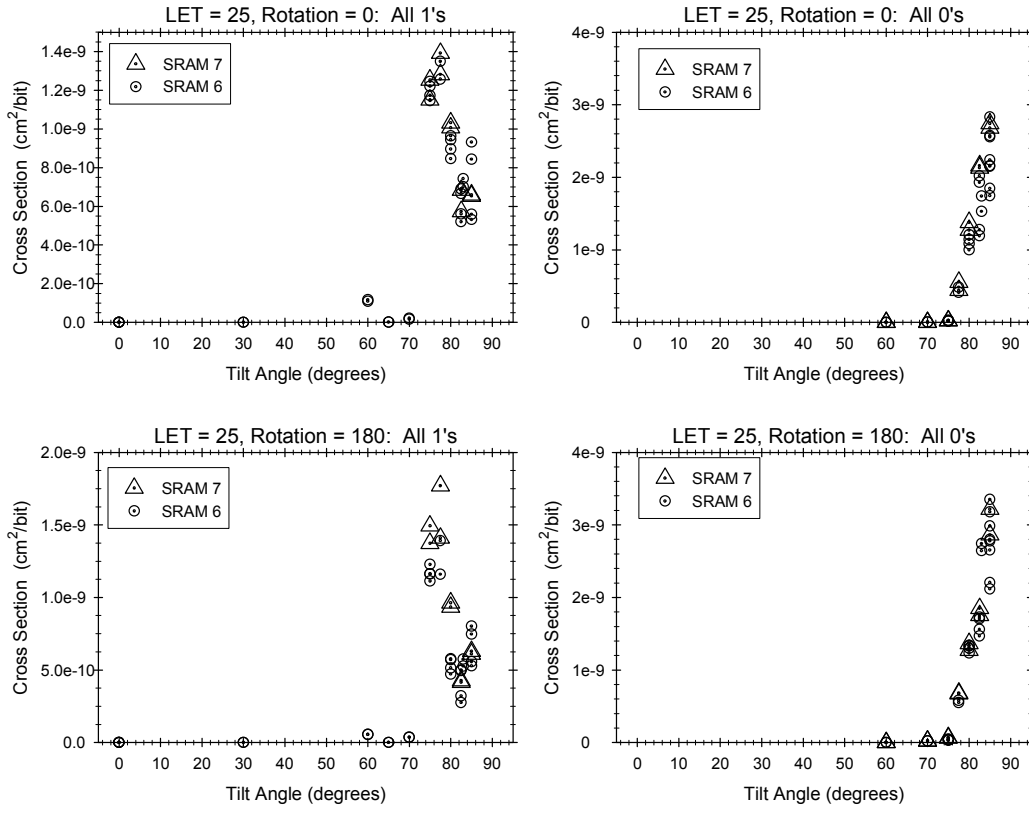


Fig. 34. Tilt sweeps for SRAM7 are compared to SRAM6.

APPENDIX A. DERIVATION OF (13)

To shorten the notation, write (12) as

$$\sigma_{AVG} \equiv \frac{1}{4\pi} \int_0^\pi \int_0^{2\pi} \sigma(\lambda(\theta, \varphi)) \sin \theta \, d\varphi \, d\theta. \quad (\text{A1})$$

Consider the surface integral I defined by

$$I \equiv \frac{1}{4\pi} \oint_S \sigma \left(\frac{|x|}{\sqrt{x^2 + y^2 + A^2 z^2}} \right) \frac{\vec{r}}{r^3} \circ d\vec{s} \quad (\text{A2})$$

where

$$\vec{r} \equiv x \hat{e}_1 + y \hat{e}_2 + z \hat{e}_3, \quad r \equiv \|\vec{r}\| \quad (\text{A3})$$

and the surface of integration is a sphere (hence the subscript S to the integral) centered at the origin and having some arbitrary radius R . The surface unit normal vector is taken to be an outer normal, so

$$d\vec{s} = \frac{\vec{r}}{r} ds \quad (\text{on sphere}). \quad (\text{A4})$$

Also, if we let (r, θ, φ) denote the spherical coordinates of the position vector \mathbf{r} , then

$$x = r \sin \theta \cos \varphi, \quad y = r \sin \theta \sin \varphi, \quad z = r \cos \theta. \quad (\text{A5})$$

An element of surface area on the sphere is given by

$$ds = R^2 \sin \theta \, d\varphi \, d\theta \quad (\text{on sphere}). \quad (\text{A6})$$

Recall that λ is defined by

$$\lambda(\theta, \varphi) \equiv \frac{|\sin \theta \cos \varphi|}{\sqrt{A^2 \cos^2 \theta + \sin^2 \theta}} \quad (\text{A7})$$

and combining this with (A5) gives

$$\frac{|x|}{\sqrt{x^2 + y^2 + A^2 z^2}} = \lambda(\theta, \varphi). \quad (\text{A8})$$

Substituting (A4), (A6), and (A8) into (A2), we find that the integral in (A2) is the same as the integral in (A1), i.e.,

$$\sigma_{AVG} = \frac{1}{4\pi} \oint_S \sigma \left(\frac{|x|}{\sqrt{x^2 + y^2 + A^2 z^2}} \right) \frac{\vec{r}}{r^3} \circ d\vec{s}. \quad (\text{A9})$$

The motivation for expressing α_{AVG} as a surface integral is that there might be some flexibility in how the surface of integration can be selected. To verify that there actually is flexibility, it is necessary to calculate the divergence of the integrand in (A9). Expressing the divergence operator in spherical coordinates, we find that

$$\vec{\nabla} \circ \left\{ \sigma \left(\frac{|x|}{\sqrt{x^2 + y^2 + A^2 z^2}} \right) \frac{\vec{r}}{r^3} \right\} = \vec{\nabla} \circ \left\{ \sigma(\lambda(\theta, \varphi)) \frac{\vec{r}}{r^3} \right\} = 0 \quad \text{if } r > 0$$

i.e., the divergence is zero except at the origin where there is a singularity. This property together with the divergence theorem implies that the spherical surface of integration can be replaced by any other closed surface that encloses the origin. A convenient choice for a closed surface is the ellipsoid denoted E and defined by

$$x^2 + y^2 + A^2 z^2 = D^2 \quad (\text{defines the ellipsoid E}) \quad (\text{A10})$$

where D is an arbitrary positive distance that is needed to give the coordinates the dimensions of distance. Replacing the sphere S with the ellipsoid E in (A9), and using (A10) to simplify one of the terms gives

$$\sigma_{AVG} = \frac{1}{4\pi} \oint_E \sigma \left(\frac{|x|}{D} \right) \frac{\vec{r}}{r^3} \circ d\vec{s}.$$

The left half of the ellipsoid (negative x) makes the same contribution to the integral as the right half, so we can also write

$$\sigma_{AVG} = \frac{1}{2\pi} \int_{E/2} \sigma \left(\frac{x}{D} \right) \frac{\vec{r}}{r^3} \circ d\vec{s} \quad (\text{A11})$$

where the subscript E/2 indicates half of the ellipsoid defined by

$$x^2 + y^2 + A^2 z^2 = D^2, \quad 0 \leq x \leq D \quad (\text{defines E/2}). \quad (\text{A12})$$

It is convenient to express the surface integral in parametric form, but it is necessary to first express the equation for the surface in parametric form. One convenient choice of parametric equations that define E/2 is

$$x = Du, \quad y = D\sqrt{1-u^2} \cos v, \quad z = \frac{D}{A}\sqrt{1-u^2} \sin v \quad (\text{A13a})$$

where the parameters u and v have the range of values

$$0 \leq u \leq 1, \quad 0 \leq v \leq 2\pi. \quad (\text{A13b})$$

The integral in (A11) can be expressed as [13]

$$\sigma_{AVG} = \frac{1}{2\pi} \int_0^1 \int_0^{2\pi} \sigma(u) \left| \frac{\vec{r}}{r^3} \circ (\vec{P}_1 \times \vec{P}_2) \right| dv du \quad (\text{A14})$$

where

$$\vec{P}_1 \equiv \frac{\partial x}{\partial u} \hat{e}_1 + \frac{\partial y}{\partial u} \hat{e}_2 + \frac{\partial z}{\partial u} \hat{e}_3, \quad \vec{P}_2 \equiv \frac{\partial x}{\partial v} \hat{e}_1 + \frac{\partial y}{\partial v} \hat{e}_2 + \frac{\partial z}{\partial v} \hat{e}_3. \quad (\text{A15})$$

Using (A13a) to calculate the derivatives in (A15) gives

$$\vec{r} \circ (\vec{P}_2 \times \vec{P}_1) = \frac{D^3}{A}$$

so (A14) becomes

$$\sigma_{AVG} = \frac{A^2}{2\pi} \int_0^1 \int_0^{2\pi} \frac{\sigma(u)}{\left[A^2 - (A^2 - 1)(1 - u^2) \sin^2 v \right]^{3/2}} dv du$$

which can also be written as

$$\sigma_{AVG} = \frac{1}{A} \int_0^1 W \left(\left(1 - \frac{1}{A^2} \right) (1 - \lambda^2) \right) \sigma(\lambda) d\lambda \quad (\text{A16})$$

where we changed dummy symbols from u to λ , and W is defined by

$$W(\xi) \equiv \frac{1}{2\pi} \int_0^{2\pi} \left[1 - \xi \sin^2 v \right]^{-3/2} dv, \quad -\infty < \xi < 1. \quad (\text{A17})$$

To shorten the notation, define T by

$$T(\lambda) \equiv W \left(\left(1 - \frac{1}{A^2} \right) (1 - \lambda^2) \right) \quad (\text{A18})$$

so (A16) becomes

$$\sigma_{AVG} = \frac{1}{A} \int_0^1 T(\lambda) \sigma(\lambda) d\lambda. \quad (\text{A19})$$

APPENDIX B. DERIVATION OF (14)

An approximation for T is obtained by first deriving an approximation for W given by (A17). Note that W can be related to the complete elliptic integral of the third kind, but this is a special case (because of repeated factors) that can also be expressed in terms of the complete elliptic integral of the second kind. The analysis below first relates W to the latter integral, and then uses an approximation for this integral to obtain an approximation for W .

Previously defined geometric quantities are not needed here, so we start over with a fresh x-y plane and fresh symbolism. Consider the line integral I defined by

$$I \equiv \frac{1}{2\pi} \oint_C \frac{[x^2 + y^2]^{3/2}}{[x^2 + (1-\xi)y^2]^{3/2}} \frac{\vec{r}}{r^2} \circ \hat{n} dl \quad (\text{B1})$$

where

$$\vec{r} \equiv x \hat{e}_1 + y \hat{e}_2, \quad r \equiv \|\vec{r}\| = \sqrt{x^2 + y^2} \quad (\text{B2})$$

and the path of integration is a circle (hence the subscript C to the integral) in the x-y plane, centered at the origin and having some arbitrary radius R . The curve unit normal vector is taken to be an outer normal, so

$$\hat{n} = \frac{\vec{r}}{r} \quad (\text{on circle}). \quad (\text{B3})$$

Also, if we let (r, θ) denote the polar coordinates of the position vector \mathbf{r} , then

$$x = r \cos \theta, \quad y = r \sin \theta. \quad (\text{B4})$$

An element of arc length on the circle is given by

$$dl = R d\theta \quad (\text{on circle}). \quad (\text{B5})$$

Note that (B4) gives

$$\frac{[x^2 + y^2]^{3/2}}{[x^2 + (1-\xi)y^2]^{3/2}} = [1 - \xi \sin^2 \theta]^{-3/2}. \quad (\text{B6})$$

Substituting (B3), (B5), and (B6) into (B1), we find that the integral in (B1) is the same as the integral in (A17), i.e.,

$$W(\xi) = \frac{1}{2\pi} \oint_C \frac{[x^2 + y^2]^{3/2}}{[x^2 + (1-\xi)y^2]^{3/2}} \frac{\vec{r}}{r^2} \circ \hat{n} dl. \quad (\text{B7})$$

The motivation for expressing W as a line integral is that there might be some flexibility in how the curve of integration can be selected. To verify that there actually is flexibility, it is necessary to calculate the 2-dimensional divergence of the integrand in (B7). Expressing the divergence operator in polar coordinates (the same as in cylindrical coordinates but without the z-derivative), we find that

$$\bar{\nabla} \circ \left\{ \frac{[x^2 + y^2]^{3/2}}{[x^2 + (1-\xi)y^2]^{3/2}} \frac{\vec{r}}{r^2} \right\} = \bar{\nabla} \circ \left\{ [1 - \xi \sin^2 \theta]^{-3/2} \frac{\vec{r}}{r^2} \right\} = 0 \quad \text{if } r > 0$$

i.e., the divergence is zero except at the origin where there is a singularity. This property together with a 2-dimensional version of the divergence theorem implies that the circular path of integration can be replaced by any other closed curve that encloses the origin. A convenient choice for a closed curve is the ellipse denoted E and defined by

$$x^2 + (1-\xi)y^2 = R^2 \quad (\text{defines the ellipse E}) \quad (\text{B8})$$

where R is an arbitrary positive distance that is needed to give the coordinates the dimensions of distance. The requirement that $\xi < 1$ implies that (B8) does define an ellipse that encloses the origin. Replacing the circle C with the ellipse E in (B7), and using (B8) to simplify one of the terms gives

$$W(\xi) = \frac{1}{2\pi R^3} \oint_E \sqrt{x^2 + y^2} (\vec{r} \circ \hat{n}) dl. \quad (\text{B9})$$

A normal vector to the curve E is the gradient of the left side of (B8), and the outer normal unit vector is given by

$$\hat{n} = \frac{x \hat{e}_1 + (1-\xi) y \hat{e}_2}{\sqrt{x^2 + (1-\xi)^2 y^2}}$$

so

$$\vec{r} \circ \hat{n} = \frac{R^2}{\sqrt{x^2 + (1-\xi)^2 y^2}}. \quad (\text{B10})$$

It is convenient to express the line integral in parametric form, but it is necessary to first express the equation for the ellipse in parametric form. One convenient choice of parametric equations that define E is

$$x = R \cos \omega, \quad y = \frac{R}{\sqrt{1-\xi}} \sin \omega, \quad 0 \leq \omega \leq 2\pi \quad (\text{B11})$$

so

$$dl = \sqrt{\left(\frac{dx}{d\omega}\right)^2 + \left(\frac{dy}{d\omega}\right)^2} d\omega = \frac{R}{\sqrt{1-\xi}} \sqrt{1-\xi \sin^2 \omega} d\omega \quad (\text{B12})$$

while (B10) becomes

$$\vec{r} \circ \hat{n} = \frac{R}{\sqrt{1-\xi \sin^2 \omega}}. \quad (\text{B13})$$

Substituting (B11), (B12), and (B13) into (B9) gives

$$W(\xi) = \frac{1}{2\pi(1-\xi)} \int_0^{2\pi} \sqrt{1-\xi \cos^2 \omega} d\omega = \frac{2}{\pi(1-\xi)} \int_0^{\pi/2} \sqrt{1-\xi \cos^2 \omega} d\omega.$$

Changing variables in the last integral gives

$$W(\xi) = \frac{2}{\pi(1-\xi)} \int_0^{\pi/2} \sqrt{1-\xi \sin^2 \omega} d\omega \quad (\text{B14})$$

which expresses W in terms of the complete elliptic integral of the second kind. An approximation is obtained by relating this integral to the perimeter P of the ellipse defined by (B8), and then using an approximation for the perimeter. The perimeter is given by

$$P = \oint_E dl$$

and using (B12) gives

$$P = \frac{R}{\sqrt{1-\xi}} \int_0^{2\pi} \sqrt{1-\xi \sin^2 \omega} d\omega = \frac{4R}{\sqrt{1-\xi}} \int_0^{\pi/2} \sqrt{1-\xi \sin^2 \omega} d\omega. \quad (\text{B15})$$

An approximation for the perimeter P , derived by Lindner [14] but using the notation shown in (B8), is

$$P \approx \pi R \frac{1+\sqrt{1-\xi}}{\sqrt{1-\xi}} \left[1 + \frac{1}{8} \left(\frac{\sqrt{1-\xi}-1}{\sqrt{1-\xi}+1} \right)^2 \right]^2.$$

The error in this approximation is less than 0.6% regardless of the eccentricity of the ellipse. Combining this approximation with (B15) gives

$$\int_0^{\pi/2} \sqrt{1-\xi \sin^2 \omega} \, d\omega \approx \frac{\pi}{4} (1 + \sqrt{1-\xi}) \left[1 + \frac{1}{8} \left(\frac{\sqrt{1-\xi} - 1}{\sqrt{1-\xi} + 1} \right)^2 \right]^2 \quad (-\infty < \xi \leq 1). \quad (\text{B16})$$

Again, the error in this approximation is less than 0.6% for any ξ between $-\infty$ and 1. Substituting (B16) into (B14) produces an approximation for W , and combining this result with (A18) produces the approximation (14) for T .

APPENDIX C. EVALUATION OF I

The area of intersection $I(R_1, R_2, D)$ is defined to be the area of the intersection of two circular regions, one having radius R_1 and the other having radius R_2 , when the distance between centers is D . Elementary analysis will show that this area is given by:

$$\text{If } D \geq R_1 + R_2 \text{ then} \\ I(R_1, R_2, D) = 0.$$

$$\text{If } D \leq |R_1 - R_2| \text{ then} \\ I(R_1, R_2, D) = \min\{\pi R_1^2, \pi R_2^2\}.$$

$$\text{If } |R_1 - R_2| < D < R_1 + R_2 \text{ then}$$

$$I(R_1, R_2, D) = R_1^2 \arccos\left[\frac{D^2 + R_1^2 - R_2^2}{2D R_1}\right] + R_2^2 \arccos\left[\frac{D^2 + R_2^2 - R_1^2}{2D R_2}\right] \\ - \frac{1}{2} \sqrt{4R_1^2 R_2^2 - (R_1^2 + R_2^2 - D^2)^2}.$$

The first result applies when the circles are so widely separated that there is no region of intersection. The second result applies when the circle centers are close enough that the smaller circle is entirely contained within the larger. The third result applies to all other cases. When numerically evaluating the last expression, it may be useful to know that the three terms on the right are defined real numbers if and only if the qualifying condition is satisfied (but the equalities are allowed). Therefore, the qualifying condition should be checked before attempting to numerically evaluate this expression. Also, round-off error can cause a quantity contained in this expression to become undefined in a computer calculation even when it would be defined in an exact calculation, and this would be the prime suspect if errors are encountered during program execution.

APPENDIX D. REGRESSION WIZARD PROGRAMMING

Equation

```
pi=3.14159265359
T=2
;Make sure trig units are rads.
phi=phi_dat+phi_off
csp=cos(phi)
cst=cos(theta)
snp=sin(phi)
snt=sin(theta)
arg1=A*A*csp*csp+B*B*snp*snp
arg2=cst*cst+arg1*snt*snt
alph=sqrt(arg2)
arg3=-1.0*(L01*alph/L)**P
arg4=-1.0*(L02*alph/L)**P
S1=S01*alph*exp(arg3)
S2=S02*alph*exp(arg4)
r1=sqrt(S1/pi)
r2=sqrt(S2/pi)
arg5a=(alph*alph-cst*cst)*h*h/(A*B)
arg5b=2*(A/B)*snt*cst*csp*h*T
arg5c=(A*B*snp*snp*snt*snt+(A/B)*cst*cst)*T*T
arg5=arg5a+arg5b+arg5c
d=sqrt(arg5/alph)
rmin=if(r1>r2,r2,r1)
rs=r1+r2
rd=abs(r1-r2)
Sa=pi*rmin*rmin
arg6a=(d*d+r1*r1-r2*r2)/(2*d*r1)
arg7a=(d*d+r2*r2-r1*r1)/(2*d*r2)
arg6b=if(arg6a>-1,arg6a,-1)
arg7b=if(arg7a>-1,arg7a,-1)
arg6=if(arg6b<1,arg6b,1)
arg7=if(arg7b<1,arg7b,1)
arg8a=4*r1*r1*r2*r2-(r1*r1+r2*r2-d*d)*(r1*r1+r2*r2-d*d)
arg8=if(arg8a>0,arg8a,0)
Sb=r1*r1*acos(arg6)+r2*r2*acos(arg7)-0.5*sqrt(arg8)
Sc=if(d>rd,Sb,Sa)
S=if(d>rs,0,Sc)
f=ln(1+S)
fit f to y with weight w
```

Variables

```
L=col(3)
theta=3.14159265359*col(5)/180
phi_dat=3.14159265359*col(4)/180
XS=col(6)
y=ln(1+XS)
w=1/col(3)^3
```

Constraints

```
A>0
B>0
L01>=0
L02>=0
S01>0
S02>0
phi_off<1.571
phi_off>-1.571
h>-5
h<5
P>0
;T>0
```

Initial Parameters

```
A = 0.2
B = 0.2
L01 = 10
L02 = 100
S01 = 5
S02 = 5
phi_off = 0
h = 0
P = 0.5
;T=2
```

Iterations = 500, Step Size = 10, Tolerance = 0.000001

APPENDIX E. THE TRANSFORM

```
;Make sure trig button is on rads.
```

```
A=0.2234  
B=0.6953  
L01=0  
L02=43.85  
S01=2.914  
S02=1.215  
phi_off=1.685e-2  
h=6.583e-3  
P=0.7075  
T=2
```

← *Assign parameters*

```
pi=3.14159265359
```

```
L=3.4  
;L=col(7)  
theta=pi*75/180  
;theta=pi*col(7)/180  
;phi_data=pi*180/180  
phi_data=pi*col(7)/180
```

← *Assign variables*

```
phi=phi_data+phi_off  
csp=cos(phi)  
cst=cos(theta)  
snp=sin(phi)  
snt=sin(theta)  
arg1=A*A*csp*csp+B*B*snp*snp  
arg2=cst*cst+arg1*snt*snt  
alph=sqrt(arg2)  
arg3=-1.0*(L01*alph/L)**P  
arg4=-1.0*(L02*alph/L)**P  
S1=S01*alph*exp(arg3)  
S2=S02*alph*exp(arg4)  
r1=sqrt(S1/pi)  
r2=sqrt(S2/pi)  
arg5a=(alph*alph-cst*cst)*h*h/(A*B)  
arg5b=2*(A/B)*snt*cst*csp*h*T  
arg5c=(A*B*snp*snp*snt*snt+(A/B)*cst*cst)*T*T  
arg5=arg5a+arg5b+arg5c  
d=sqrt(arg5/alph)  
rmin=if(r1>r2,r2,r1)  
rs=r1+r2  
rd=abs(r1-r2)  
Sa=pi*rmin*rmin
```

```
arg6a=(d*d+r1*r1-r2*r2)/(2*d*r1)
arg7a=(d*d+r2*r2-r1*r1)/(2*d*r2)
arg6b=if(arg6a>-1,arg6a,-1)
arg7b=if(arg7a>-1,arg7a,-1)
arg6=if(arg6b<1,arg6b,1)
arg7=if(arg7b<1,arg7b,1)
arg8a=4*r1*r1*r2*r2-(r1*r1+r2*r2-d*d)*(r1*r1+r2*r2-d*d)
arg8=if(arg8a>0,arg8a,0)
Sb=r1*r1*acos(arg6)+r2*r2*acos(arg7)-0.5*sqrt(arg8)
Sc=if(d>rd,Sb,Sa)
S=if(d>rs,0,Sc)
```

```
;col(8)=S
col(9)=S
```

← *Assign output column*

APPENDIX F. THE FORTRAN CODE

```
PROGRAM XSAVG
REAL L01,L02,L
DIMENSION XPHIA(45)
COMMON PI,A,B,L01,L02,S01,S02,H,T,P
PI=3.14159265359
WRITE(*,*)'ENTER A      '
READ(*,*)A
WRITE(*,*)'ENTER B      '
READ(*,*)B
WRITE(*,*)'ENTER L01    '
READ(*,*)L01
WRITE(*,*)'ENTER L02    '
READ(*,*)L02
WRITE(*,*)'ENTER S01 IN um2  '
READ(*,*)S01
WRITE(*,*)'ENTER S02 IN um2  '
READ(*,*)S02
WRITE(*,*)'ENTER h IN um      '
READ(*,*)H
WRITE(*,*)'ENTER T IN um      '
READ(*,*)T
WRITE(*,*)'ENTER P      '
READ(*,*)P
OPEN(UNIT=9,STATUS='UNKNOWN',FILE='XSAVG.TXT')
REWIND(9)
WRITE(9,100)'  LET      ','XS AVG '
WRITE(9,100)'MeV-cm2/mg','cm2/bit'
WRITE(9,100)'-----','-----'
DO 50 K=1,61
RK=FLOAT(K)
L=10.0**((RK-21.0)/20.0)
DO 30 J=1,45
THETA=FLOAT(2*J-1)
THETA=PI*THETA/180.0
SUMXS=0.0
DO 20 I=0,179
PHI=FLOAT(2*I+1)
PHI=PI*PHI/180.0
XS=XDIR(L,THETA,PHI)
SUMXS=SUMXS+XS
20 CONTINUE
XPHIA(J)=SUMXS/180.0
30 CONTINUE
SUM=0.0
DO 40 J=1,45
THETA=FLOAT(2*J-1)
THETA=PI*THETA/180.0
SUM=SUM+XPHIA(J)*SIN(THETA)
40 CONTINUE
XAVG=PI*SUM/90.0
XAVG=1.0E-8*XAVG
WRITE(9,110)L,XAVG
50 CONTINUE
CLOSE(9)
100 FORMAT(A22,A12)
```

```

110 FORMAT (F19.2, 1P, E15.2)
      END
C*****
      FUNCTION XDIR(L, THETA, PHI)
      COMMON PI, A, B, L01, L02, S01, S02, H, T, P
      REAL L01, L02, L
      CP=COS (PHI)
      SP=SIN (PHI)
      CT=COS (THETA)
      ST=SIN (THETA)
      ARG1=A*A*CP*CP+B*B*SP*SP
      ARG2=CT*CT+ARG1*ST*ST
      ALPH=SQRT (ARG2)
      ARG3=-1.0*(L01*ALPH/L)**P
      ARG4=-1.0*(L02*ALPH/L)**P
      S1=S01*ALPH*EXP (ARG3)
      S2=S02*ALPH*EXP (ARG4)
      R1=SQRT (S1/PI)
      R2=SQRT (S2/PI)
      ARG5A= (ALPH*ALPH-CT*CT) *H*H/ (A*B)
      ARG5B=2.0*(A/B) *ST*CT*CP*H*T
      ARG5C= (A*B*SP*SP*ST*ST+ (A/B) *CT*CT) *T*T
      ARG5=ARG5A+ARG5B+ARG5C
      IF (ARG5.LE.0.0) ARG5=0.0
      D=SQRT (ARG5/ALPH)
      RMIN=R1
      IF (R2.LT.R1) RMIN=R2
      RSUM=R1+R2
      RDIF=ABS (R1-R2)
      IF (D.GE.RSUM) XDIR=0.0
      IF (D.LE.RDIF) XDIR=PI*RMIN*RMIN
      IF ((D.GT.RDIF).AND.(D.LT.RSUM)) THEN
        ARG6= (D*D+R1*R1-R2*R2) / (2.0*D*R1)
        ARG7= (D*D+R2*R2-R1*R1) / (2.0*D*R2)
        ARG8=4.0*R1*R1*R2*R2- (R1*R1+R2*R2-D*D) * (R1*R1+R2*R2-D*D)
        XDIR=R1*R1*ACOS (ARG6) +R2*R2*ACOS (ARG7) -0.5*SQRT (ARG8)
      END IF
      RETURN
      END

```

REFERENCES

- [1] L.D. Edmonds, "A Graphical Method for Estimating Charge Collected by Diffusion from an Ion Track," *IEEE Transactions on Nuclear Science*, vol. 43, no. 4, pp. 2346–2357, August 1996.
- [2] L. Edmonds, G. Swift, and A. Johnston, "Non-Destructive Measurements for CMOS Devices Using Charge-Collection Techniques," *IEEE Transactions on Nuclear Science*, vol. 43, no. 6, pp. 2833–2842, December 1996.
- [3] L.D. Edmonds, "SEU Cross Sections Derived from a Diffusion Analysis," *IEEE Transactions on Nuclear Science*, vol. 43, no. 6, pp. 3207–3217, December 1996.
- [4] L.D. Edmonds, "Charge Collection from Ion Tracks in Simple EPI Diodes," *IEEE Transactions on Nuclear Science*, vol. 44, no. 3, pp. 1448–1463, June 1997.
- [5] L.D. Edmonds, "Proton SEU Cross Sections Derived from Heavy-Ion Test Data," *IEEE Transactions on Nuclear Science*, vol. 47, no. 5, pp. 1713–1728, October 2000.
- [6] S. Guertin, L. Edmonds, and G. Swift, "Angular Dependence of DRAM Upset Susceptibility and Implications for Testing and Analysis," *IEEE Transactions on Nuclear Science*, vol. 47, no. 6, pp. 2380–2385, December 2000.
- [7] L.D. Edmonds, "A Time-Dependent Charge-Collection Efficiency for Diffusion," *IEEE Transactions on Nuclear Science*, vol. 48, no. 5, pp. 1609–1622, October 2001.
- [8] L.D. Edmonds, "A Method for Correcting Cosine-Law Errors in SEU Test Data," *IEEE Transactions on Nuclear Science*, vol. 49, no. 3, pp. 1522–1538, June 2002.
- [9] E.L. Petersen, J.C. Pickel, J.H. Adams, Jr., and E.C. Smith, "Rate Prediction for Single Event Effects—A Critique," *IEEE Transactions on Nuclear Science*, vol. 39, pp. 1577–1599, Dec. 1992.
- [10] D. Binder, "Analytic SEU Rate Calculation Compared to Space Data," *IEEE Transactions on Nuclear Science*, vol. 35, pp. 1570–1572, Dec. 1988.
- [11] Allen, Gregory R, "<no subject>," e-mail sent 12/08/2010.
- [12] Allen, Gregory R, "SRAM 7," e-mail sent 1/04/2011.
- [13] W. Kaplan, *Advanced Calculus*, Addison-Wesley, 1973, p. 334.
- [14] On the internet at <http://home.att.net/~numericana/answer/ellipse.htm> .
- [15] J.D. Patterson and L.D. Edmonds, "Automating the Modeling of the SEE Cross Section's Angular Dependence," RADECS 2003, pp. 217–223, Sept. 2003.